AD-A956 124

ELECTE
AUG 5 1992
S C D

(1)

21629-599-91
Cy 1 A

85029599
NCIPA CLASSIFIED LIBRARY

THE ASTRAL MODEL
VOLUME I:
TECHNICAL DESCRIPTION

Approved for public release; distribution is unlimited.

SCIENCE APPLICATIONS, INC.

DTIC QUALITY INSPECTED 5

Accession For
NTIS GRA&I ☒
DTIC TAB ☐
Unannounced ☐
Justification
By
Distribution/
Availability Codes
Dist | Avail and/or Special
A-1 | 21

THE ASTRAL MODEL.
VOLUME I:
TECHNICAL DESCRIPTION

SAI-79-742-WA

January 1979

Prepared by:
Science Applications, Inc.
C. W. Spofford

Prepared for:
Long Range Acoustic Propagation Project
NORDA Code 600
NSTL Station, Mississippi

Prepared Under Contract No. N00014-77-C-0502

SCIENCE APPLICATIONS, INC.
8400 Westpark Drive, McLean, ~~Virginia 22101~~ VA.
Telephone 703/821-4300

92-21228
168
92 8 04 009

CONTENTS

		Page
	ABSTRACT	i
1	INTRODUCTION	1-1
	1.1 Background	1-1
	1.2 Structure of Report	1-2
	1.3 Acknowledgments	1-3
2	BASIC MODEL DESCRIPTION	2-1
	2.1 Specification of the Environment	2-1
	2.1.1 Bathymetry	2-2
	2.1.2 Bottom Reflectivity	2-3
	2.1.3 Sound-Speed Structure	2-3
	2.1.4 Surface Wave Height	2-4
	2.1.5 Volume Attenuation	2-4
	2.2 The Propagation-Loss Model	2-4
	2.2.1 Model Requirements	2-5
	2.2.2 Model Rationale	2-6
	2.3 Implementation of the Model	2-10
	2.3.1 Treatment of the Receiver	2-12
	2.3.2 Treatment of the Source	2-15
	2.3.3 Treatment of Range-Dependence	2-19
	2.3.4 Smoothing of Results	2-20
	2.4 Cycling Capabilities	2-22
	2.4.1 Receiver Data	2-23
	2.4.2 Water-Mass Data	2-23
3	DETAILED IMPLEMENTATION	3-1
	3.1 The Environment	3-1
	3.1.1 Bathymetry	3-1
	3.1.2 Bottom Classes	3-3
	3.1.3 Sound-Speed Structure	3-3
	3.1.4 Surface Wave Height	3-4
	3.1.5 Volume Attenuation	3-4
	3.2 The Propagation-Loss Model	3-4
	3.2.1 Treatment of the Receiver	3-5
	3.2.1.1 The Ray Trace	3-7
	3.2.2 Treatment of the Source	3-11
	3.2.3 Range Dependence	3-18
	3.2.4 The Smoothing Algorithm	3-21

CONTENTS (Cont.)

		Page
4	MODEL EVALUATION	4-1
4.1	Test Case 1	4-6
4.1.1	Case 1A - Flat Bottom	4-6
4.1.1.1	Case 1A1 - 2500-ft Receiver	4-6
4.1.1.2	Case 1A2 - 10000-ft Receiver	4-7
4.1.2	Test Case 1B - Shoaling Bottom	4-8
4.1.2.1	Test Case 1B1 - 2500-ft Receiver	4-8
4.1.1.2	Test Case 1B2 - 10000-ft Receiver	4-9
4.1.3	Test Cases 1D1 and 1D2 - Broad Ridge, 2500 and 10000-ft Receivers	4-9
4.2	Test Case 2	4-29
4.2.1	Test Case 2A1 - Flat Bottom, 3000-ft Receiver	4-29
4.2.2	Test Case 2D1 - Broad Ridge, 3000-ft Receiver	4-30
4.3	Test Case 3	4-38
4.3.1	Test Cases 3A1 and 3A2 - Flat Bottom, 1000- and 5000-ft Receivers	4-38
4.3.2	Test Cases 3C1 and 3C2 - Gradual Downslope 1000- and 5000-ft Receivers	4-39
4.4	Test Case 4	4-53
4.4.1	Test Cases 4A1 and 4A2 - Flat Bottom, 4000- and 12000-ft Receivers	4-53
4.4.2	Test Cases 4D1 and 4D2 - Broad Ridge, 4000- and 12000-ft Receivers	4-54
4.5	Test Case 5	4-69
4.5.1	Test Cases 5A1 and 5A2 - Flat Bottom, 500- and 2000-ft Receivers	4-69
4.5.2	Test Cases 5C1 and 5C2 - Gradual Downslope, 500- and 2000-ft Receivers	4-70

CONTENTS (Cont.)

		Page
4.6	Summary of Identified Model Deficiencies	4-84
4.6.1	Angular Discretization	4-84
4.6.2	Receiver Coupling to Diffraction Fields of Modes	4-85
4.6.3	Coherent Effects at the Receiver	4-85
4.6.4	Extended Surface-Image Interference at the Source	4-86
4.6.5	Surface-Image Interference on Refracted Modes	4-86
4.6.6	Improved Diffraction Fields	4-87
4.6.7	Double-Channel Environments	4-88
4.6.8	Asynchronous Changes in Bathymetry and Water Mass	4-88
4.6.9	Transmission-Loss Smoothing	4-89
4.6.10	Summary of Likely Problem Areas	4-90
4.7	Statistical Results	4-91
4.7.1	Distribution Functions for Model Error	4-91
4.7.2	Statistics of Model Error	4-99
4.8	Summary of Model Evaluation	4-102
4.8.1	Computer Running Times	4-103
REFERENCES		R-1

ABSTRACT

This report documents the development and evaluation of a new long-range propagation-loss model - ASTRAL (ASEPS Transmission-Loss). ASTRAL has been developed to meet the need for an accurate, high-speed fully automated model capable of predicting range-smoothed (over 30-40 nm) propagation loss in a range-dependent environment. It is being incorporated in the ASEPS Fleet Support model at FNWC Monterey, however it may also be used independent of ASEPS in a stand-alone mode.

ASTRAL assumes adiabatic invariance in propagating mode-like envelopes through a fully range-dependent environment. Initial excitation of these quasi-modes (by the receiver, invoking acoustic reciprocity) can include ray-angle conversion effects on a slope immediately in front of the receiver. The mode envelope functions are computed for several source depths and frequencies simultaneously and include surface-image interference as well as diffraction.

To evaluate the model's accuracy, exhaustive comparisons between ASTRAL and parabolic-equation (PE) results have been made for water-borne paths in identical, highly range-dependent environments. Virtually all of the significant discrepancies have been identified with design limitations of the model. Few, if any, discrepancies result from the adiabatic-invariance assumption. From the comparisons with PE the error in an ASTRAL prediction given the correct environmental inputs appears to be approximately normally distributed with a mean of 0 to -1 dB (slightly overestimating the loss) and a standard deviation of 1.5 to 2.0 dB.

Across the set of 180 cases considered in the comparisons ASTRAL is five orders of magnitude faster than PE on comparable computers and three orders of magnitude faster (and cheaper) than PE when run on the Texas Instruments Advanced Scientific Computer at NRL. A companion report (Volume II) documents the ASTRAL computer code.

Section 1
Introduction

This report is the first of two volumes documenting a new long-range low-frequency propagation-loss model developed by Science Applications, Inc. for the Long-Range Acoustic Propagation Project (LRAPP - NORDA Code 600) under Contract N00014-77-C-0502. This volume contains a detailed description of the physics and mathematics represented by the model and the results of the basic evaluation effort. Volume II* describes the computer code including detailed flow charts, running instructions, and sample output.

1.1 BACKGROUND

For a number of applications, LRAPP has long recognized the need for a fast, accurate long-range propagation-loss model for range-dependent environments. The FACT Model (Spofford, 1974 and Baker and Spofford, 1974) met this objective for range-independent environments quite adequately. A number of attempts to extend FACT's results to range-dependent environments have met with limited success. The fastest of these (using Ad-hoc corrections of the form A+BLogR) was incorporated in the ASEPS and TASSRAP Fleet Support models at FNWC Monterey. A slower but more detailed extension was developed by AESD for the SASS Phase B Scenario. A series of evaluations of these models against measured data revealed a number of critical limitations.

With the advent of the Parabolic Equation (PE) Model a highly accurate control solution was available for fully range-dependent environments. PE could not meet the

*Blumen and Spofford (1978).

running-time and automation requirements; however, it did provide "correct" answers for a much wider range of environments than available measurement sets and without their environmental input uncertainties.

Confronted with the need for a more accurate high-speed model and no available model to meet this need, LRAPP considered several development alternatives and selected that proposed by SAI. The thrust of the SAI approach was to exploit the unique opportunities offered by the requirements which would permit both accuracy and speed. These were: the adequacy of a range-smoothed transmission loss (intensity averaged over convergence-zone spacings), and the typical operating mode of estimating loss along several bearings from a specified point. The first requirement permitted consideration of some approximate techniques for obtaining range-averaged intensities, and the second offered the opportunity for substantial savings in running time by saving certain results from one bearing for subsequent bearings. The resulting SAI model as described in this report represents the first attempt to design from the ground up a model which might take full advantage of these opportunities.

1.2 STRUCTURE OF REPORT

The following section contains a qualitative description of the model physics and approach for the reader who has no need for a detailed description, and an introduction to the complete description contained in Section 3 (including all pertinent equations). Section 3 also describes the detailed implementation as each of the technical questions is

resolved. The program structure and flow of Volume II refer directly to these equations. Section 4 contains a first evaluation of the model physics in terms of direct comparisons with PE results (appropriately smoothed) for identical environments. Sources for the observed differences are identified in terms of recognized model limitations. Model accuracy is quantitatively assessed as a function of figure-of-merit, source depth, and frequency. Running times and costs for PE and ASTRAL are compared for appropriate computers.

1.3 ACKNOWLEDGMENTS

This model was developed as part of LRAPP's Modeling Program under the cognizance of CDR J. E. Paquin. The encouragement of CDR Paquin and LRAPP's Director, Dr. R. D. Gaul are gratefully acknowledged. Much of the success of this technique relies on the ability to store and re-use key features of the acoustic field. This idea was originally suggested by Mr. K. O. Osborne, II of Ocean Data Systems, Inc. The able assistance of Mr. Osborne and his staff have made the transition of this model to FNWC a smooth and efficient process.

The technical approach represented in the model was derived largely from the highly successful adiabatic normal-mode work of Mr. D. F. Gordon at NOSC. Comparisons with high-frequency PE results were only possible as a result of the pioneering work of Mr. H. K. Brock of NRL in implementing PE on the Texas Instruments Advanced Scientific Computer.

Finally, it is a pleasure to acknowledge the support from within SAI in program development, lead by Dr. R. G. Stieglitz as assisted by Messrs. P. C. Broe and W. E. Renner. Ms. L. S. Blumen of SAI co-authored Volume II and is wholly responsible for its clarity and utility.

Section 2
Basic Model Description

This section describes the model in terms of its overall structure and the basic approach being employed. Section 3 translates this approach into the detailed implementation description including all pertinent equations and approximations. Section 2.1 describes the environmental "model"--that is the input required and the implicit treatment of that input. Section 2.2 summarizes the approach to solving for the acoustic field in that environment.

2.1 SPECIFICATION OF THE ENVIRONMENT

The model is capable of treating an environment where the following properties are a function of range: water depth, bottom reflectivity, sound-speed profile, and surface wave height. The specific treatment of each of these parameters is described in the following subsections. A typical scenario which the model can treat might be as follows:

- A receiver mounted on a bottom which locally has a gradual slope (say 2°) for 2 nm followed by a steep slope (say 10°) to the basin floor

- Depth and reflectivity changes occuring irregularly every 20 to 60 nm

- Significant changes in sound-speed profile and sea state every 100 to 300 nm

- Propagation loss required from this receiver to 3 source depths for 4 different frequencies to a range of 1500 nm along several bearings where the environments may gradually change from bearing to bearing

2.1.1 Bathymetry

From the receiver, at range zero the bathymetry is described in terms of the immediate slope, the "near-field" bathymetry, and the distant or far-field bathymetry. For a bottom-mounted receiver, the immediate slope (~first mile or less) along the bearing of interest is specified to eliminate paths arriving at the receiver at angles coming up through the bottom. Possible "bottom-baffle" or enhancement effects at the receiver are not currently included although they could be, if warranted. If the receiver is suspended above the bottom this slope is not relevant.

The mean bottom characteristics from a range of a few miles to tens of miles can be prescribed in terms of the "near-field" bathymetry. Specifically a slope and its extent are defined to allow for the conversion of rays leaving the receiver to other angles upon one or more reflections from the slope. The immediate and near-field bathymetry data are usually taken from detailed bottom charts.

Beyond the end of the near-field bathymetry, the water depth is described as a step function in range as often as specified by the user. These values are presently

generated by a retrieval package from a digitized and gridded bathymetric data bank. Present banks typically have 1-degree square resolution so steps might be anticipated every 30 to 60 nm. Higher resolution banks are currently in development and should not reduce model efficiency.

2.1.2 Bottom Reflectivity

The bottom reflectivity both on the near-field slope and the far-field steps can be specified for each interval in terms of the FNWC 5-class reflection-loss curves (Bassett and Wolff, 1970). For purposes of computational speed, these curves have been approximated by three-segment functions in angle for each class and frequency. Transitions between curves across frequency domains have been smoothed to yield a continuous function of both frequency and grazing angle for each bottom class. These curves are described in detail in Section 3.1.2. An option for perfect reflectivity at all angles and frequencies has been permitted for possible use on steep near-field slopes where near-perfect reflectivity has occasionally been observed.

2.1.3 Sound-Speed Structure

Sound-speed profiles are specified over discrete range intervals (similar to, though on a different mesh from, the water depth). These are usually generated by extracting profiles along the bearing from a sound-speed data bank (currently with 5-degree square resolution). These profiles may have arbitrary complexity within limits on the number of points (see Volume II), however their complexity may not be fully treated by the model (see discussions in Sections

3.2.2 and 4.6.7). The transition from profile to profile is smoothed in the output as described in Sections 2.3.4 and 3.2.4.

2.1.4 Surface Wave Height

The surface wave height (rms) may be specified as often as the sound-speed profile (consistent with current data banks). This is used only for the computation of rough-surface losses. Presently a "dummy" routine is used which assumes zero loss under all conditions. Rough-surface loss expressions currently under development for inclusion in the FACT Model will be incorporated when approved. This will require minor program modifications.

2.1.5 Volume Attenuation

This model uses the same volume-attenuation function as FACT

$$\alpha_v(f) = 0.125(f/1000)^2 \text{ dB per nm}$$

for frequencies, f, less than 1000 Hz. (It is not envisioned that this model will be used above 1000 Hz.) These values are currently being scrutinized since they are approximately half those of Thorp (1967). If revised values are approved by LRAPP they can be incorporated with little difficulty.

2.2 THE PROPAGATION-LOSS MODEL

This section outlines the requirements for the model and the rationale for the particular approach selected.

The approach is then described in terms of the treatments of the receiver, the source, range-dependent sound-speed profiles and water depths, non-spreading losses (surface, volume and bottom attenuations), and smoothing algorithms to reduce transition artifacts. A final subsection describes the efficiencies attained by saving certain computed quantities from one run for subsequent runs.

2.2.1 Model Requirements

The highest priority for the new model was accuracy. Given an accurate description of the environment, the model should be capable of predicting transmission loss with a mean error of less than 3 dB and a comparable rms error. Inaccuracies attributable to uncertainties or errors in describing the environment contribute to an additional error budget. The objective in these phases of model development and evaluation was to shift the overall accuracy burden from the acoustic model to the environmental inputs.

The next priority was model running time. A goal was set that the model should be able to predict propagation loss for three source depths and three frequencies on a track 1000 nm long in one CPU second of a CDC 6000 Series Computer.

The final major requirement was more of an opportunity than a constraint. The propagation loss should be described in terms of its mean intensity, averaged over distances comparable to convergence zones. This description is adequate for two reasons. First, the model is used as a component in an ambient-noise model where surface ships

are treated as a continuous distribution of sources. The mean noise from a given direction may be computed by using this range-averaged intensity. Second, for propagation of signals, variations about this mean are traditionally treated statistically in the passive sonar equation. Clearly, such a range average can be computed from detailed estimates; however, as described subsequently, the lack of a requirement for the detailed loss characteristic permits the formulation of more efficient and less complicated models.

Additional requirements in terms of core size, disc usage and other computer-related items were imposed by the FNWC operating environment. These have had a minimal impact on the model development. Residual problems in this area have been ably dispatched by the ODSI staff under Mr. Osborne's direction.

2.2.2 Model Rationale

Because only range-averaged transmission loss was required, it appeared that some form of ray or wave formulation was possible following either Smith (1974) or Gordon (1972), respectively. In the ray formulation the average of intensity over range is computed for separate ray bundles and summed. In the wave formulation the normal modes are summed on an rms or incoherent basis.* For range-independent environments when appropriate surface-image and diffraction effects are added to the ray treatment, the results are essentially equivalent.

Smith and Gordon extended their techniques to range-dependent environments by identifying new rays and

*Weinberg and Burridge (1974) extended the modal approach to a coherent sum and allowed for horizontal refraction as well.

modes, respectively, via the adiabatic mapping (Milder, 1969). For rays this requires conservation of the phase integral from one domain to another, and for modes the correspondence of mode number (which in the WKB approximation equates to the phase integral). The most attractive feature of this approach is that it requires no information on how the environment changed, only its specification at ranges of interest. Milder has shown that this approximation is valid if the environment changes slowly enough--specifically over several cycle distances for rays and somewhat less abruptly for individual modes. This apparent contradiction merely reflects the correspondence between rays and groups of modes so that mode number variations must be comparable to group dimensions in order to affect rays significantly.

The validity of the adiabatic approximation has been extensively examined both theoretically (Uberall, et al., 1975) and experimentally (Gordon, 1972). In situations involving steep slopes or strong oceanographic fronts, it can be expected to break down. It is for this reason that the reflection from the slope directly in front of the receiver is not treated adiabatically. In the case of strong fronts, the breakdown of adiabatic invariance implies that the result will be sensitive to the precise positioning of the front with respect to the various rays of interest. Present oceanographic data banks do not have sufficient resolution to warrant such a detailed treatment. Hence to the extent that the adiabatic result resembles the average over possible front locations the approximation may be considered the best guess given the environmental uncertainties. Nevertheless, the inherent limitations of the adiabatic approximation must not be overlooked.

The ASTRAL model assumes adiabatic invariance in the ray (strong) sense once the slope in front of the receiver has been treated. A fan of rays is traced, approximately, from the receiver to the end of the near field bathymetry, converting in angle upon reflection as appropriate. At this range they are identified (by turning-point sound speed or "phase velocity") with a set of modes (or a ray-equivalent) contributing the energy in the original bundle (less attenuation losses) to the mode's excitation. The mode then propagates adiabatically in range, changing phase velocity to conserve the phase integral as the sound-speed profile and/or water depth changes.

Modes are assigned depth functions which approximate the envelope of the oscillatory depth functions of true normal modes. The envelope corresponds to the WKB envelope, extended via Airy functions at turning points and including surface-image interference very near the surface. At each range of interest the mode's contributions for various depths and frequencies are computed and summed over all remaining modes.

In this way the range-averaged propagation loss is obtained. If detailed true normal modes had been used, this would equate to their rms sum--thus removing all convergence zones. If rays had been used, each mode corresponds to the range averaged contributions of the aperture of rays about the particular ray equivalent.

An alternative way of viewing this model is as a logical extension of the simple conservation of energy model. In a homogeneous medium of depth, D, with boundaries which are perfectly reflecting for grazing angles less than

θ_{max} and perfectly absorbing for greater angles, the range- (and depth-) averaged intensity, I, as a function of range, r, is easily shown to be

$$I(r) = \frac{2}{rD} \sin\theta_{max} .$$

If the aperture from $-\theta_{max}$ to $+\theta_{max}$ were partitioned into subapertures of width $(\Delta\sin\theta)_m$ then

$$I(r) = \sum_m \frac{(\Delta\sin\theta)_m}{rD}$$

$$= \frac{1}{r} \sum_m (\Delta\sin\theta)_m \cdot \phi_m^{(0)}(z),$$

where $\phi_m^{(0)}(z)$ is the contribution from aperture or "mode" m to the depth z. $(\Delta\sin\theta)_m$ represents the excitation of this mode at the origin of rays (source or receiver) and corresponds to the solid angle (hence energy) propagating with mode m. The 1/r term merely reflects the cylindrical spreading for the mode.

In this simple example $\theta_m^{(0)}(z)$ is equal to 1/D for all m and z. If, however, refraction were introduced and each mode had its own upper and lower turning points (z_m^{up}, z_m^{dn}), respectively, then a logical extension would be to set

$$\phi_m^{(1)}(z) = \frac{1}{z_m^{dn} - z_m^{up}} \qquad \text{for} \quad z \varepsilon [z_m^{up},\ z_m^{dn}]$$

$$= 0 \qquad \text{for} \quad z \notin [z_m^{up},\ z_m^{dn}] .$$

Note that again ϕ_m is normalized (i.e., integrates over z to 1). This eigenfunction represents the contribution from mode m averaged over all depths between the turning points. The WKB improvement $\phi_m^{(2)}(z)$ takes the focusing effects of refraction into account by weighting $\phi_m^{(1)}(z)$ by $1/\tan\theta(z,m)$ where $\theta(z,m)$ is the ray-equivalent angle at depth z via Snell's Law and the phase velocity.

These eigenfunctions have no apparent frequency dependence (being in fact the infinite-frequency limit); hence they are further modified with diffraction corrections to be finite at turning points and to extend into shadow zones, and with surface-image interference. Finally, volume, surface and bottom losses are accumulated continuously for each mode per unit distance. The boundary losses are accumulated at a rate appropriate to the "bounce" loss of the ray equivalent. This formulation is described more completely in the following subsection with mathematical details reserved for Section 3.

2.3 IMPLEMENTATION OF THE MODEL

The range-smoothed intensity, I, as a function of range, r, frequency, f, and source depth z is given by

$$I(r,f,z) = \frac{1}{r} \sum_m \hat{\phi}_m(f) \cdot \phi_{m'(r,m)}(r,f,z) \cdot 10^{-\alpha_m(r,f)/10}$$

The $\hat{\phi}_m$ are the excitation of eigenfunction m at the receiver (including near-field slope coupling--hence the frequency dependence). The evaluation of $\hat{\phi}_m$ is described in Section 2.3.1. The source coupling is through ϕ_m (Section 2.3.2) where mode m couples to m'(m,r) through adiabatic invariance. In a true adiabatic normal-mode formulation m'(m,r) = m. Because the "modes" here are actually sets of modes or ray bundles, they are defined in terms of certain angles, θ_m, which may not correspond adiabatically. Hence m' may differ from m. The r-dependence of both θ_m and m is meant to indicate the influence of the sound-speed profile and the water depth (see Section 2.3.3 for details). The attenuation term, α_m, contains all volume and boundary losses.

The procedure may be summarized as follows:

(1) Trace rays, corresponding to mode bundles from the receiver to the end of the near-field bathymetry, slope-converting angles if necessary and accumulating all losses

(2) At the end of the near-field bathymetry identify these rays (through their phase velocity) with specific modes, m, thus obtaining $\hat{\phi}_m(f)$

(3) Propagate this set of modes computing their contributions to each depth for each frequency with appropriate attenuation

(4) When the water mass (sound-speed profile) and/or the depth changes, re-normalize the modes, compute new phase integrals, and new coupling--m'(m)

(5) Continue this procedure computing I(r) as often as required until a maximum specified range is reached or all modes are effectively extinguished by bottom losses

2.3.1 Treatment of the Receiver

The receiver, as mentioned previously, may be either bottom-mounted or suspended over a locally flat or sloping bottom. If bottom-mounted it may have an immediate (interface) slope which obscures paths at shallower angles. For the sound-speed profile applicable at the receiver, a set of angles $\{\theta_n\}$ has been defined at the sound-speed minimum (axis) for purposes of mode definition (as described in the next section). For those rays reaching the receiver depth, the corresponding angles θ_n^R are identified via Snell's Law. The solid-angle contribution to each mode at the receiver is taken to be

$$(\Delta \sin\theta_R)_n = \sin\theta_n^R - \sin\theta_{n-1}^R \ .$$

If the receiver is suspended over a flat bottom these values become the mode excitation.

For a bottomed receiver the immediate slope precludes angles shallower than it. For a receiver suspended over a sloping bottom all rays at $\pm\theta_n^R$ are considered. In either event, each allowed ray, θ_n^R, is "traced" to the end of the near-field slope. This trace is done approximately to conserve running time. It is assumed that any ray which reflects from the bottom will do so at sufficient depths that the deep (pressure) gradient may be assumed with minimal error. For each of the rays (θ_n^R) the cycle distance, or period, has been computed assuming an infinitely deep ocean with a pressure gradient at great depths. An approximate trajectory is used equivalent to a circular arc of the proper period between the lower turning point and upper turning point or the surface.

This assumption permits a rapid computation of intersection points with the bottom. At each intersection the grazing angle is computed, the appropriate reflection loss noted, and the ray angle reduced (or augmented) by twice the slope angle (corresponding to specular reflection). This new ray is assigned a turning-point sound speed and axis angle, via Snell's Law, and a corresponding period by interpolation in the table of periods versus axis angle, θ_n. It propagates with additional reflection if appropriate until the end of the near-field bathymetry is reached or until the ray is either turned back or reduced by bottom attenuation to an insignificant level.

If the ray reaches the end of the near-field bathymetry, its phase velocity or turning-point sound speed, $\bar{c}$, is used to assign it to a particular mode m, where

$$\bar{c}_{m-1} < \bar{c} \leq \bar{c}_m ,$$

and

$$\tilde{c}_m = c(\text{axis})/\cos\theta_m \ .$$

Note that this m may not be the same as the ray's original mode equivalent, n. This ray will now contribute energy to mode m of magnitude $(\Delta\sin\theta_R)_n$ reduced by appropriate volume and boundary losses.

(This treatment is non-adiabatic in the sense that the (approximate) points of intersection are computed and the ray may or may not reflect from the bottom depending on details of the specific case. The adiabatic treatment of this problem would assume many bounces and a continuous change in ray angle or turning-point sound speed such that over a ray's period it would change angle on the bottom by twice the slope angle. As the slope becomes more and more gradual the detailed treatment should approach the adiabatic result.)

After all rays have been traced the excitation of each mode at the end of the near-field bathymetry, $\hat{\phi}_m(f)$, has been accumulated as contributions from various rays. Frequently one mode may be excited by several rays, and some modes may have no excitation. At this point the subset of modes with non-zero excitation is identified for subsequent propagation. Note that modes are now identified only in terms of their turning-point sound speeds, $\tilde{c}_m$, so any distinction between up- and down-going paths at the receiver is lost (or more precisely, implicitly contained in the $\hat{\phi}_m$).

2.3.2 Treatment of the Source

As is generally the case in treating range-dependent environments, the receiver is considered to be fixed in that environment and we are interested in the propagation loss from sources at fixed depths and a number of ranges. Acoustic reciprocity is invoked and the receiver is considered to be the source of energy sampled at various ranges and depths corresponding to source positions. In this document "source" will always be used to refer to these positions. The coupling of the source to the acoustic "field" of the receiver is then expressed in terms of the intensity eigenfunctions ϕ_m.

The amplitude of the intensity eigenfunction in the infinite frequency limit at depth z is proportional to

$$\frac{1}{\tan\theta(z,\tilde{c}_m)} ,$$

where $\theta(z,\tilde{c}_m)$ is the ray-equivalent's angle via Snell's Law:

$$\cos\theta(z,\tilde{c}_m) = \frac{c(z)}{\tilde{c}_m} .$$

c(z) is the sound speed versus depth. The constant of proportionality must be chosen to normalize ϕ_m in depth:

$$1 = \int_z \phi_m(z)dz$$

which leads to

$$\phi_m(z) = \frac{2}{P_m \tan\theta(z,\tilde{c}_m)} ,$$

where P_m is the ray's cycle distance. Note that in a homogeneous medium of depth D, $\theta(z,\tilde{c}_m) = \theta_m$, and $P_m = 2D/\tan\theta_m$; hence $\phi_m(z) \to 1/D$ as expected. When new water depths occur within the same water mass (i.e., sound-speed profile), the normalization must be recomputed. To facilitate this the ray cycle distances (P_m^∞) for the infinitely deep ocean are saved and modified assuming a pressure gradient from the bottom depth to the turning point.

At the ray-equivalent's turning point(s), $\theta = 0$ and the infinite-frequency ϕ_m become infinite. The eigenfunction is extended through the turning points using a squared Airy function whose argument depends on the frequency and the sound-speed gradient at the turning point. Specifically for a given frequency and turning point gradient, g, there is an angle $\hat{\theta}$ below which the geometric result diverges from the proper finite-frequency behavior:

$$\hat{\theta} \simeq (3|g|/4f)^{1/3} ,$$

corresponding to the last point of rms interference between the up- and down-going rays defining the mode. If the gradient is constant around the turning point the depth $\hat{z}$ of this transition point is

$$\hat{z} = z_T \pm \frac{\tilde{c}_m \hat{\theta}^2}{2g},$$

with the sign depending on whether z_T is an upper (-) or lower (+) turning point.

The eigenfunction is then extended as follows

$$\phi_m(z) = \frac{2}{P_m} \cdot \begin{cases} \dfrac{1}{\tan\theta(z,\tilde{c}_m)} & \theta > \hat{\theta} \\ \dfrac{1}{\tan\hat{\theta}} \left[\dfrac{Ai(-x)}{Ai(0)}\right]^2 & \theta < \hat{\theta} \text{ or shadow} \end{cases}$$

where Ai is the Airy function and its argument is proportional to the distance from the turning point:

$$x = 1.77 \; \frac{z - z_T}{\hat{z} - z_T} \quad .$$

Note that the transition point ($\hat{\theta}$) is a function of both the frequency and the turning-point gradient.

Eigenfunctions are also modified to include effects of surface-image interference. For surface-reflected modes

$$\phi_m \rightarrow \phi_m \cdot 2 \sin^2\psi_0 \quad \text{for } \psi_0 < 3\pi/4 \quad ,$$

where

$$\psi_0 = \frac{2\pi f}{c(0)} z \sin\theta(0,\tilde{c}_m)$$

This simulates the surface null and first constructive peak in the image-interference pattern. For $\psi_0 \geq 3\pi/4$ (i.e., beyond this point of rms summation) no correction is applied. For non-surface-reflected modes (that is, modes with upper turning points

$$\phi_m(z) \rightarrow \left(\sqrt{\phi_m(z)} - \sqrt{\phi_m(-z)}\right)^2.$$

This approximates the interference of a diffraction field from an out-of-phase image source (or receiver) in a reflected medium.

For each mode the attenuation losses are accumulated continuously. The losses per reflection from the surface and bottom (as functions of grazing angle, frequency and sea-state/bottom-class) are determined. From the ray-equivalent's cycle distance a decay rate is computed such that the loss per bounce is removed over one cycle distance. Volume losses are added proportional to range (not path length, but somewhat consistent with the way they are measured).

This concludes the present treatment of eigenfunctions. Two areas for possible improvement should be mentioned:

1. For very low frequencies and/or very shallow angles, the phase term ψ_0 can be more accurately expressed as

$$\psi_0 = 2\pi f \int_0^z \frac{\sin\theta(\zeta,\tilde{c}_m)d\zeta}{c(\zeta)} .$$

There have been no cases examined to date where this appears to be necessary.

(2) In sound-speed profiles with one or more interior relative maxima, it is possible for low order modes to have several turning points. The present treatment considers only the upper and lower extreme turning points and extends the field across internal "shadow" regions without exponential decay. This is a more serious limitation; however, it is consistent with the limited overall treatment of multiple-channel profiles. In one of the test cases (see Section 4) this has led to a significant error. This subject is discussed in more detail subsequently.

2.3.3 Treatment of Range-Dependence

Given a set of propagating modes at various levels of excitation (and decay) we wish to change the sound-speed profile and/or the water depth. (If the bottom-reflectivity is changed it is appropriately noted in changed decay rates for the bottom-reflected modes.) The energy from one mode m will then be treated as coupling to a new mode m'. The coupling is assumed to be adiabatic--that is the phase integral

$$\psi_m = \int_z \frac{\sin\theta(z,\check{c}_m)}{c(z)}\, dz$$

will be conserved:

$$\psi_m^0 = \psi_{m'} \quad ,$$

where the superscript zero denotes the value at the receiver.* In practice a fan of rays at the axis of each region has already been considered and m'(m) will be such that

$$\psi_{m'-1} < \psi_m^0 \leq \psi_{m'} \quad .$$

Clearly if only the water depth changes then m may change only for modes which interact with the bottom in one or both regions. When the sound-speed profile changes any of the modes may be affected.

To facilitate these calculations the infinite-ocean values of the phase-integral, ψ_m^∞, are computed, and for each water depth encountered are modified assuming a pressure gradient between their turning point and the bottom. Modifications for new water depths are (as for the eigenfunctions) rapid and straightforward.

2.3.4 Smoothing of Results

As defined above, the transmission-loss model will provide values at least as often as requested by the user (typically 30 nm). Within each region of given environmental

*More precisely, ψ_m^0 will be the phase at the end of the near-field bathymetry.

parameters (sound-speed, water-depth and reflectivity) values will be computed on an equispaced range mesh approximating a user specified sampling rate. While the variations from region to region are treated adiabatically, the net effect from the endpoint of one region to the first point in the next region can be unrealistically abrupt (when compared, for example, with solutions generated by PE).

A thorough solution to this problem, assuming the validity of the adiabatic approximation would be to track the depth-dependence of the individual mode-like eigenfunctions through a transition region. This would require a detailed description of the evolution of the environment and a corresponding series of mode calculations. Such environmental data are not generally available, and the necessary mode calculations would seriously degrade the model's efficiency.

An approximate implementation of the above approach would be to define a transition region within which the values of each eigenfunction at the desired depths and frequencies varied smoothly (e.g., linearly) between their values in the two regions. This approach may be worth more investigation since it would probably not require excessive running times. The key issue would be to determine appropriate transition regions.

For the present model a similar but much simpler smoothing algorithm has been developed which works only on the output transmission-loss curve. First, a discontinuity is identified in terms of a specified change in level from a value based on linear extrapolation of the two preceding points on the transmission-loss curve. The change is then identified (in the following order) with either:

(1) A change in water mass

(2) A change in water depth

(3) Neither of the above

In the event of a water mass change a transition region is defined approximately midway into both water masses and the transmission loss is linearly interpolated from one end to the other. If only the water depth changed, the value at the discontinuity is linearly interpolated between the values at the adjacent points. (This is meant to simulate a more continuous change in water depth.) If neither (1) nor (2) has occurred no smoothing is applied. The discontinuity is then most likely due to a change in reflectivity and may be a correct representation. The detailed implementation of this smoother is described in Section 3.2.2. It may be easily circumvented on option, and if a satisfactory substitute is found it can be easily removed.

2.4 CYCLING CAPABILITIES

In the operational environment it is anticipated that the model will be required to predict propagation loss for many radials (say 72 at a 5-degree spacing in azimuth) from a particular receiver. Since the present water masses are defined by 5-degree squares in latitude and longitude, each one may be traversed several times by various radials. Similarly each near-field bathymetry sector may apply to several radials. Hence significant running time reductions appeared to be achievable if certain computed information from one radial were saved for subsequent radials rather than recomputed. This information falls into two categories:

receiver and water-mass related data. In general, when these data are required, a check is made to determine whether they have been previously computed. If they have, they are used directly, if not they are computed, stored, and flagged as available.

2.4.1 Receiver Data

Since the receiver is always in the same water mass, the modes that it excites, and the corresponding solid angles in the absence of any bathymetry effects are computed once and saved. For a given near-field bathymetry sector (point-slope and maximum range plus basin depth), the approximate ray-trace information relating to slope conversion and ultimate mode excitation can also be saved for each of the ray apertures possible at the receiver. When the immediate slope at the receiver is introduced, apertures corresponding to rays going directly into the bottom are eliminated before summing for the total excitation of each mode.

2.4.2 Water-Mass Data

The first time a sound-speed profile is encountered the following information is computed for each mode:

(1) Phase velocities

(2) Infinite-ocean phase integrals

(3) Infinite-ocean cycle distances (periods)

(4) Upper and lower (infinite ocean) turning points

(5) Depth-unnormalized eigenfunctions for each source depth and frequency

(6) Surface-reflection losses for each frequency

Also the index of the first surface-reflected mode is computed and stored.

As already mentioned these data are used along a single track as the water depth changes within a water mass by modifying phase integrals, cycle distances, and eigenfunctions accordingly. They are also made available for use on subsequent radials in the same way. The running time savings that this approach offers vary substantially with the complexity of the profiles and the density of radials. Typical savings might be 10% to 20%, with 50% savings possible in extreme cases.

Section 3
Detailed Implementation

In the context of the approach described in Section 2, the equations, approximations, and treatments of special cases are detailed here. The subsection numbers correspond to those of Section 2. The computer code resulting from these specifications is described in Volume II.

3.1 THE ENVIRONMENT

Figure 3-1 illustrates a simplified environmental section along a single radial.

3.1.1 Bathymetry

If the receiver is bottom-mounted, the immediate bathymetry is described in terms of the receiver depth, z_R, and slope, θ_{bR} (negative-down). For both bottom-mounted and suspended receivers the near-field bathymetry is described in terms of its intercept at range zero, z_{nf} (may be positive, negative, and greater or less than z_R), its slope θ_{nf} (negative-down, greater or less than θ_{bR}, if ≤ -1.5 radians, the receiver is suspended), and its extent, r_{nf}. The rays are traced to range r_{nf} at which point the corresponding water depth is assumed and the propagation loss is computed with the eigenfunctions normalized to this depth.

For the next range point in the computation, the water depth will be taken as the depth in the piecewise constant (staircase) bathymetry region containing r_{nf}. This function is defined by its initial ranges at each step, r_e, and depths z_e. Up to 400 steps are allowed. As each new

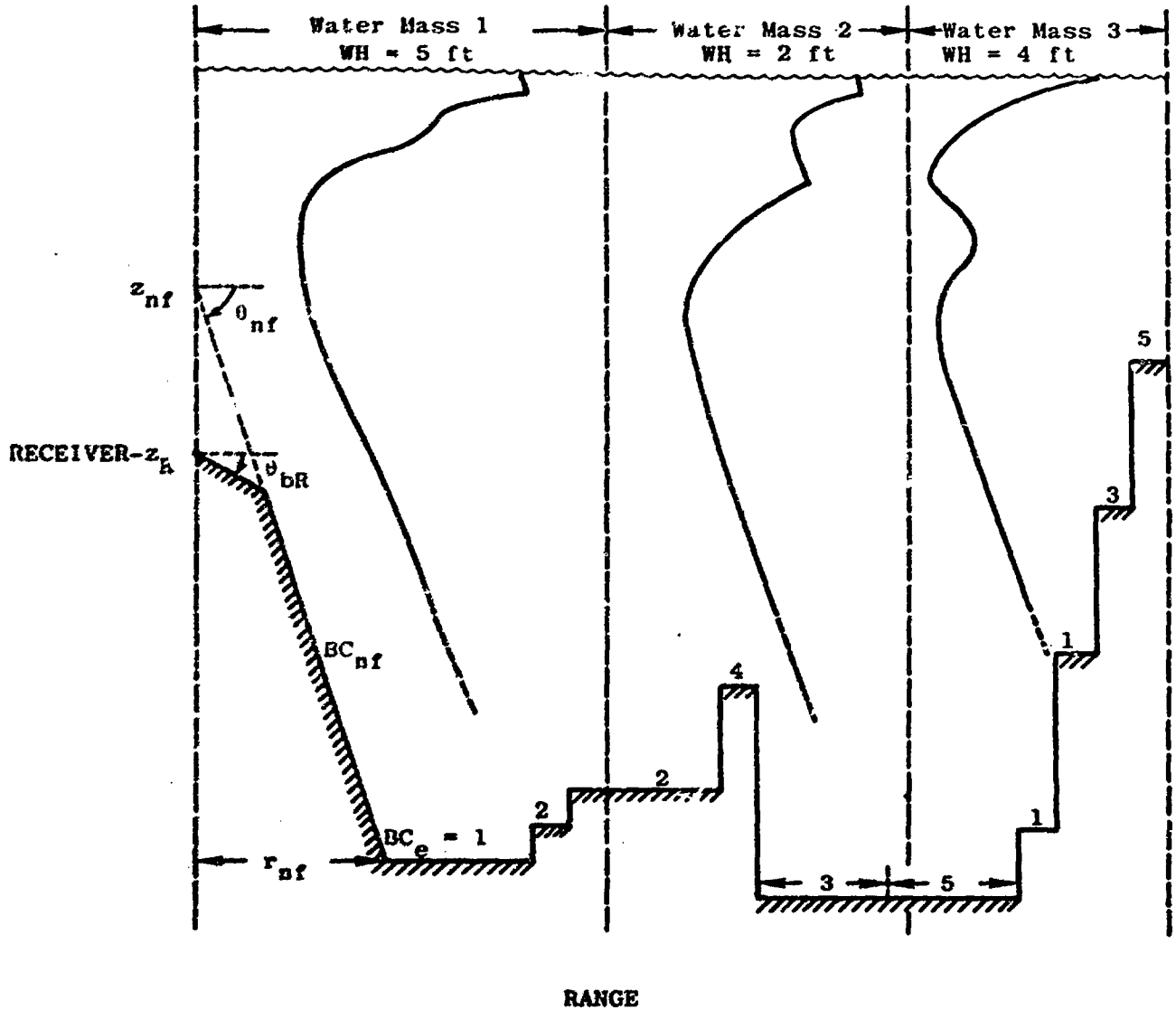

Figure 3-1. Typical Environmental Section Along a Single Radial

step is encountered a check is made to see whether it will substantially affect the eigenfunctions which are still carrying significant energy by that range. If it will, the eigenfunctions are appropriately modified and the mode-mapping via the phase integral is performed.

3.1.2 Bottom Classes

The bottom class (currently FNWC 1 through 5)* on the near-field slope, BC_{nf}, is used to determine the reflection loss for each bounce of each ray traced. Similar indices, BC_e, may be specified for each step in the bathymetry. In fact the depth may be constant and the reflectivity may change (introducing a new range r_e).

3.1.3 Sound-Speed Structure

Water masses are identified by indices, i, referring to sound speed profiles c(z) containing 25 or fewer pairs of points. A limit of 20 water masses is currently imposed. The first index (not necessarily i = 1) defines the water mass applicable at the receiver and at least to the range r_{nf}. For each new range step (r_e) an index is specified along with the water depth and bottom reflectivity. These indices can occur in any order and be repeated as often as desired. Below the last specified point on each profile, a constant (pressure) gradient ($g_p = 0.018\ sec^{-1}$) is assumed. If sound-speed values are required here they are implicitly given (in feet per second) by $c(z) = 4776 + g_p * z$ (ft).

*Presently constrained such that Class 2 maps to 1 and 5 to 4.

3.1.4 Surface Wave Height

The wave height (in feet) is specified with each water mass, i, and varies only with water mass. This wave-height is used to compute the loss for each mode and frequency, given its surface-grazing angle. Currently zero loss is used for all angles/frequencies/wave-heights.

3.1.5 Volume Attenuation

The volume loss, α_v, per unit horizontal distance is computed from

$$\alpha_v(f) = 0.125\ (f/1000)^2 \text{ dB per nm}$$

for each input frequency f. Once the bottom- and surface-loss rates are computed, they are added to α_v, multiplied by the range step, and converted to an intensity reduction for each eigenfunction.

3.2 THE PROPAGATION-LOSS MODEL

Rewriting the expression for the intensity as a function of range

$$I(r,f,z) = \frac{1}{r} \sum_m \left[\hat{\phi}_m(f) \cdot 10^{-\alpha_m(r,f)/10} \right] \cdot \phi_{m'(r,m)}(r,f,z)$$

the receiver excitation, $\hat{\phi}_m$, is grouped with the attenuation terms since the ϕ_m are reduced accordingly as the mode propagates, and only the incremental attenuation in each range step is included. That is

$$\hat{\phi}_m(f,r+\Delta r) = \hat{\phi}_m(f,r) \cdot 10^{-\tilde{\alpha}_m(r,f) \cdot \Delta r/10} ,$$

where $\tilde{\alpha}_m$ is the dB attenuation suffered by mode m as identified with m'(r,m) per unit distance in the environmental region from r to r+Δr.

3.2.1 Treatment of the Receiver

The receiver eigenfunction at range r_{nf} is given by

$$\hat{\phi}_m(f,r_{nf}) = \sum_j (\Delta \sin\theta_R)_j \cdot 10^{-\alpha_j(r_{nf},f)/10} ,$$

where the summation over j refers to those angular apertures at the receiver which, after propagation to the range r_{nf} (with or without slope conversion), will be contained in mode m. Specifically if the ray θ_{Rj} at the receiver propagates to range r_{nf} with ultimate phase (turning-point) velocity $\tilde{c}_j$, then its solid-angle contribution, $(\Delta \sin\theta_R)_j$, is assigned to mode m where

$$\tilde{c}_{m-1} < \tilde{c}_j \leq \tilde{c}_m .$$

The attenuation term represents accumulated volume and bottom losses:

$$\alpha_j(r_{nf},f) = \sum_k^{N_k} BL_k(\gamma_b(r_k),f) + \alpha_v(f) r_{nf} ,$$

where $\gamma_b(r_k)$ are the ray grazing angles at each of the N_k bottom reflections, and BL_k are the corresponding dB losses.

The procedure is to trace each ray θ_{Rj} reaching the receiver (corresponding to axis angles $\theta_{x,j}$) upward and downward from the receiver to the range r_{nf}. Attenuation losses are accumulated and mode numbers m(j) determined. If the immediate slope θ_{bR} is less than θ_{Rj} (with sign) then the ray's contribution is included:

$$(\Delta\sin\theta_R)_j = \sin\theta_R(\theta_{x,j}) - \sin\theta_R(\theta_{x,j-1}),$$

where from Snell's Law

$$\cos\theta_R = \frac{c_R}{c_x}\cos\theta_x.$$

For the shallowest ray $\theta_{\hat{j}}$ reaching the receiver

$$(\Delta\sin\theta_R)_{\hat{j}} = \sin\theta_R(\theta_{x,\hat{j}}).$$

For a suspended receiver over a locally flat bottom, the identification clearly simplifies to a Snell's Law mapping (since no angle conversion is possible). That is

$$m(j) = j.$$

This case is invoked when θ_{nf} is set ≤ -1.5 radians. The depth at the end of the near-field sector, z_{nf}, should then be set to the desired depth at the receiver, and r_{nf} should be set to some short range (> 1nm) beyond which the z_e depth will be used. For the sloping bottom, the ray trace must be executed as described below.

3.2.1.1 The Ray Trace

The ray trace is considerably simplified by assuming that the ray trajectory may be approximated by the arc of a circle, horizontal at the depth of the lower turning point and passing through the upper turning points (or surface reflections) with a separation distance equal to the ray's period. This approximation is based on the observation that below the sound-channel axis, the actual ray trajectory is very nearly circular, and the contribution to the period from the trajectory above the axis is a small fraction of the total period.

Figure 3-2 illustrates a typical geometry for a ray passing through the receiver and reflecting twice off the near-field slope. Given a ray passing through the point (r,z) with period P and upper and lower turning points z_{up} and z_{dn}, the center of the equivalent circular ray is located at (r_c, z_c) where

$$z_c = z_{dn} - \rho$$

$$r_c = r \pm \sqrt{\rho^2 - (z - z_c)^2} .$$

ρ is the radius of the circular arc:

$$\rho = \frac{1}{2(z_{dn} - z_{up})} \left[(P/2)^2 + (z_{dn} - z_{up})^2 \right],$$

and the plus sign in the expression for r_c is used when the ray angle at (r,z), θ (measured positive up) is less than

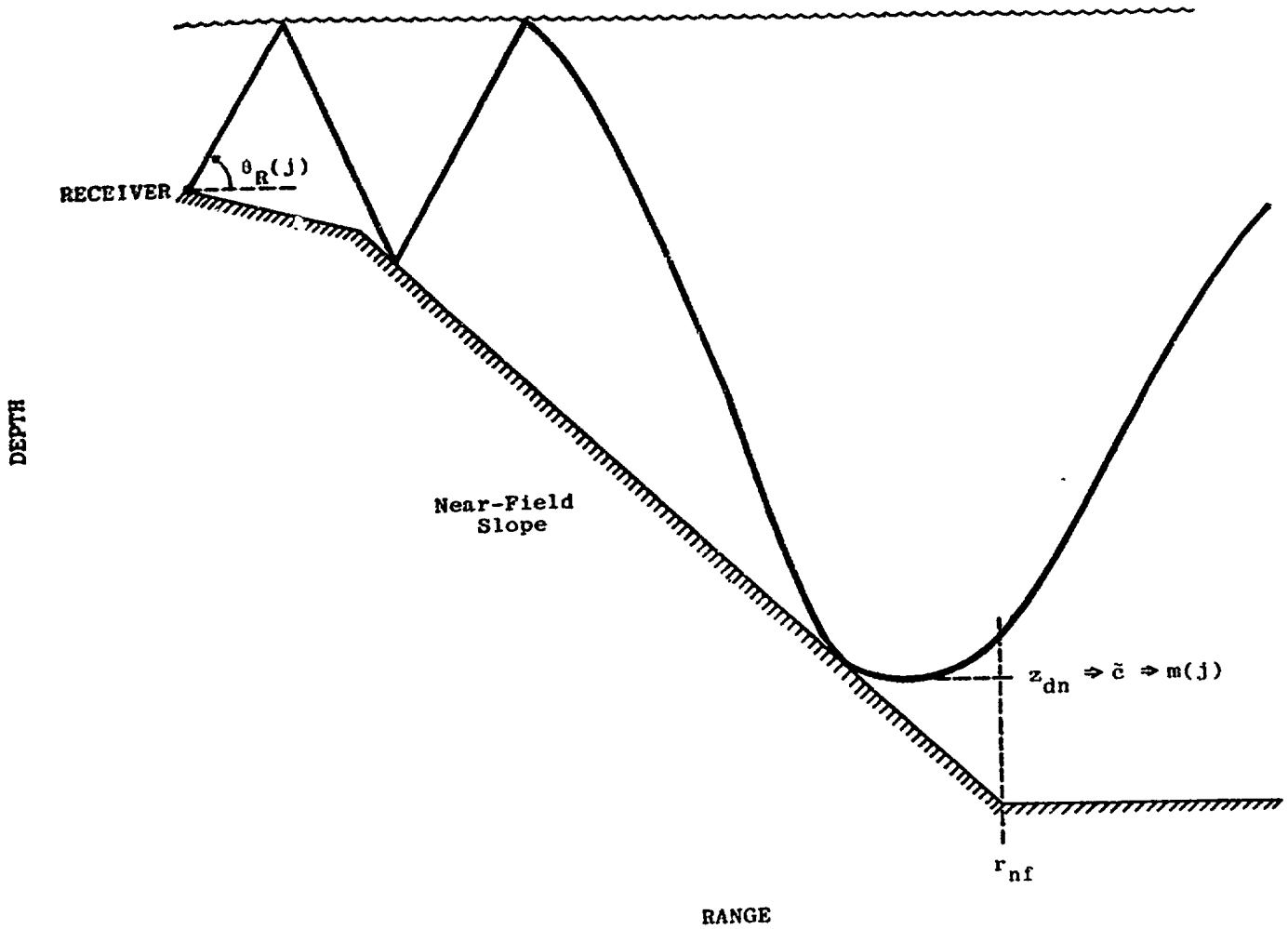

Figure 3-2. Example of Slope Conversion of a Ray - m(j) is New Mode Number

zero (minus for $\theta > 0$). The ray period is obtained by interpolation in $P(\tilde{c})$ where $\tilde{c}$ is the ray's turning-point sound speed.

Initially, since the ray corresponds to a mode, m, $\tilde{c} = c_m$ and $P = P_m$. The ray is then traced with a check for reflection either before or after its upper turning point. An initial reflection is permitted if

$$z_{nf} \geq z \text{ and } \hat{\theta} < \beta,$$

where the near-field bottom has slope β (positive up) and depth z_{nf} at range zero, and $\hat{\theta}$ corresponds to the angle of the ray at $(r=0,\ z=z_R)$ on the circular arc:

$$\hat{\theta} = \sin^{-1}(r_c/\rho).$$

If the ray cannot initially reflect it is incremented by one cycle ($r_c \rightarrow r_c + P$), and in either event a test for reflection is made by solving for the intersection (r',z') of the circle and straight line:

$$r' = r_c + u$$

$$z' = z_{nf} - r' \tan \beta,$$

where

$$u = \cos\beta \left\{ w\sin\beta - \left[\sqrt{\rho^2 - (w\cos\beta)^2} \right] \right\}$$

and

$$w = z_{nf} - r_c \tan\beta - z_c .$$

The ray reflects if $\rho > w\cos\beta$ and has angle θ' at (r',z'):

$$\sin\theta' = u/\rho .$$

The ray grazes the bottom (for purposes of bottom loss) at angle

$$\gamma = \beta - \theta'$$

and reflects specularly at

$$\theta'' = 2\beta - \theta' .$$

The new phase velocity $\tilde{c}$ is computed by finding $c(z')$ from the sound speed profile, and applying Snell's Law

$$\tilde{c} = \frac{c(z')}{\cos\theta''} .$$

The new period and upper and lower turning-point depths are then found by linear interpolation in their values as functions of $\tilde{c}$. The ray is advanced through an upper turning point ($r_c \rightarrow r_c + P$) and the reflection test is repeated until either the ray can no longer reflect, or the end of the near-field bathymetry, r_{nf}, is reached.

If the near field bathymetry has a flat ($\beta = 0$) bottom, the above calculations would be repetitive and the periodicity is used to speed up the process. The value

of $\tilde{c}$ after the last allowed reflection is used to identify the corresponding mode as previously described. As a result of this trace, and after incorporation of immediate-slope effects (elimination of modes, etc.), the original set of 25 modes spaced at axis angles of 1-degree from 1 to 20 degrees and 5-degrees from 25 to 45 degrees may consist of a subset of propagating modes between m_1 and m_2 with some possible interior non-propagating modes. These are recognized and flagged to minimize subsequent computations.

3.2.2 Treatment of the Source

For each water mass, the set of rays described above are traced through one full cycle to compute their periods, phase integrals, turning points, etc. First their turning point sound speeds or phase velocities, $\tilde{c}$, are found from Snell's Law

$$\tilde{c} = c_{axis}/\cos\theta_{axis},$$

where

$$\theta_{axis} = \begin{cases} 1,2,\ldots,20 \\ 25,30,\ldots,45 \end{cases} \text{degrees.}$$

The ray period is given by

$$p^{\infty} = 2 \cdot \sum_k \frac{\tilde{c}}{g_k} (\sin\theta_k^1 - \sin\theta_k^2)$$

where the summation is over all layers in the sound-speed profile which have some portion where $c(z) < \tilde{c}$. θ_k are all positive and the superscripts of 1 and 2 indicate values at the upper and lower ends of the layer, respectively. The ray angles at the endpoints of each layer are:

$$\cos\theta_k = c_k/\tilde{c}.$$

If only a portion of the layer has $c(z) < \tilde{c}$ then the ray turns in that layer and one $\theta_k = 0$. If $g_k = 0$, then the contribution from that layer is

$$\Delta r_k = (z_k^2 - z_k^1)/\tan\theta_k^1.$$

For the phase integral

$$\psi^{\infty} = \sum_k \frac{1}{g_k}\left\{\sin\theta_k^2 - \sin\theta_k^1 - \ln\left[\frac{c_k^1}{1+\sin\theta_k^1} \cdot \frac{1+\sin\theta_k^2}{c_k^2}\right]\right\}.$$

If the ray turns in the layer (and say $\theta_k^2 = 0$) then c_k^2 is replaced by $\tilde{c}$. For zero-gradient layers

$$\Delta\psi_k = (z_k^2 - z_k^1)\sin\theta_k^1/c_k^1.$$

If $\tilde{c} \geq c(z = 0)$ then the upper turning point depth is taken as zero. Otherwise the first depth (z_{up}) in the sound-speed profile where

$$c(z_{up}) = \tilde{c}$$

is the upper turning point, and the last point (z_{dn}) where

$$c(z_{dn}) = \tilde{c}$$

is the lower turning point. For subsequent diffraction calculations the magnitudes of the gradients at these points (g_{up}, g_{dn}) are saved.

The source eigenfunctions are then computed as a function of z_{up}, z_{dn}, g_{up}, g_{dn}, the source depths, ray angle, and frequency. First, the geometric limit, h_g, is computed where

$$h_g = 1/\tan\theta(\tilde{c},\ c(z_s)),$$

θ being the angle at the source depth, z_s, of the ray with phase velocity $\tilde{c}$:

$$\cos\theta = c(z_s)/\tilde{c}\ .$$

If $c(z_s) \geq \tilde{c}$, $h_g = 0$.

For each frequency, f, the upper (if $z_{up} > 0$) and lower turning point scale factors and limits for diffraction corrections are computed

$$\hat{\theta}_{up/dn} = \left(\frac{3g_{up/dn}}{4f}\right)^{1/3}$$

$$\hat{\Delta z}_{up/dn} = \hat{\theta}^2_{up/dn}\left(\tilde{c}/2g_{up/dn}\right)$$

$$\alpha_{up/dn} = 1.77/\hat{\Delta z}_{up/dn}$$

$$\hat{z}_{up/dn} = z_{up/dn} +/- \hat{\Delta z}_{up/dn}$$

$$h_{c,up/dn} = 1/\hat{\theta}_{up/dn}$$

All of the above variables are functions of frequency. $\hat{\theta}$ is the minimum angle permitted before diffraction limits the intensity, h_c is the caustic limit for the intensity, and $\hat{z}$ are the depths at which these limits will apply.

Except for the special cases noted below, beyond $\hat{z}$ (i.e. in the diffraction area):

$$h(z) = h_c \left[\frac{Ai^2(+/- \alpha(z_{up/dn} - z))}{Ai^2(0)} \right]$$

where Ai is the Airy function, and for upper turning points

$$h = \left(\sqrt{h(z)} - \sqrt{h(-z)}\right)^2$$

to include surface image interference of the diffracted field.

There are a number of special cases, however, associated with overlapping turning point regions and interior profile maxima. If the diffraction regions overlap (i.e., if $\hat{z}_{up} > \hat{z}_{dn}$) define an overlap region (z_1, z_2) between $\hat{z}_{up}$ and $\hat{z}_{dn}$ but not beyond the turning points:

$$z_1 = \max(z_{up}, \hat{z}_{dn})$$
$$z_2 = \min(z_{dn}, \hat{z}_{up}).$$

In this region a linear interpolation between $h_{c,up}$ and $h_{c,dn}$ will be used. If a profile has an interior maximum such that h_g gets too large (or 0 - i.e. $c(z) > \tilde{c}$), then in this region use a linear interpolation between $h_{c,up}$ and $h_{c,dn}$. For RSR modes $\hat{z}_{up} = 0$, $h_{c,up} = h_{c,dn}$ and the above procedures carry through.

Finally, once the diffraction-corrected geometric intensity is computed, surface-image interference effects are incorporated for surface-reflected modes by setting

$$\phi^{\infty} = \begin{cases} 2h \cdot \sin^2\psi_0 & \psi_0 < 3\pi/4 \\ h & \psi_0 \geq 3\pi/4 \end{cases},$$

where

$$\psi_0 = \frac{2\pi f \cdot z_s}{c(z = 0)} \sin\theta(z = 0).$$

This limits surface-image effects to the null and first constructive lobe below the surface.

The above treatment of special cases is aimed solely at providing a continuous result. For overlapping turning-point regions, the correct solution corresponds to Parabolic Cylinder Functions rather than Airy Functions and is too complicated to treat. When interior maxima in the profile force $h_g > h_c$ the eigenfunctions are much more complicated. Typically they split into groups concentrated in the upper or lower channel (but not both), or in the case of symmetric channels into pairs of modes which, depending on their phasing, concentrate in one or the other channel.

The treatment here is clearly approximate and amounts to partitioning the energy between both channels and allowing energy between the interior turning points. It is consistent with the rest of the treatment of double channels (e.g., cycle distances and phase integrals) but is clearly an area where improvement is possible.

These values for ϕ^{∞} are computed assuming an infinitely deep ocean bounded by a pressure gradient. Hence the lower turning point always exists. When a given region of finite depth (z_e) is considered the normalization is computed

$$\phi = \phi^{\infty}/(1/2\ P_m(z_e)),$$

where

$$P_m(z_e) = \begin{cases} P_m^{\infty} & z_e \geq z_{dn} \\ P_m^{\infty} - \frac{2\tilde{c}}{g_p} \sin\theta_b \cdot \alpha & z_e < z_{dn}. \end{cases}$$

θ_b is the bottom grazing angle at z_e by Snell's Law and g_p is the pressure gradient (0.018 sec^{-1}). The factor α is chosen to continuously model the departure of the ray trajectory from the pressure-gradient assumption. Specifically

$$\alpha = 1 - \frac{(\Delta P(z_{up}) - P_m^{\infty})}{\Delta P(z_{up})} \left[\frac{z_{dn} - z_e}{z_{dn} - z_{up}}\right]^2 ,$$

where $\Delta P(z_{up})$ is the distance the ray with turning point z_{dn} would spend in a pressure gradient below the depth z_{up}.

$$\Delta P(z_{up}) = \frac{2\tilde{c}}{g_p} \sin\theta_{up} ,$$

where

$$\cos\theta_{up} = \frac{c_o(=4776 \text{ ft/sec}) + g_p \cdot z_{up}}{\tilde{c}} .$$

Note that if the actual profile is the pressure-gradient profile $\Delta P(z_{up}) = P_m^{\infty}$ and $\alpha = 1$ (i.e. no correction). Also the correction goes quadratically to zero as $z_e \rightarrow z_{dn}$. At the upper turning point $\theta_b = \theta_{up}$ and $p_m(z_e) = 0$.

If $z_e \leq z_{up}$ (i.e., the water is so shallow that none of the mode is allowed to propagate), the mode is not considered. Note that since the corresponding phase integral will be zero no mode could couple to it anyway. (This is an example of the difference between this treatment and a standard treatment where m is the mode index, or eigenvalue in each region. Here m merely refers to a phase velocity which may or may not correspond to a propagating mode.)

The phase integral is similarly modified for finite depth:

$$\psi_m(z_e) = \begin{cases} \psi_m^{\infty} & z_e \geq z_{dn} \\ \psi_m^{\infty} \left(1 - \Delta\psi(z_e)/\Delta\psi(z_{up})\right) & z_e < z_{dn}, \end{cases}$$

where $\Delta\psi$ is the decrement to the phase integral (assuming an infinite pressure gradient) and water depth z:

$$\Delta\psi(z) = -\sin\theta(z) - \ln\left[\frac{c(z)}{\bar{c}(1 + \sin\theta(z))}\right].$$

This treatment forces the phase integral to zero at the upper turning point. Again if the medium is pressure gradient the formula makes no approximations.

For this region, the bottom loss per unit distance is computed for $z_e < z_{dn}$ by

$$\alpha_B(f) = BL(\theta_b, f, BC)/P_m \quad \text{(dB per nm)}.$$

This loss rate is added to the surface and volume losses to compute the total α.

3.2.3 Range Dependence

The key issue in range dependence is the adiabatic mapping of modes. From the initial excitation and subsequent attenuation, a certain set of modes $\{\hat{\phi}_m\}$ have been identified as propagating at a given range. These have phase integrals ψ_m^0 after initial excitation. In the new environmental region the modes have phase integrals $\psi_m(r)$, and it is necessary to identify that mode in the new region which will carry the energy of the original modes, i.e., $m'(m,r)$. The mapping is done such that

$$\psi_{m'-1}(r) < \psi_m^0 \leq \psi_{m'}(r).$$

The finite discretization of the modes makes this mapping approximate and several modes may appear to map into one

under certain circumstances. (For example, modes corresponding to axis angles of 16 through 19 degrees may all map into the high-angle mode from 20 to 25 degrees. If the modes convert to shallower angles they may be separated in subsequent mappings.)

When the water becomes very shallow, deep-water modes are converted to very steep modes. Since the basic mode set only goes to axis angles of 45 degrees, any steeper modes are assigned to this last mode and propagate accordingly. Since this high angle will attenuate rapidly the approximation is probably adequate and preferable to the overhead of carrying higher angle modes.

When only the water depth changes (and not the water mass or sound-speed profile), the new mapping need only be applied to modes which were before, and/or now become bottom-reflected. To minimize unnecessary computations a check is made to decide whether the depth change is significant.

The change is not significant if (1) below holds or both (2) and (3) hold:

(1) The highest angle ($m = m_2$) propagating mode was not and does not become bottom reflected. Specifically,

$m_2 < m_b$ (the first bottom-reflected mode in previous depth)

$z_{dn}(m_2) \leq z_e$ (in new region).

(2) The first bottom-reflected mode stays bottom-reflected, and the last non-bottom-reflected mode stays non-bottom-reflected. Specifically,

both $z_{dn}(m_b) > z_e$

and $z_{dn}(m_b-1) \leq z_e$.

(3) The change is small enough that no mode changes phase integral. This will be most likely to occur where the modes are steepest and most densely packed (i.e., near the 20-degree mode if present). This test is approximately made by assuming a homogeneous medium:

$$\psi(\theta, z_e) = \frac{1}{c_0} \sin\theta \cdot z_e$$

so that between modes for fixed depth

$$\delta\psi_\theta = \frac{1}{c_0} z_e \cos\theta \; \delta\theta .$$

Whereas for a depth change δz_e, at fixed angle

$$\delta\psi_z = \frac{1}{c_0} \sin\theta \; \delta z_e .$$

Hence if δz_e is sufficient to change ψ by $\delta\psi_\theta$, the mode will change number. That is, the change is not significant if $\delta z_e \leq \hat{\delta z}_e$ where

$$\hat{\delta z}_e = \frac{z_e \delta\theta}{\tan\theta} .$$

This test is applied to the steepest bottom reflected mode unless the 20-degree mode is present and bottom-reflected in which case it is used. Since generally the 20-degree mode will be bottom-reflected this test can be used as a convenient pre-filter of bathymetry, eliminating fractional changes in water depth

$$\frac{\Delta z}{z} \leq \frac{\delta\theta(=1^{o})}{\tan(20^{o})} \simeq \frac{0.017}{0.36} \simeq 5\%.$$

3.2.4 The Smoothing Algorithm

The smoothing algorithm operates on each transmission-loss curve (one for each source-depth/frequency combination) separately. Hence consider the range, transmission-loss pairs (R(k), TL(k), k = 1,n). The algorithm first flags all points of "significant" discontinuity, $\hat{k}$, defined as follows:

$$(1) \quad |TL(\hat{k}) - TL(\hat{k} + 1)| > \Delta TL \ (=2 \text{ dB})$$

and

$$(2) \quad |\widetilde{TL} - TL(\hat{k} + 1)| > \Delta TL ,$$

where $\widetilde{TL}$ is extrapolated from $\hat{k}$ and $\hat{k} - 1$ to $\hat{k} + 1$:

$$\widetilde{TL} = TL(\hat{k}) + \alpha(\hat{k})[R(\hat{k}+1) - R(\hat{k})],$$

$$\alpha(\hat{k}) = \frac{TL(\hat{k}) - TL(\hat{k}-1)}{R(\hat{k}) - R(\hat{k}-1)} .$$

These points are flagged by working out in range (beginning with the second point). Once a point is flagged the check continues at $\hat{k} + 2$ (i.e., the suspicious point is not used for a slope computation).

Once all points $\{\hat{k}\}$ have been identified as suspicious, they are examined for possible source. First a check is made to see if they correspond to the end of an environmental region (r_e):

$$|R(\hat{k}) - r_e(i)| \overset{?}{<} \varepsilon_r (= 0.1 \text{ nm}).$$

If this tolerance is not met the point is not changed. If the point does correspond to the end of an environmental region, it is next checked for the end of a water mass (i.e., index (i) $\overset{?}{\neq}$ index (i-1)). If this is the case, first $TL(\hat{k})$ is linearly interpolated in range between $\hat{k} - 1$, $\hat{k} + 1$. Then all transmission loss points between $R(k_1)$ and $R(\hat{k})$ and between $R(\hat{k})$ and $R(k_2)$ will be linearly interpolated in range. These endpoints $R(k_1)$ and $R(k_2)$ are no farther away from $R(\hat{k})$ than the minimum of: (a) halfway to the next $R(\hat{k})$; (b) halfway to the far side of the water mass (i.e., $r_e(i \pm 1)$); or (c) 150 nm.

If the discontinuity is not associated with a water-mass change a water-depth change is considered:

$$\left| \frac{z_e(i) - z_e(i-1)}{z_e(i-1)} \right| \overset{?}{>} \varepsilon_z (= 1\%) .$$

If there has been a depth change, $TL(\hat{k})$ is linearly interpolated in range between $\hat{k} - 1$ and $\hat{k} + 1$, otherwise no change is made.

This procedure is repeated for all flagged points at all frequencies and source depths. On option the smoothing procedure can be suppressed or both unsmoothed and smoothed output can be obtained.

Section 4
Model Evaluation

This section contains a preliminary evaluation of the transmission-loss model in terms of comparisons with parabolic-equation (PE) results for precisely the same environmental inputs. The objective of these comparisons has been to quantitatively assess the basic model accuracy in the absence of errors associated with imperfect inputs. That is, let prediction error, ε_p, be defined as the difference between actual (TL) and predicted ($\widehat{TL}$) transmission loss under the actual ({ENV}) and predicted ($\{\widehat{ENV}\}$) environments:

$$\begin{aligned}
\varepsilon_p &= TL(\{ENV\}) - \widehat{TL}(\{\widehat{ENV}\}) \\
&= TL(\{ENV\}) - TL(\{\widehat{ENV}\}) \\
&\quad + TL(\{\widehat{ENV}\}) - \widehat{TL}(\{\widehat{ENV}\}) \\
&= \varepsilon_{ENV} + \varepsilon_{MOD},
\end{aligned}$$

where ε_{ENV} is the variability in propagation loss under the actual and predicted environments, and ε_{MOD} is the model error assuming perfect inputs. Letting $\widetilde{TL}$ correspond to transmission loss predicted by PE, then ε_{MOD} may be rewritten as:

$$\varepsilon_{MOD} = TL(\{\widehat{ENV}\}) - \widehat{TL}(\{\widehat{ENV}\})$$

$$= TL(\{\widehat{ENV}\}) - \widetilde{TL}(\{\widehat{ENV}\})$$

$$+ \widetilde{TL}(\{\widehat{ENV}\}) - \widehat{TL}(\{\widehat{ENV}\})$$

$$= \varepsilon_{MOD,PE} + \tilde{\varepsilon}_{MOD},$$

the first term being the PE model error and the second the difference between PE and the ASTRAL model.

In several comparisons with both exact (normal-mode) solutions and measured data, PE has been found to have a basic model error (when smoothed much less than the present model) of zero mean and less than 1-dB standard deviation. The variance in the model error could not be separated from the measurement uncertainties, and may in fact be somewhat less. It will be assumed here that

$$\varepsilon_{MOD} = \tilde{\varepsilon}_{MOD},$$

and $\tilde{\varepsilon}_{MOD}$ will be evaluated. When it reduces to variances comparable to 1 dB^2 it may, in fact, be less.

The evaluation cases consist of five basic water-mass evolutions in conjunction with four different bathymetry sections. While all combinations were not considered a total of 12 different environments were treated. In each environment one or two receiver depths were used and propagation-loss was computed at three source depths (60, 300, and 1000 feet) and three frequencies (64, 128, and 256 Hz) in each of the 20 model runs. (For PE each frequency required a separate run.)

The five water mass evolutions have been designated 1 through 5 and the four bathymetry sections A through D. A final designator of 1 or 2 will be used for the first or second receiver. (Their specific depths vary from case to case.)

In the five sound-speed sections a total of eight different sound-speed profiles were considered, varying from a simple half-channel profile to a double channel with a surface duct. The range dependence in some examples is probably unrealistically severe. The bathymetry sections were selected to highlight certain profile/bathymetry coupling effects which are dramatized by using a very high-loss bottom. These combinations may also be unrealistically severe. They were picked to exhaustively test the model's algorithms and assumptions by highlighting selected paths.

In the illustration of an environment (e.g., the bottom of Figure 4-1),* the actual profiles used in the model are shown as solid curves. These were applied between the ranges of the 10000' point on the dashed profiles (the center point of the arrow). In this example the first profile was used from 0 to 350 nm, the second from 350 to 650 nm, etc. In running PE a continuous evolution for the sound-speed profile is required. The dashed profile indicates the intermediate profile at the midpoint of the transition regime designated by the arrows (e.g., a continuous evolution from profile 1 to profile 2 between 300 and 400 nm).

The adiabatic treatment of the range-dependent environment implicitly assumes that the details of the evolution are not essential to the level once the evolution is complete.

---

*See page 4-11.

The smoothing algorithm attempts to eliminate discontinuities by identifying their likely source (and its extent) and smoothing the levels through the transition region. Agreement between the model and PE in the transition region will thus be largely fortuitous. Agreement at the end of a transition region is a true measure of model accuracy.

The adiabatic approximation will break down if the PE results are sensitive to the rate at which the transition occurs or its position in range (i.e., the thickness and placement of the transition region). The adiabatic approximation cannot predict such a sensitivity and may, at best, represent an average result. It is also possible that the adiabatic result is totally outside the possible range of results for rapid transitions, since it assumes a gradual evolution.

When a range-dependent bottom profile is used (e.g., Figure 4-7)* the staircase profile assumed by the model is plotted as a solid curve and the PE continuous equivalent is plotted as a dashed line. The model used a loss per bounce of 40 dB at all angles and frequencies. PE used a "high-loss" bottom model which through an artifically large volume attenuation eliminates all paths which reach the bottom.

The test cases are summarized below in the following subsections. For each specific case (environment, bathymetry and receiver (located at range zero)), the results are presented on a single page for each source depth at a fixed frequency (e.g., Figure 4-1 corresponds to case 1A1 for a 64-Hz source at depths 60, 300 and 1000 ft). The solid transmission-loss curve is the range-smoothed PE and the squares are the discrete model predictions. The receiver

---

*See page 4-17.

location (2500 ft in this case) is indicated by the "R" at the appropriate depth. Higher frequencies follow and all figures for a Test Case follow the discussion of the case.

The principal objective of the case-by-case discussion is to identify model weaknesses and determine, wherever possible, the basic cause. Virtually all of the major discrepancies have been traced back to known model limitations. Nearly all could be remedied in the basic context of the present model. In the course of these comparisons a number of deficiencies were corrected as they were found. Those remaining would require a substantial effort to remedy and, at present, do not appear to represent sufficiently severe limitations to warrant delaying program release. These limitations and the environments and geometries most likely to emphasize them are summarized in Section 4.6.

Subsection 4.7 addresses model accuracy from a statistical viewpoint, summarizing the differences for various source depths, frequencies and values of transmission loss. The final subsection (4.8) summarizes the model evaluation and compares computer running times and approximate costs.

4.1 TEST CASE 1

Test Case 1 consists of a somewhat compressed evolution of the sound-speed profile characteristic of tracks from warmer mid-latitudes to colder northern latitudes (Figure 4-1). Propagation loss from sources in the northern latitudes is a complex function of source and receiver depths and frequency.

4.1.1 Case 1A Flat Bottom

This case addresses propagation loss for a deep (18000 ft) flat bottom with receivers at depths of 2500 and 10000 ft.

4.1.1.1 Case 1A1 - 2500 ft Receiver

64 Hz Comparisons (Figure 4-1). The principal discrepancy occurs in the first transition region (300-400 nm) where the smoother has spread the change over ±150 miles. If the smoother used ±50 miles the results would be much closer. A phenomenon illustrated by this case is the much better coupling between the receiver and the shallow source as the axis rises. The poor coupling in the first 200 miles is magnified by strong surface-image interference losses at 64 Hz which are less severe at the higher frequencies (Figures 4-2 and 4-3).

128 Hz Comparisons (Figure 4-2). The less-severe surface-image interference reduces the magnitude of the decrease in loss in the second region for the shallow source.

A shorter smoothing interval would eliminate most of the discrepancies around 400 miles. The 2-dB mean difference at 300 ft may be due to either the approximate extension in depth of the diffraction fields of key modes, or more likely the termination of surface-image interference effects below the second rms interference point.

256 Hz Comparisons (Figure 4-3). The discrepancies in the first 200 miles at both 60 and 300 ft are probably due to the termination of surface-image interference effects. The error at 60 ft magnifies the problems associated with the smoother between 250 and 400 miles.

4.1.1.2 Case 1A2 - 10000 ft Receiver

64, 128 and 256 Hz Comparisons (Figures 4-4, 5, and 6). The transition problem persists at 60 ft and a short-term focusing effect is predicted by PE at 300 ft and 350 miles. The dissipation of the effect by 400 miles indicates that it is strictly a transient phenomenon of the sound-speed evolution. It does indicate that even the range-smoothed level in a transition region is not bounded by the levels on either side.

A more serious problem occurs for the shallow source in the last profile and persists somewhat across frequency. The paths leaving the 10000-ft receiver will be surface reflected in the last profile at angles between approximately 12 and 20 degrees. At 64 Hz and 60 ft these should all experience some degree of constructive interference. While the model appears to indicate this, PE does not. The

discrepancies at 128 Hz and 256 Hz could be removed by extending the surface-image interference below the second rms point. The 64-Hz problem remains unsolved, however, and may indicate a partial breakdown of the adiabatic mapping.

4.1.2 Test Case 1B - Shoaling Bottom

The rising sound-channel axis has been accompanied by a slightly out of phase, shoaling bathymetry to illustrate the losses and recoveries such an environment might produce.

4.1.2.1 Test Case 1B1 - 2500 ft Receiver

64 Hz Comparisons (Figure 4-7). All of the energy reaching 60 ft from 100 to 200 miles is via extended diffraction fields of modes with deeper turning points. As the bottom shoals between 200 and 300 nm the level is controlled by more axial modes and is being somewhat underestimated at both 60 and 300 ft. The recovery in level at 60 ft is more abrupt than in PE because the transmission-loss changes are too rapid for the smoothing algorithm to treat effectively. In the transition and pressure-gradient regions beyond 600 miles the discrepancies at 300 and 1000 ft result from the discrete, small number of modes left in the problem, and the breakdown of the local plane-wave treatment of surface-image interference for low-order modes in a pressure-gradient or "half-channel" environment. The modes are, in fact, strongly focused in this region whereas the surface-image interference estimate has large errors.

128 and 256 Hz Comparisons (Figures 4-8 and 4-9). The same basic problems persist, however, the long-range discrepancies are not so severe at the higher frequencies.

4.1.2.2 Test Case 1B2 - 10000 ft Receiver

64, 128 and 256 Hz Comparisons (Figures 4-10, 4-11, and 4-12). Since the near axial modes do not reach the 10000-ft receiver, the second shoaling eliminates all available modes and the loss increases irrecoverably.

4.1.3 Test Cases 1D1 and 1D2 - Broad Ridge, 2500 and 10000-ft Receivers

64, 128 and 256 Hz Comparisons (Figures 4-13 through 4-18). In this case a broad shallow (7500 ft) ridge is introduced with the second profile. (The increase in depth beyond 700 nm is irrelevant for this environment since the sound-channel continues to rise.) The model handles this environment quite well. A minor problem uncovered in these test cases is the high-loss window from 300 to 350 nm for the shallow sources where the bathymetry intrudes before the sound-speed profile changes. The PE transition region was able to channel energy away from the rising bottom rapidly enough to avoid high losses.

Propagation to the shallow sources at the higher frequencies in the first profile shows the same problem discussed earlier (Case 1B). The overestimated loss at 300 ft for both 128 and 256 Hz may indicate a problem with the extended (and surface reflected) shadow-zone fields. The present treatment assumes that the gradient at the mode turning

point extends indefinitely (to and effectively through the surface for the surface-reflected component). Since the gradient weakens the reflected diffraction field may be stronger than predicted. The assumed phase difference of 180° independent of depth is only an approximation which may degrade with depth.

The energy to the deep receiver from sources beyond the ridge is totally blocked. The model overestimates slightly the range at which the loss increases rapidly, however, the rate of increase is about right.

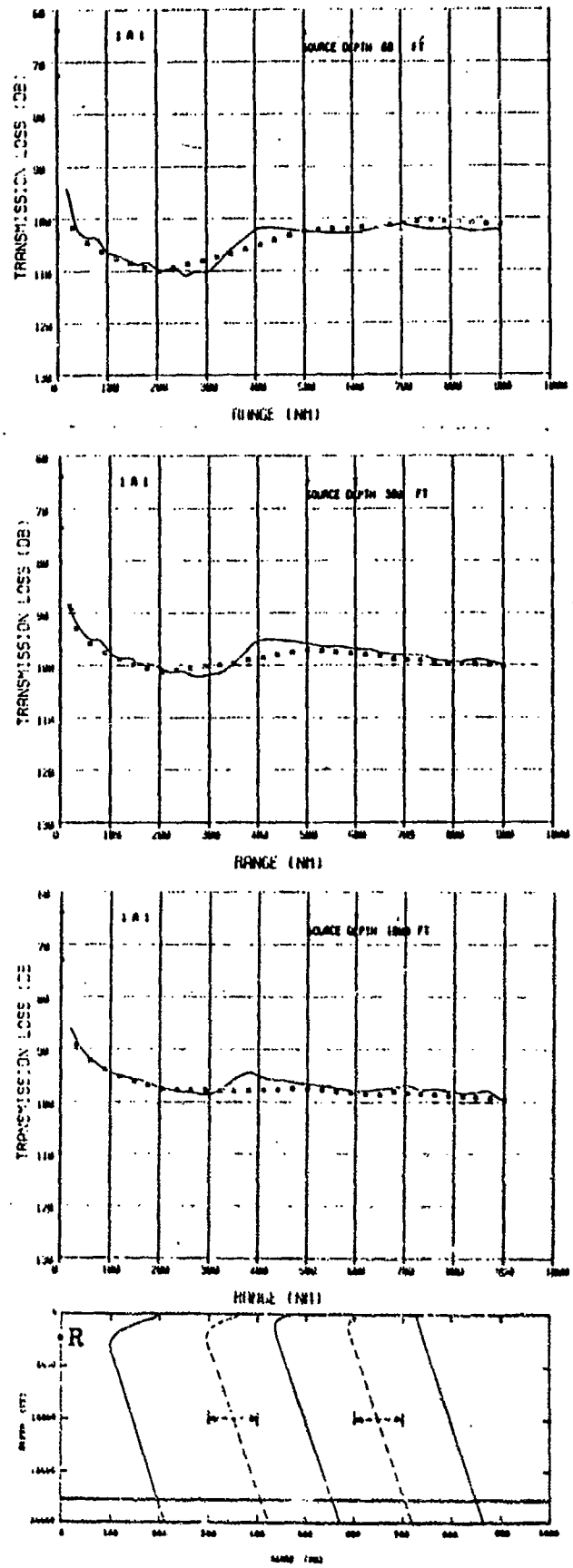

Figure 4-1 Comparison of Range-Smoothed Propagation Loss Versus Range for Test Case 1A1 (2500-ft Receiver-R) for Frequency of 64 Hz. Model(■), PE(—).

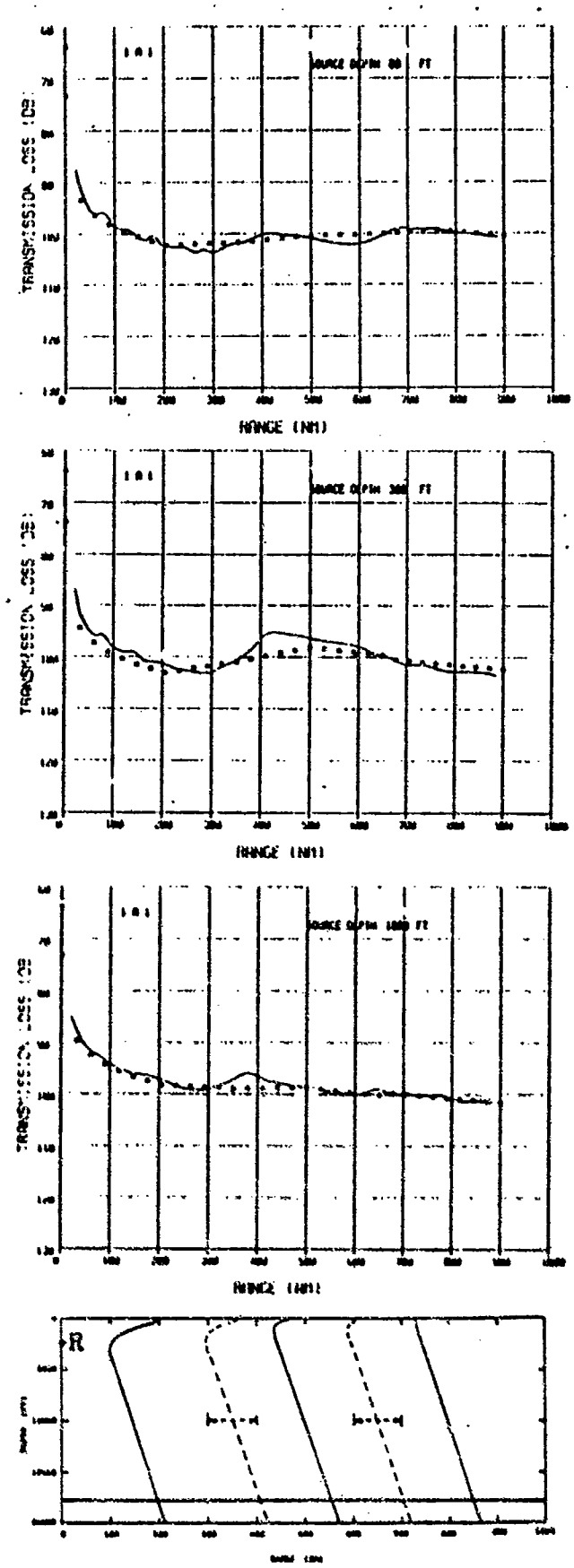

Figure 4-2 Comparison of Range-Smoothed Propagation Loss Versus Range for Test Case 1A1 (2500-ft Receiver-R) for Frequency of 128 Hz. Model(■), PE(—).

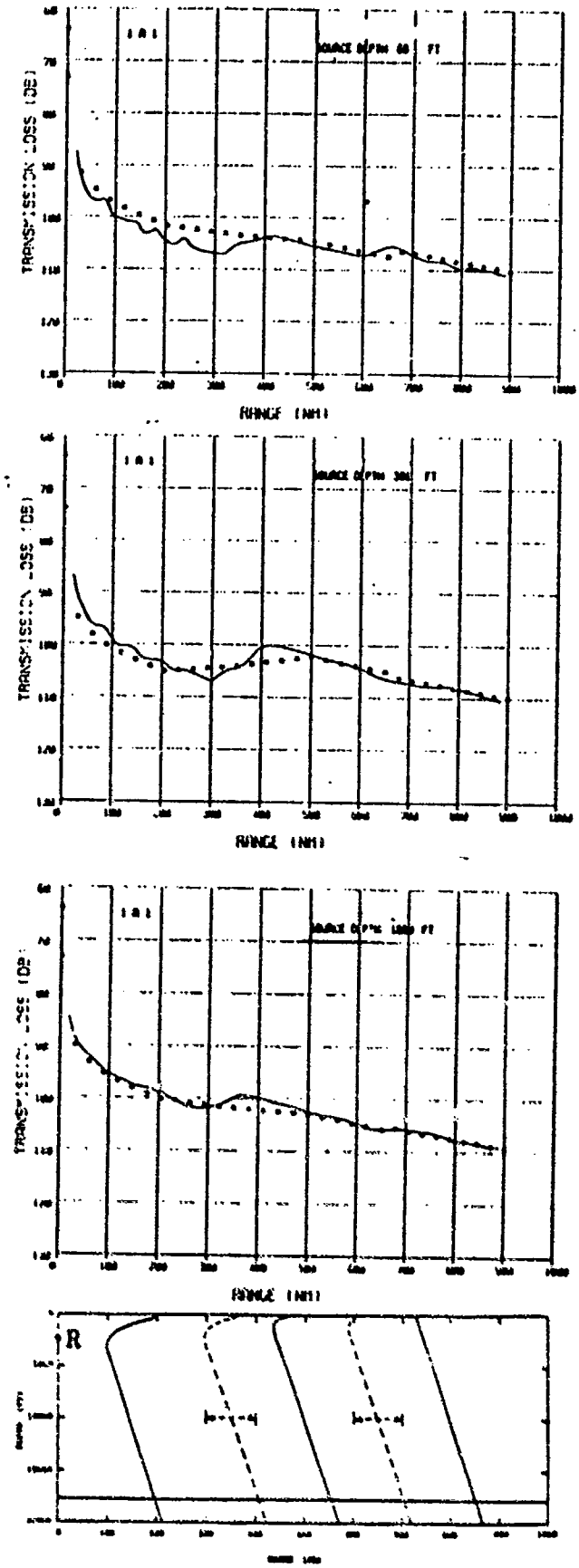

Figure 4-3 Comparison of Range-Smoothed Propagation Loss Versus Range for Test Case 1A1 (2500-ft Receiver-R) for Frequency of 256 Hz. Model(■), PE(—).

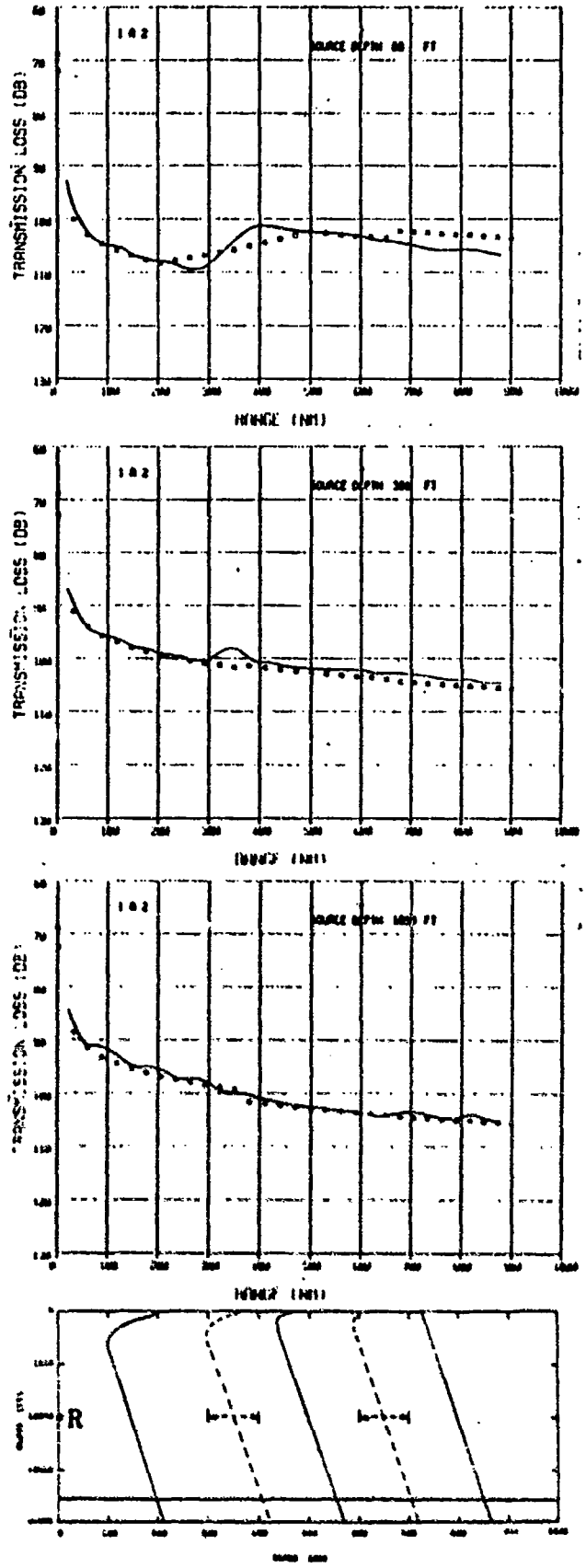

Figure 4-4 Comparison of Range-Smoothed Propagation Loss Versus Range for Test Case 1A2 (10000-ft Receiver-R) for Frequency of 64 Hz. Model(■), PE(—).

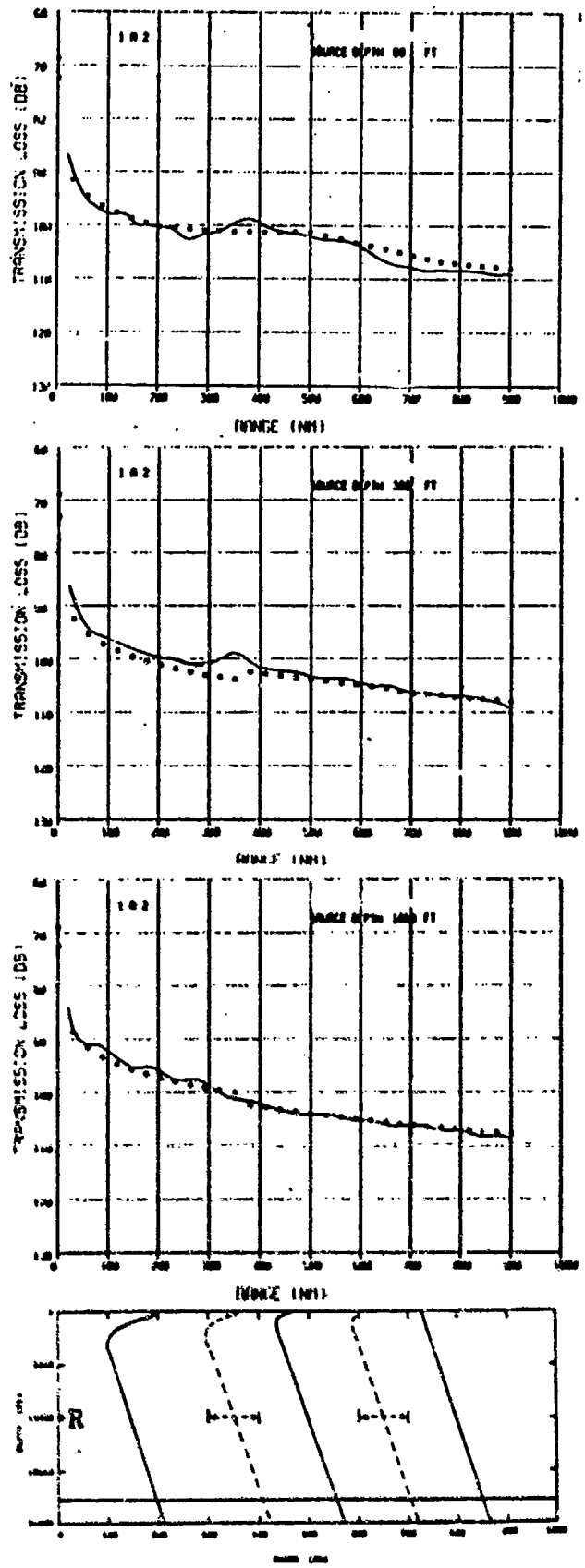

Figure 4-5 Comparison of Range-Smoothed Propagation Loss Versus Range for Test Case 1A2 (10000-ft Receiver-R) for Frequency of 128 Hz. Model(■), PE(—).

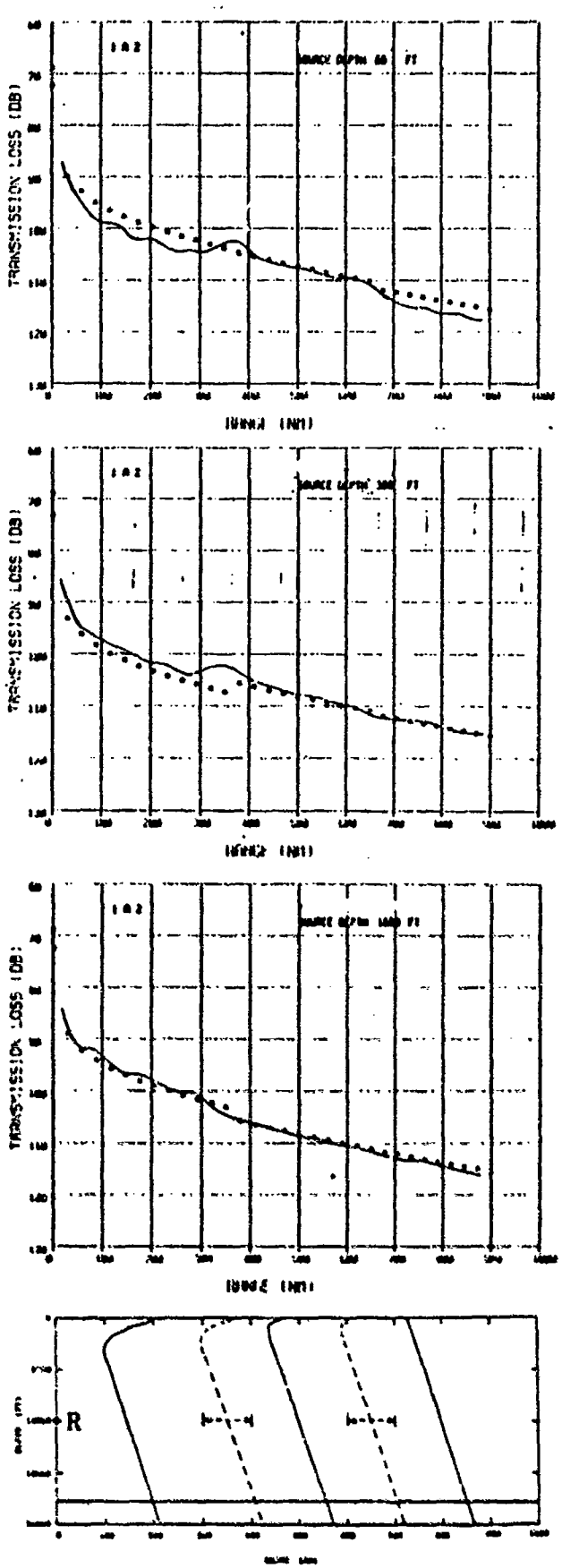

Figure 4-6 Comparison of Range-Smoothed Propagation Loss Versus Range for Test Case 1A2 (10000-ft Receiver-R) for Frequency of 256 Hz. Model(■), PE(—).

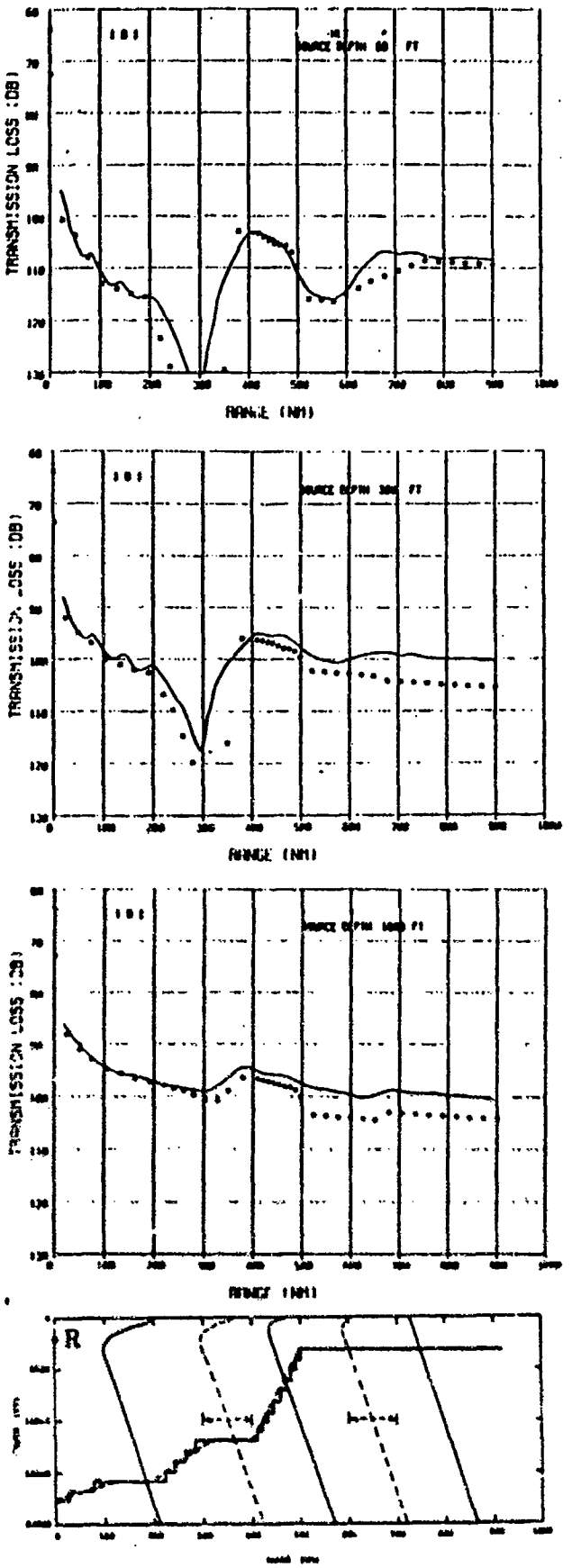

Figure 4-7 Comparison of Range-Smoothed Propagation Loss Versus Range for Test Case 1B1 (2500-ft Receiver-R) for Frequency of 64 Hz. Model(■), PE(—).

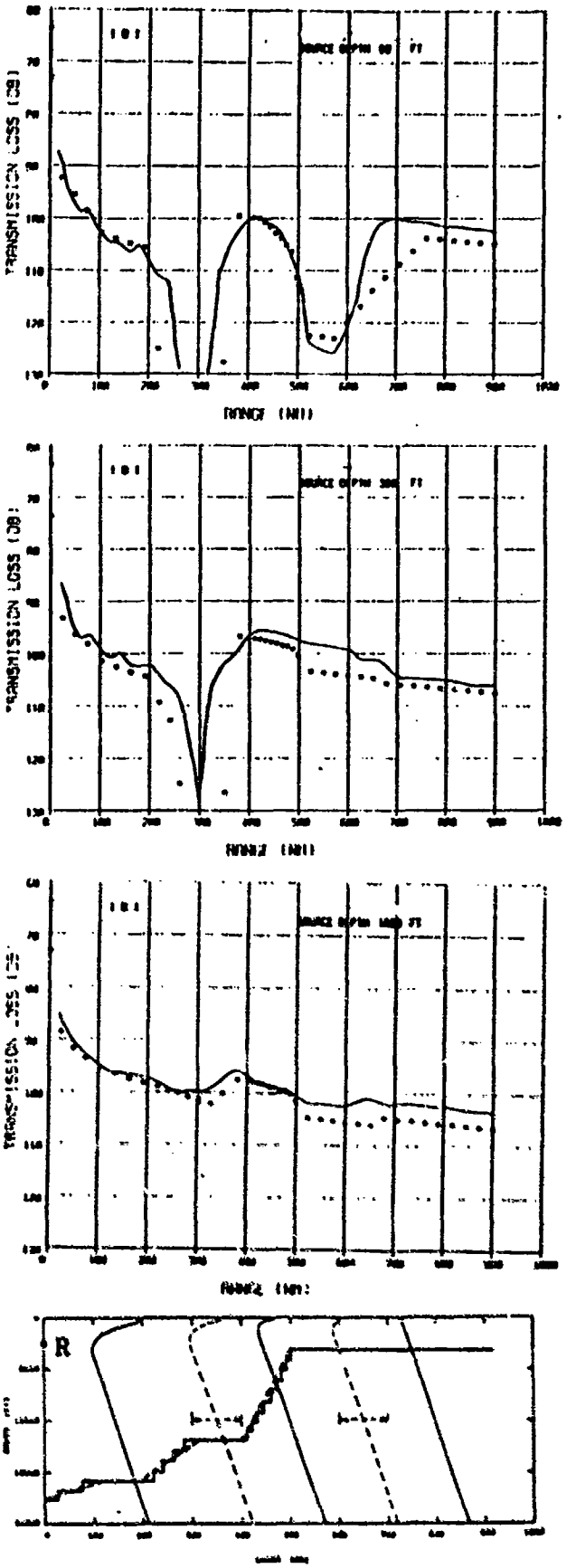

Figure 4-8 Comparison of Range-Smoothed Propagation Loss Versus Range for Test Case 1B1 (2500-ft Receiver-R) for Frequency of 128 Hz. Model (■), PE(—).

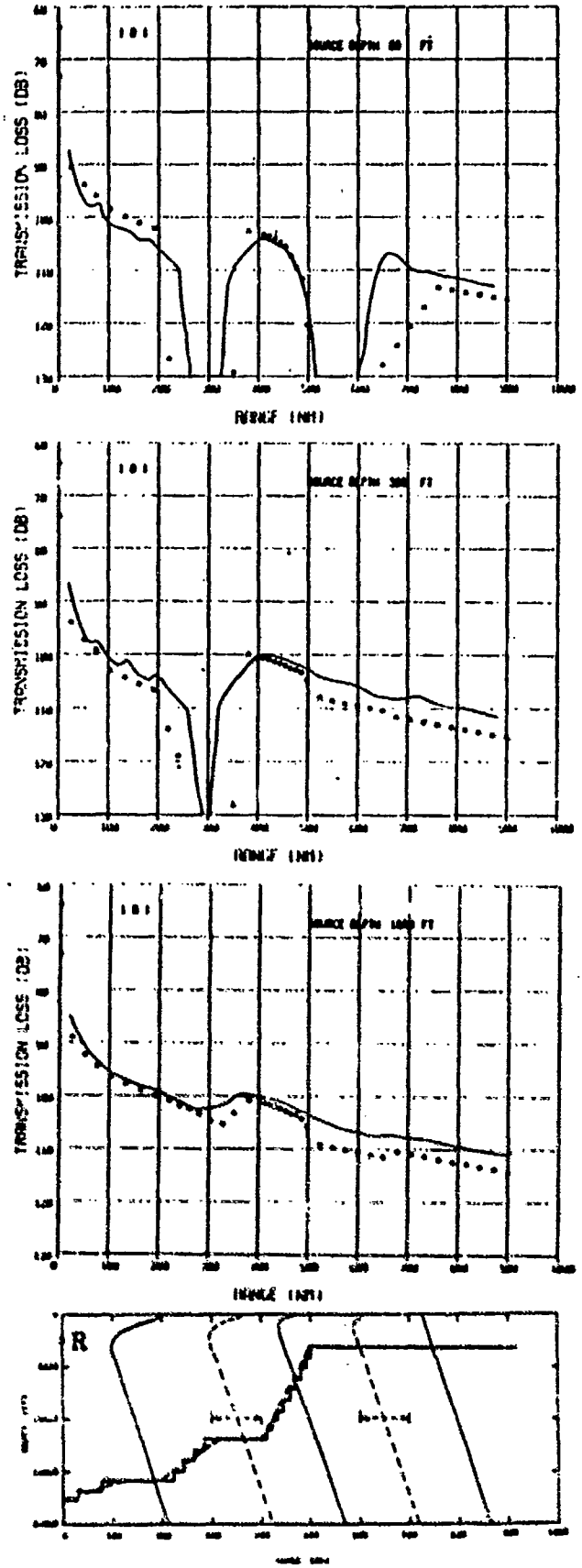

Figure 4-9 Comparison of Range-Smoothed Propagation Loss Versus Range for Test Case 1B1 (2500-ft Receiver-R) for Frequency of 256 Hz. Model(■), PE(—).

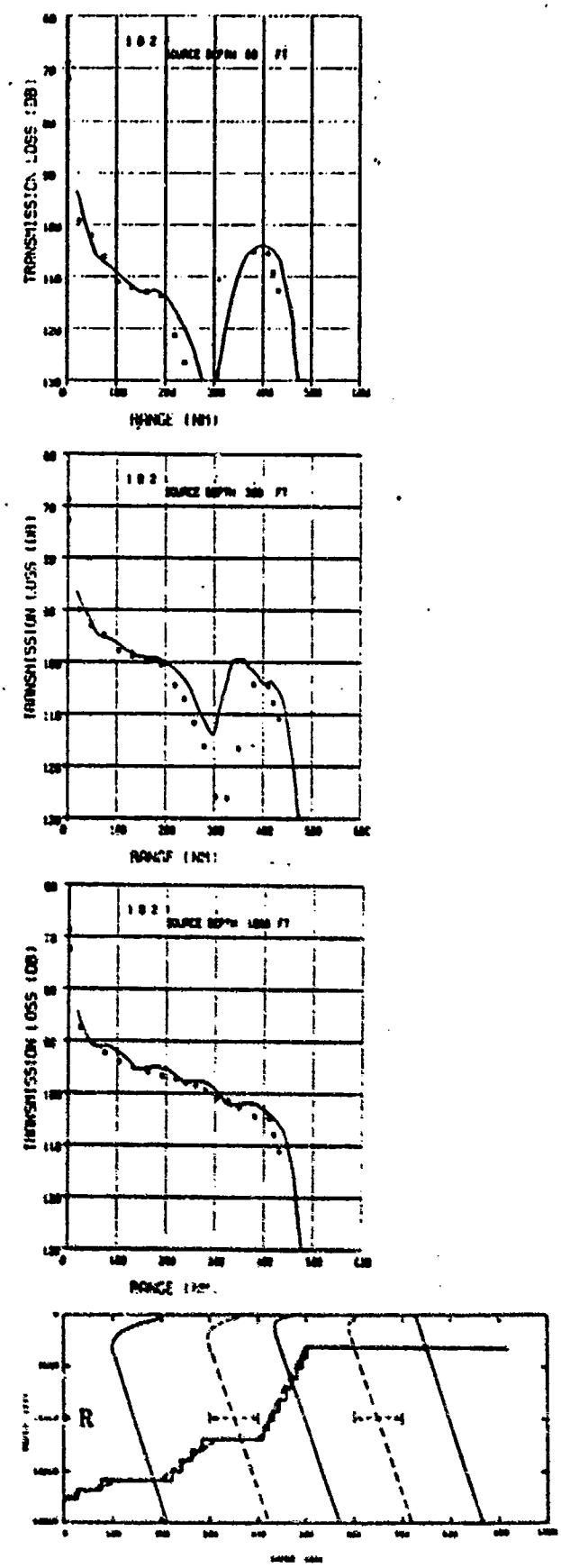

Figure 4-10 Comparison of Range-Smoothed Propagation-Loss Versus Range for Test Case 1B2 (10000-ft Receiver-R) for Frequency of 64 Hz. Model(■), PE(—).

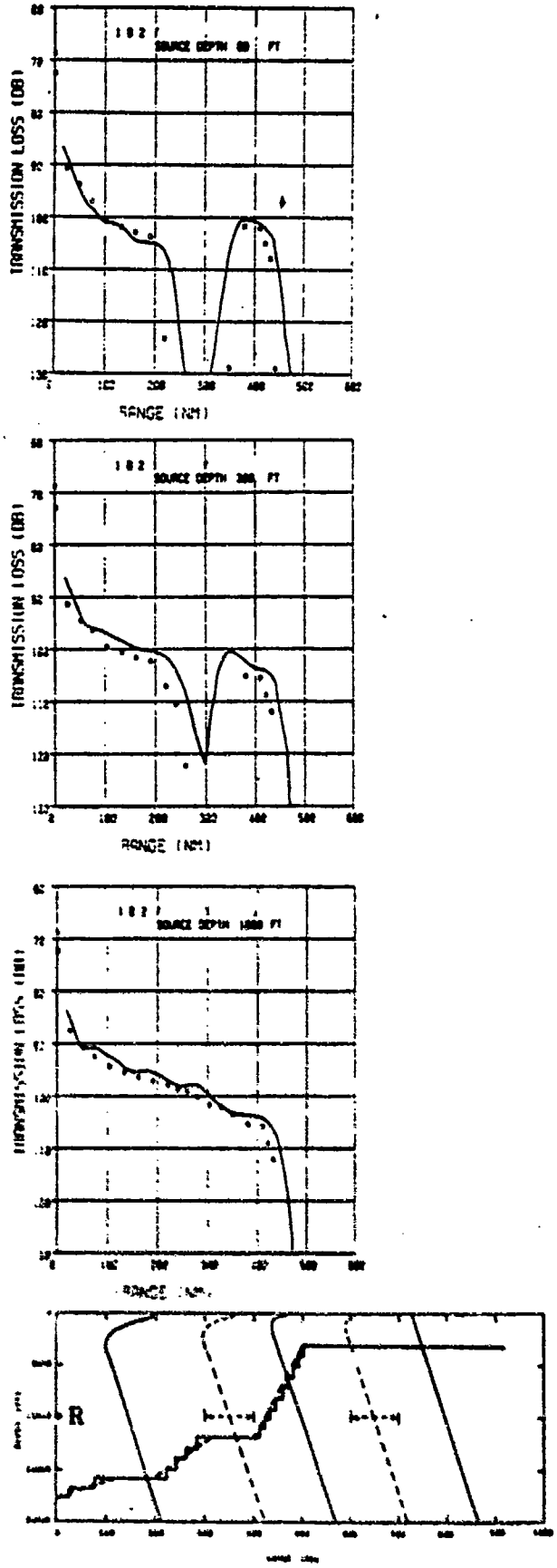

Figure 4-11 Comparison of Range-Smoothed Propagation Loss Versus Range for Test Case 1B2 (10000-ft Receiver-R) for Frequency of 128 Hz. Model(■), PE(—).

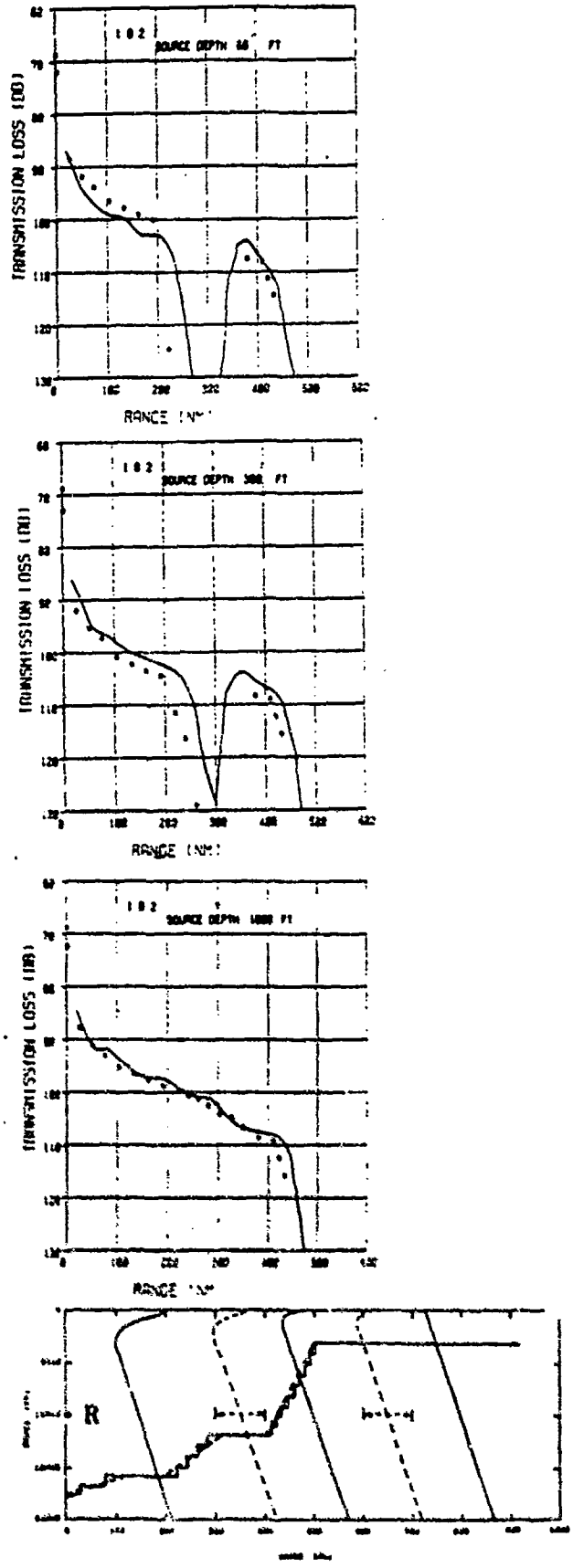

Figure 4-12 Comparison of Range-Smoothed Propagation Loss Versus Range for Test Case 1B2 (10000-ft Receiver R) for Frequency of 256 Hz. Model(■), PE(—).

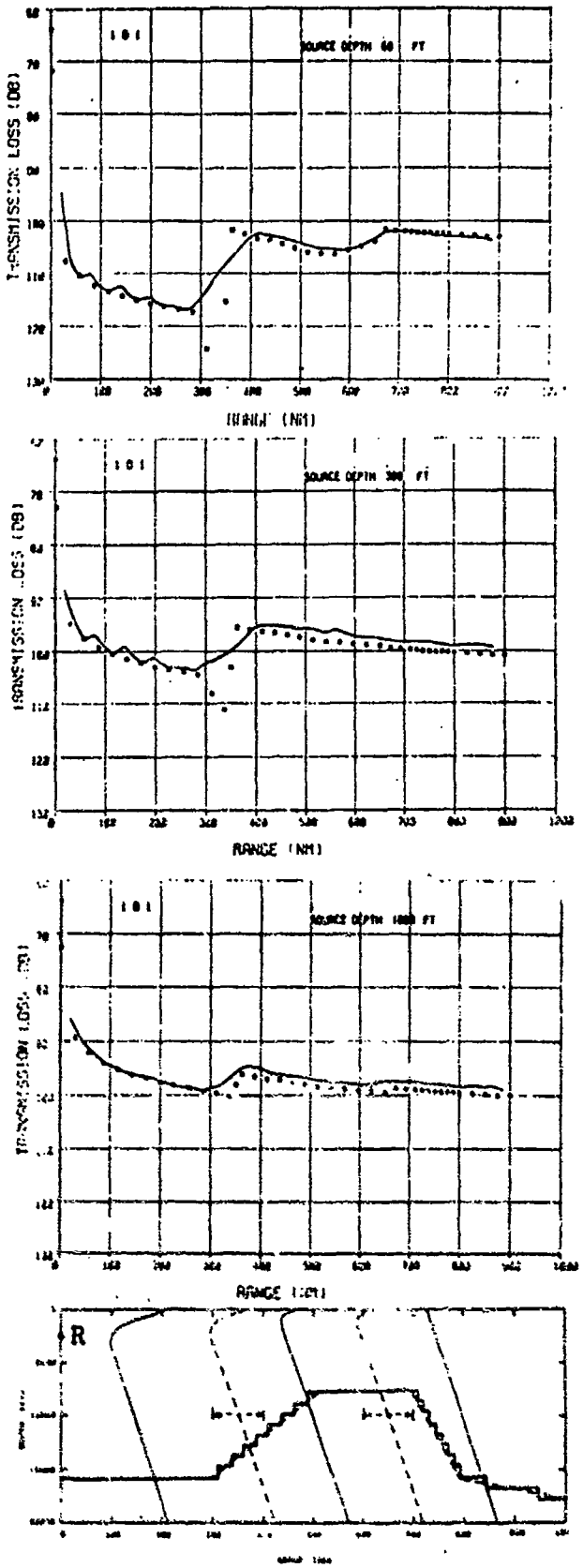

Figure 4-13 Comparison of Range-Smoothed Propagation Loss Versus Range for Test Case 1D1 (2500-ft Receiver-R) for Frequency of 64 Hz. Model (■), PE(—).

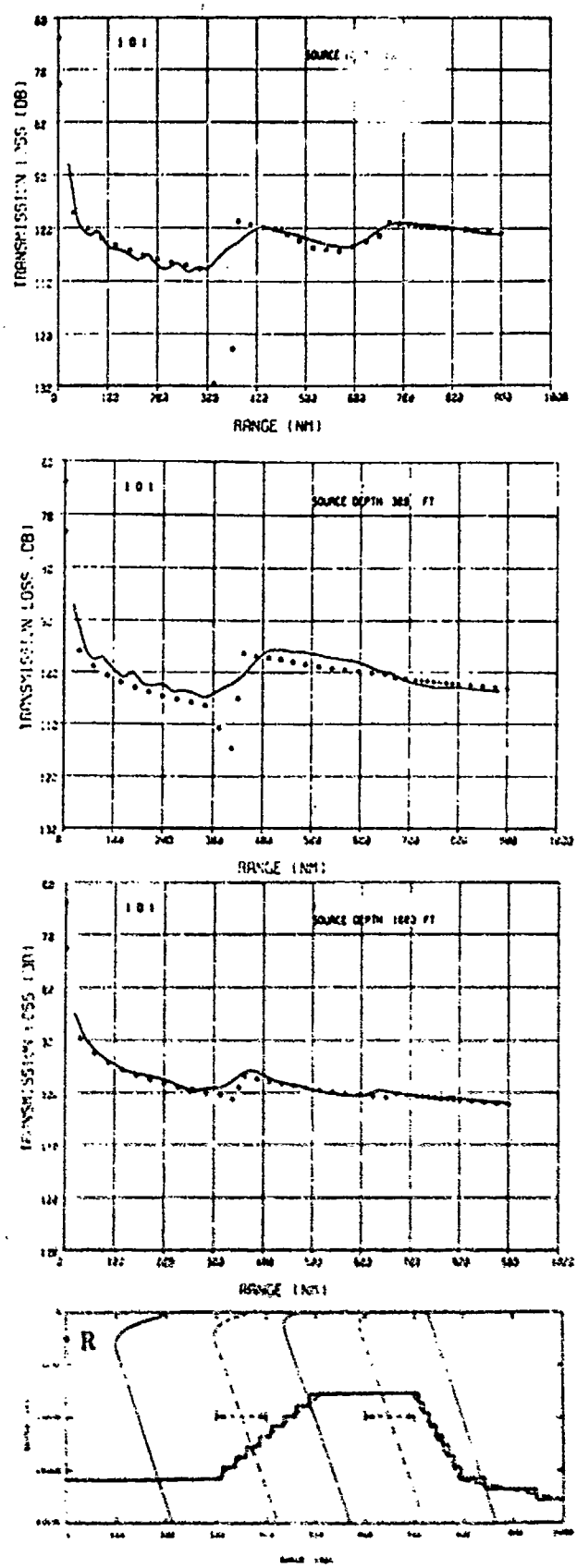

Figure 4-14 Comparison of Range-Smoothed Propagation Loss Versus Range for Test Case 1D1 (2500-ft Receiver-R) for Frequency of 128 Hz. Model(■), PE(—).

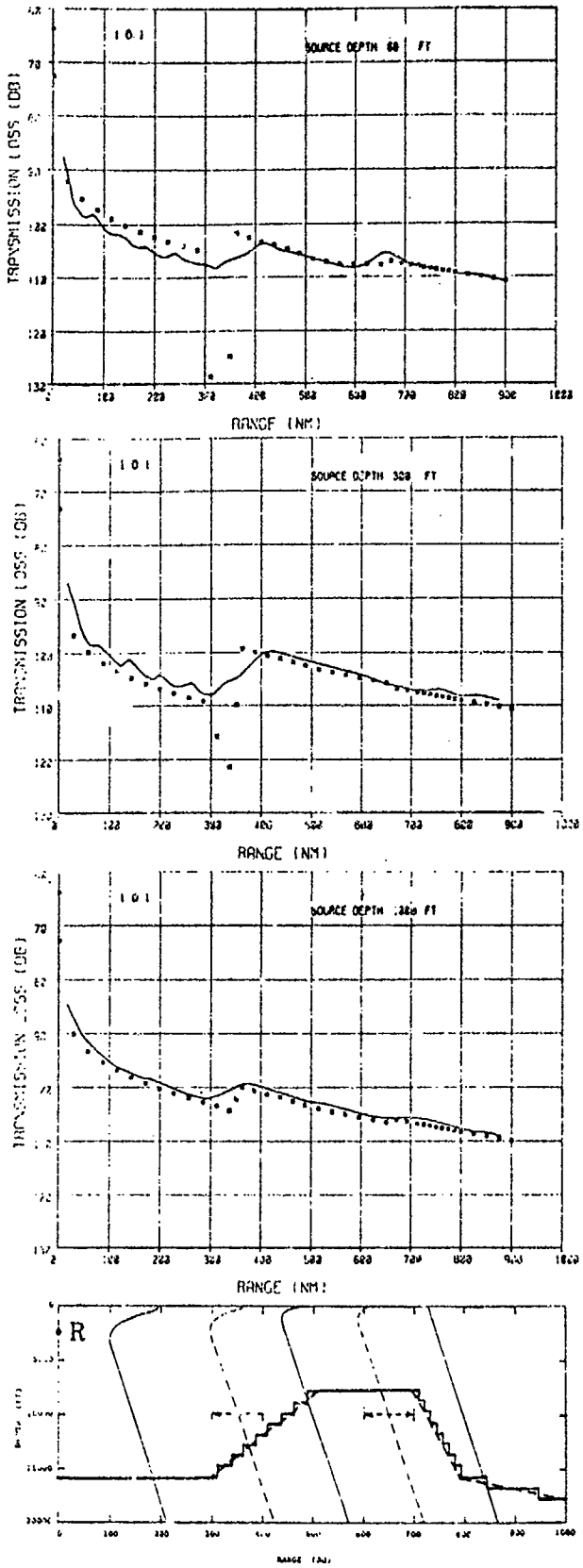

Figure 4-15 Comparison of Range-Smoothed Propagation Loss Versus Range for Test Case 1D1 (2500-ft Receiver-R) for Frequency of 256 Hz. Model(■), PE(—).

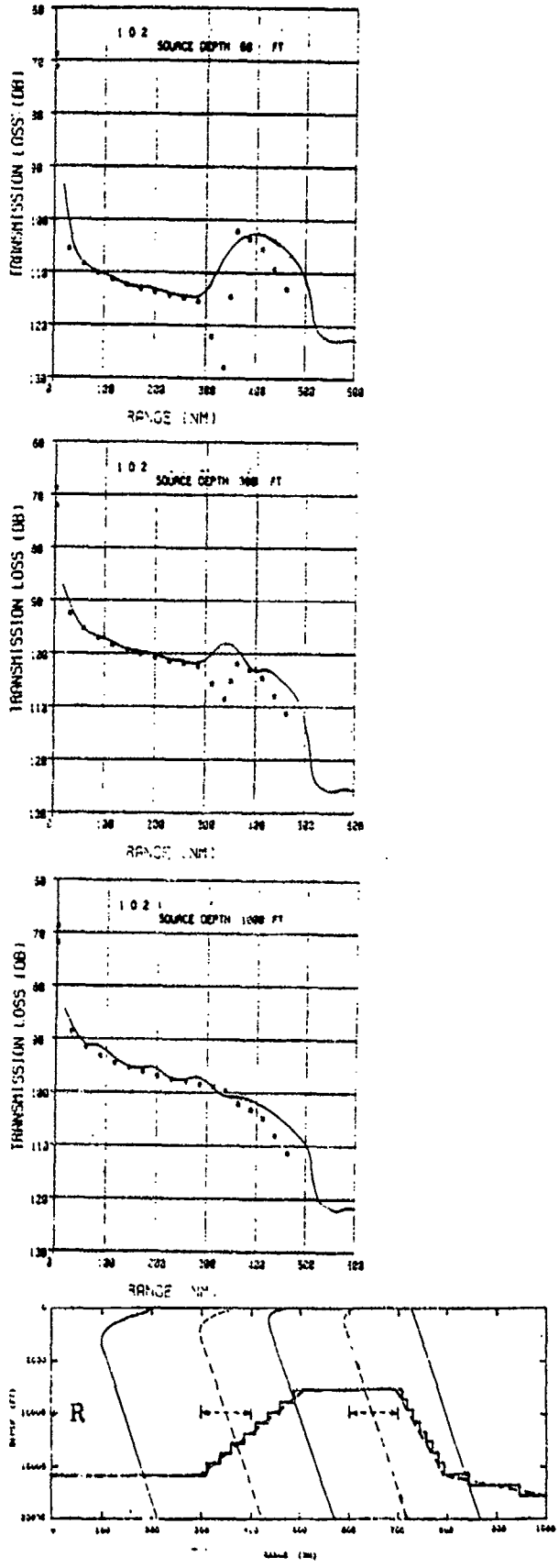

Figure 4-16 Comparison of Range-Smoothed Propagation Loss Versus Range for Test Case 1D2 (10000-ft Receiver-R) for Frequency of 64 Hz. Model(■), PE(—).

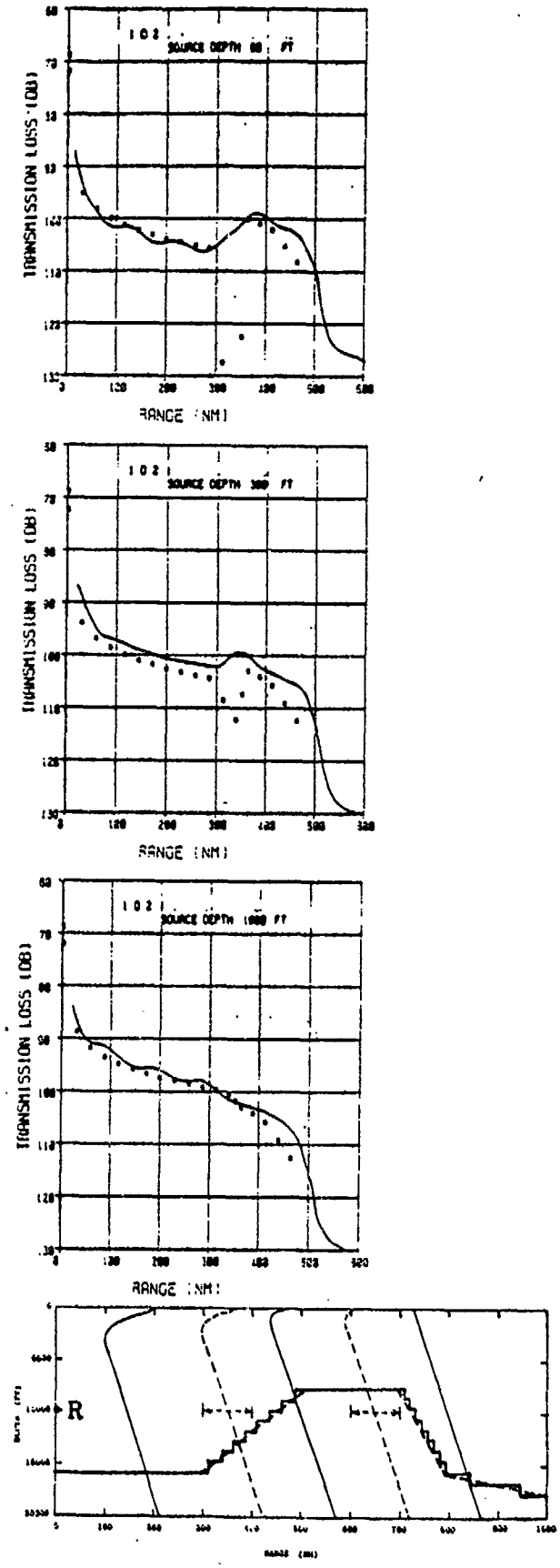

Figure 4-17 Comparison of Range-Smoothed Propagation Loss Versus Range for Test Case 1D2 (10000-ft Receiver-R) for Frequency of 128 Hz. Model(■), PE(—).

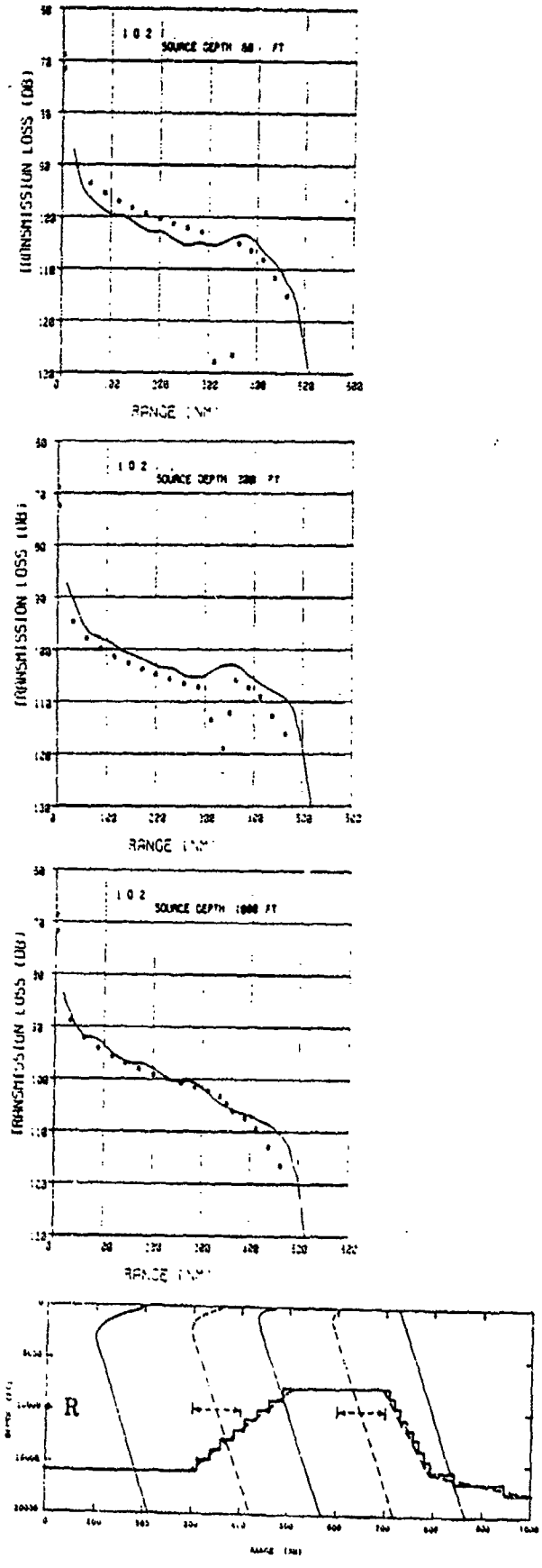

Figure 4-18 Comparison of Range-Smoothed Propagation Loss Versus Range for Test Case 1D2 (10000-ft Receiver-R) for Frequency of 256 Hz. Model(■), PE(—).

4.2 TEST CASE 2

The sound-speed structure for this case (bottom of Figure 4-19) begins with the same profile as Case 1 but evolves into a strong-thermocline warmer profile, a double-channel profile and two Bermuda-like profiles, the first containing a slight upper channel, the second a large but weak, negative sound-speed gradient.

Problems encountered in the first 300 miles have been addressed in the discussion of Case 1. This case was designed to address problems associated with the approximate eigenfunctions in the double-channel profile as well as the adiabatic treatment of its development and decay.

Both cases considered below are for a 3000 ft (axis-depth of the first profile) receiver. The double channel is assumed (in the PE continuous evolution of the sound-speed profile) to develop as a split in the main sound channel of the first profile. By using an axis-depth receiver, low-angle rays (or modes) are introduced which split between these channels. As the channel diminishes in size (in the first Bermuda-like profile) some of these escape to the full channel leaving only a few in the upper channel. The 1000-ft source is on the axis of the first double channel and just below the bottom of the second double channel. The 300-ft source is just above the trapping region of both channels.

4.2.1 Test Case 2A1 - Flat Bottom, 3000-ft Receiver

64, 128 and 256 Hz Comparisons (Figures 4-19, 4-20, and 4-21). At 64-Hz the entire evolution is handled

well with ~2 dB errors at most. However, at 128-Hz propagation losses from the 1000-ft source on the axis of the first upper channel (800 to 1100 nm) are being significantly overestimated. (Note that at 64 Hz it is being slightly underestimated and at 256 Hz there is essentially no error.) The upper duct effectively traps 2, 6 and 11 normal modes at 64, 128 and 256 Hz, respectively. The model assumes that there are enough modes contributing that the detailed eigenfunctions may be replaced by their envelopes. This approximation becomes less accurate as the number of modes becomes small. The agreement at 64 Hz may be fortuitous, whereas at 128 Hz the real magnitude of the problem may be apparent. By 256 Hz there are probably enough modes that the approximation is valid.

The second double channel should pose similar problems. However, none of the sources is contained in the upper channel and the effect is less noticeable. The discrepancy for 256 Hz at 1000 ft may relate to the treatment of sources located in interior shadow zones of modes. The present treatment is to apply the caustic field throughout such regions whereas the field should, in fact, decay.

4.2.2 Test Case 2D1 - Broad Ridge, 3000-ft Receiver

64, 128 and 256 Hz Comparisons (Figures 4-22, 4-23, and 4-24). By introducing a broad ridge, the deeper cycling paths are eliminated, leaving only those near the axis and magnifying the double-channel effects described above (c.f., 128 Hz for the 1000-ft source). As the second double-channel profile is introduced at 1100 nm, the levels drop abruptly indicating very little trapping in the upper channel and strong shielding from modes trapped in the lower channel.

The major discrepancies in these cases (aside from those already discussed) occur at sufficiently high values of transmission loss (> 120 dB) to be inconsequential.

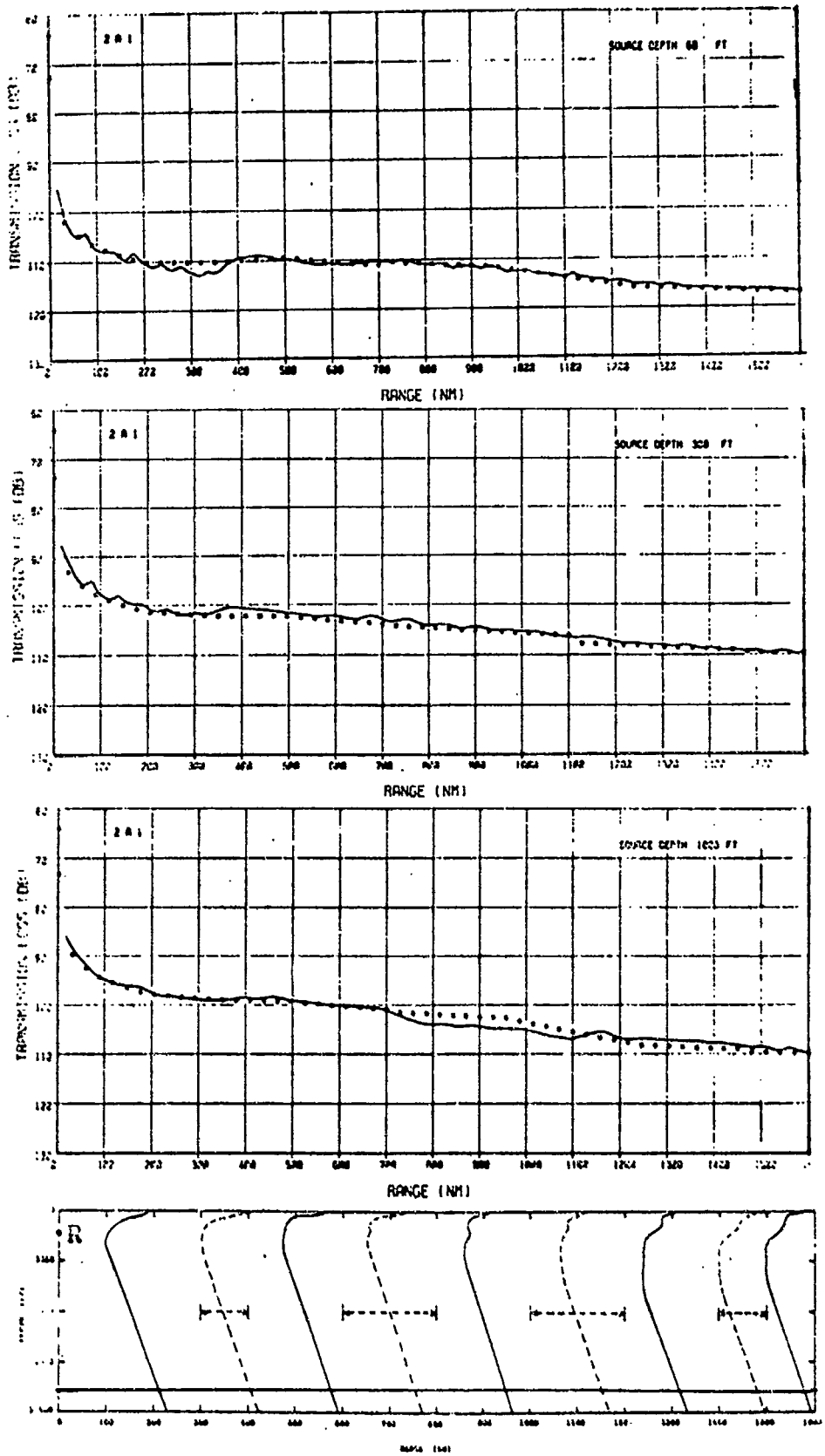

Figure 4-19 Comparison of Range-Smoothed Propagation Loss Versus Range for Test Case 2A1 (3000-ft Receiver-R) for Frequency of 64 Hz. Model(■), PE(—).

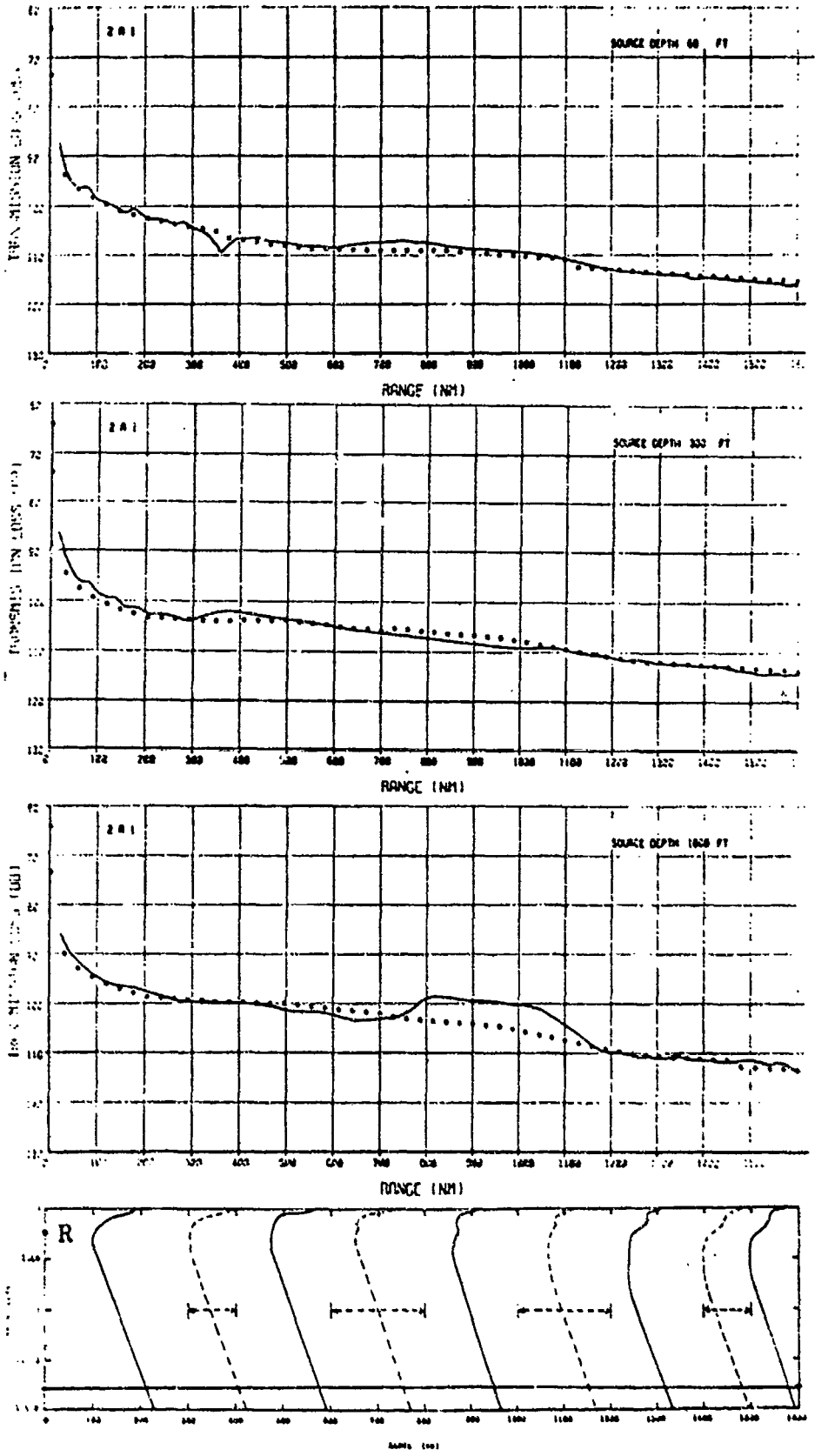

Figure 4-20 Comparison of Range-Smoothed Propagation Loss Versus Range for Test Case 2A1 (3000-ft Receiver-R) for Frequency of 128 Hz. Model(■), PE(—).

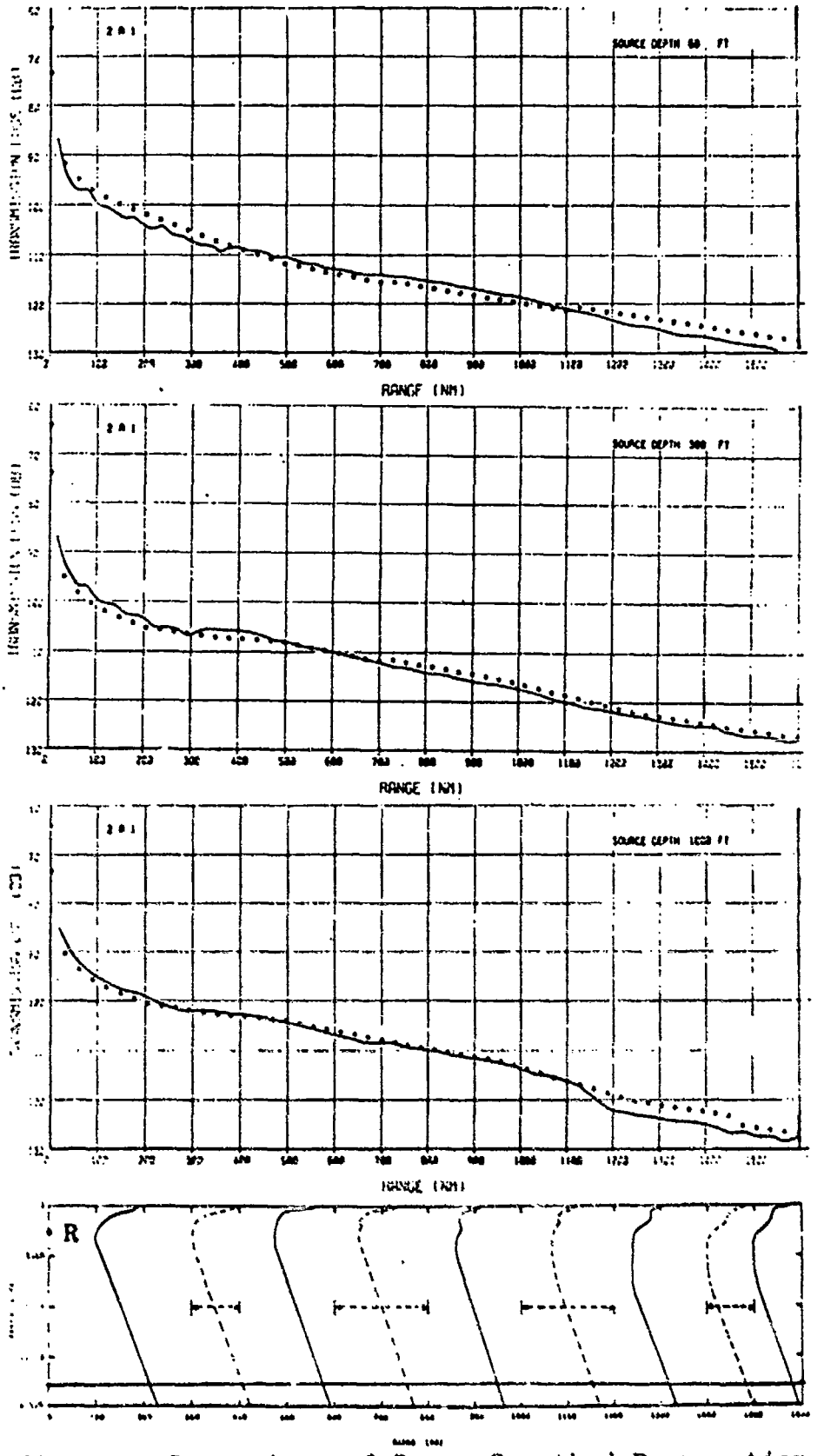

Figure 4-21 Comparison of Range-Smoothed Propagation Loss Versus Range for Test Case 2A1 (3000-ft Receiver-R) for Frequency of 256 Hz. Model(■), PE(—).

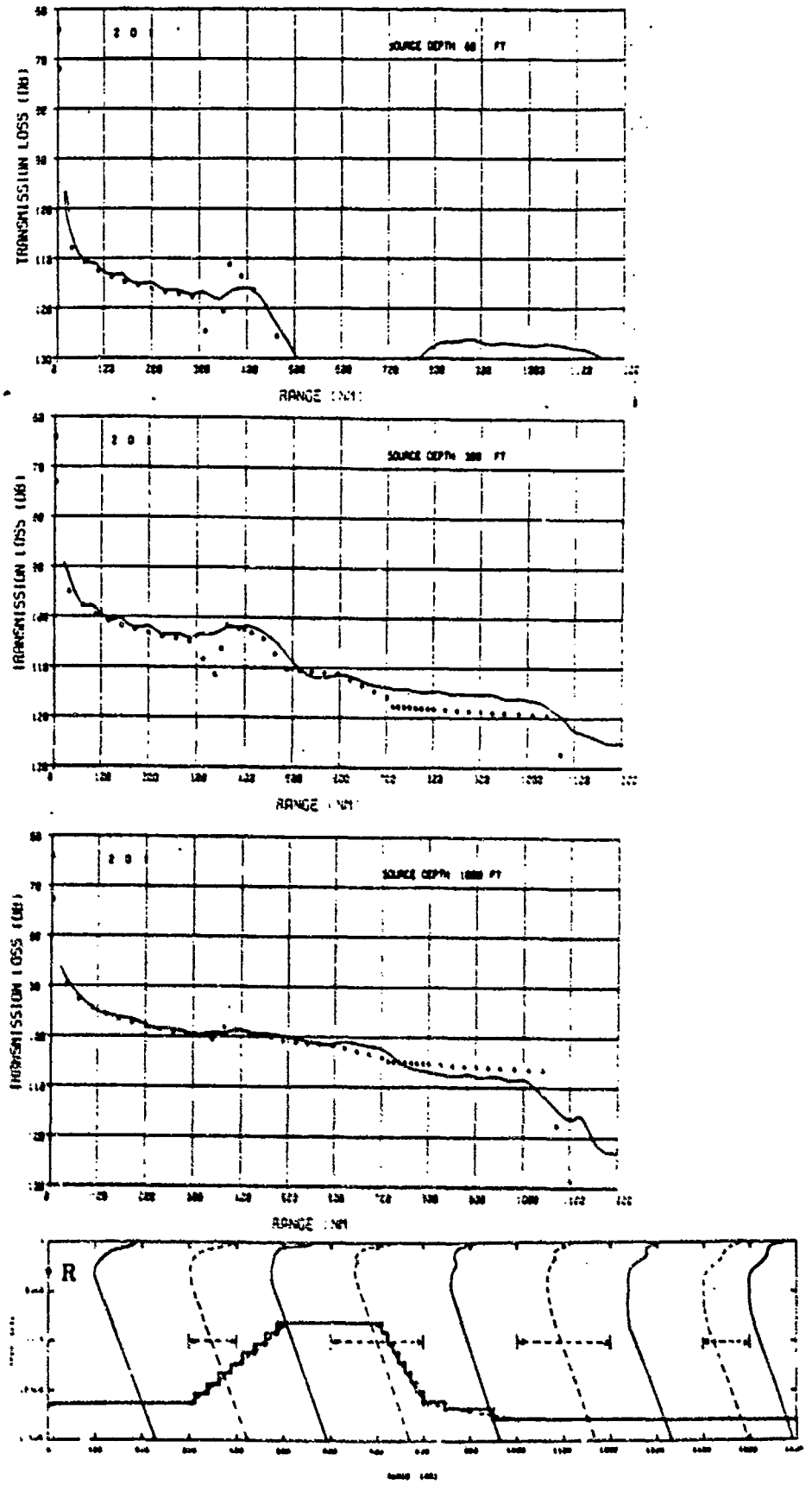

Figure 4-22 Comparison of Range-Smoothed Propagation Loss Versus Range for Test Case 2D1 (3000-ft Receiver-R) for Frequency of 64 Hz. Model(■), PE(—).

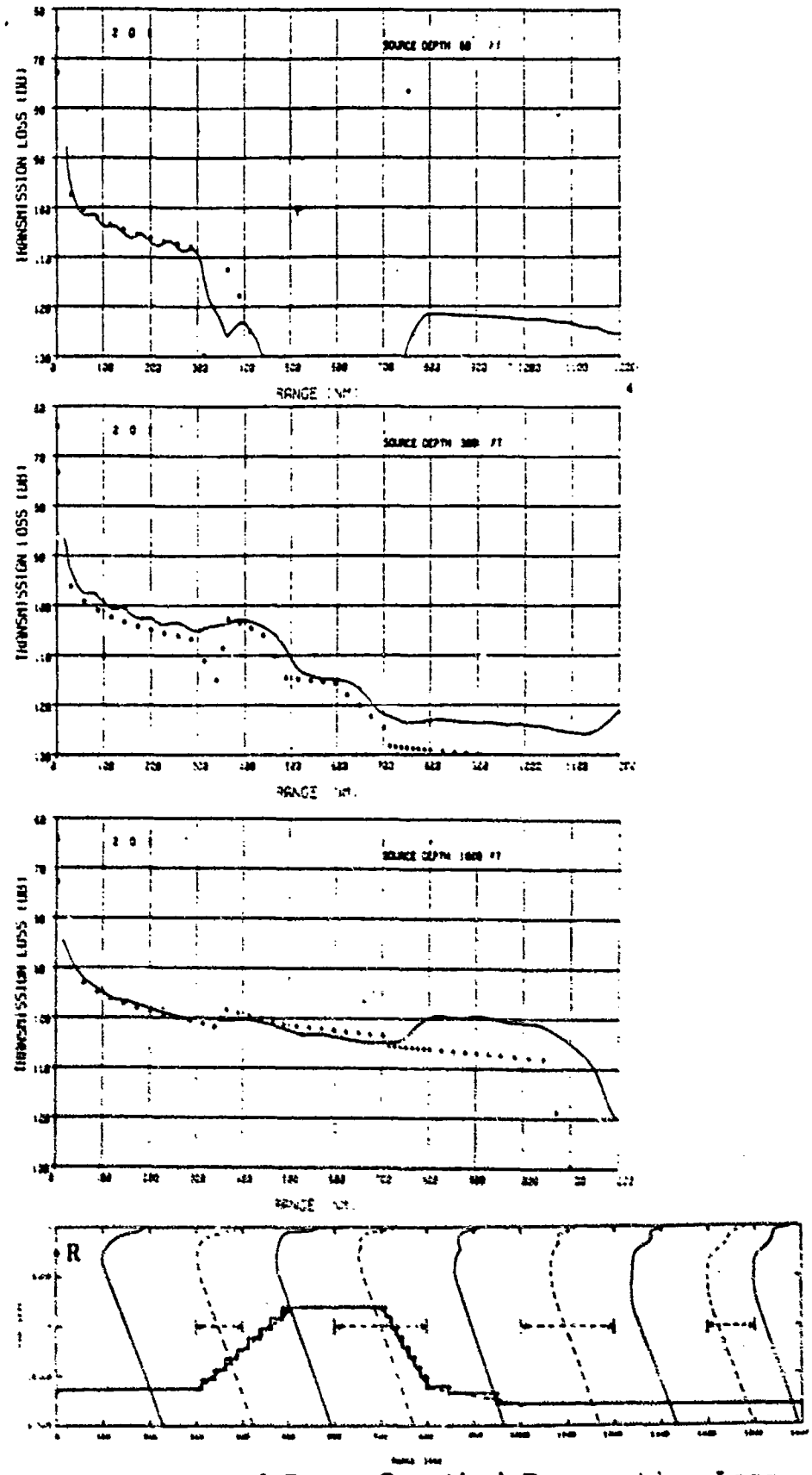

Figure 4-23 Comparison of Range-Smoothed Propagation Loss Versus Range for Test Case 2D1 (3000-ft Receiver-R) for Frequency of 128 Hz. Model(■), PE(—).

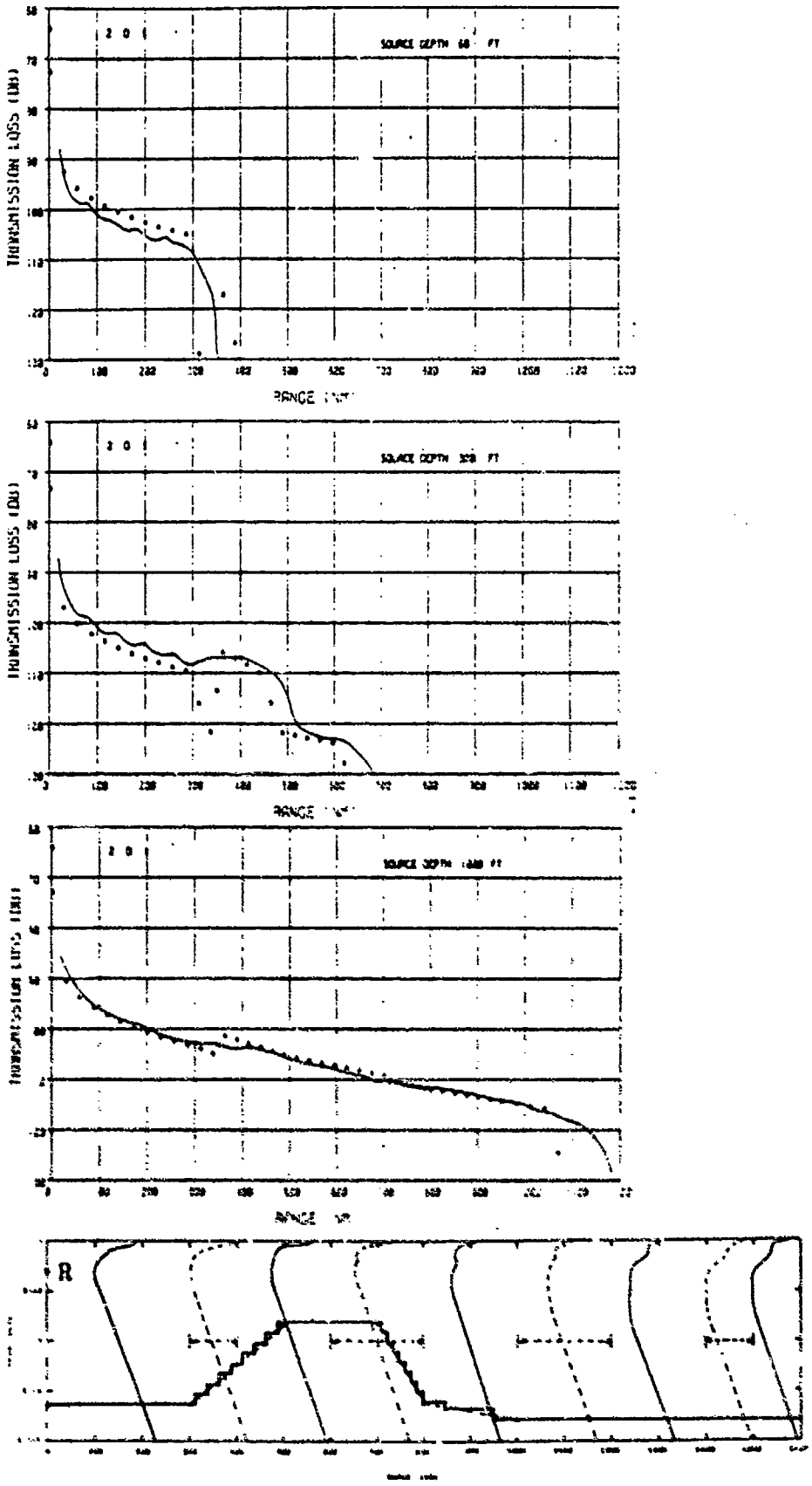

Figure 4-24 Comparison of Range-Smoothed Propagation Loss Versus Range for Test Case 2D1 (3000-ft Receiver-R) for Frequency of 256 Hz. Model(■). PE(—).

4.3 TEST CASE 3

The sound-speed structure for this case is the reverse of that used in Test Case 1. It corresponds to propagation to a receiver in a cold, high latitude from sources to the south.

4.3.1 Test Cases 3A1 and 3A2 - Flat Bottom, 1000- and 5000-ft Receivers

64, 128 and 256 Hz Comparisons (Figures 4-25 through 4-30). Two problems are illustrated in these cases. First, for the 1000-ft receiver and 1000-ft source in the first profile (< 300 miles) the model underestimates the level by 3 dB at all frequencies. Because the source and receiver are at the same depth in a range-independent environment, the peak focal regions correspond to cusped caustics. The mode treatment used here effectively recognizes this focusing at one end (the source) but not the other. The up- and down-going pairs of paths being added at the receiver actually have a zero-phase difference rather than the random relative phase assumed by the model. The approximate summation will thus yield a 3 dB lower level than the proper summation.

The second problem occurs at longer ranges (> 800 nm) for the shallow source at 256 Hz for both receivers, and 64 Hz for the shallow receiver. The model is overestimating the level by 3 dB in all cases. At 64 Hz this difference appears to be due to surface-image interference at the receiver (since it is not present for the deep receiver). At 256 Hz surface-image interference might account for the difference at the 1000-ft receiver but seems unlikely as the mechanism at 5000 ft. The difference is consistent with the

problems in Test Case 1 for the shallow source at 256 Hz, where it appears that an extension of the image-interference correction to greater depth than the second rms depth may be required.

4.3.2 Test Cases 3C1 and 3C2 - Gradual Downslope 1000- and 5000-ft Receivers

64, 128 and 256 Hz Comparisons (Figures 4-31 through 4-36). In this case the sound-channel develops more rapidly than the water depth increases, resulting in a substantial stripping of high-angle modes. With the third profile only the high-angle modes could contribute to the level and a large increase in loss occurs. Even for the deepest source, the energy is sufficiently concentrated near the axis that very little is available.

The model has a tendency to overestimate the final level from the deep source, especially at the lower frequencies. The field in these cases is composed solely of diffraction contributions from the remaining modes, all of whose upper turning points are deeper than 1000 ft. In the model, the extension of the diffraction field beyond the turning point is based on the sound-speed gradient at the turning point. For the near axial modes this gradient is quite weak and the diffraction fields would be extended much further than in a complete treatment (which would recognize the significant increase in gradient above the turning point).

A peculiar effect occurs for the 1000-ft source, where the level to the deep (5000-ft) receiver is higher than to the shallow (1000-ft) receiver. This is probably due to the stronger coupling by the 5000-ft receiver to the few higher-angle modes which propagate at this range.

The final figure (4-36, 60 ft) magnifies the surface-image interference problem introduced by limiting the effect to the depths below the rms point in phase. The high-loss bottom results in a narrow aperture of rays (between 9.9 and 11.0 degrees) reaching the source at 60 ft from this receiver in the first few hundred miles. The phase difference between up- and down-going paths is larger than the rms cut-off point. In fact, however, the phase differences over the aperture are small and all paths in the aperture experience constructive interference at 60 ft for 256 Hz. The corresponding decrease in level varies from 1 to 3 dB depending on the path. This appears to account for most of the observed discrepancy.

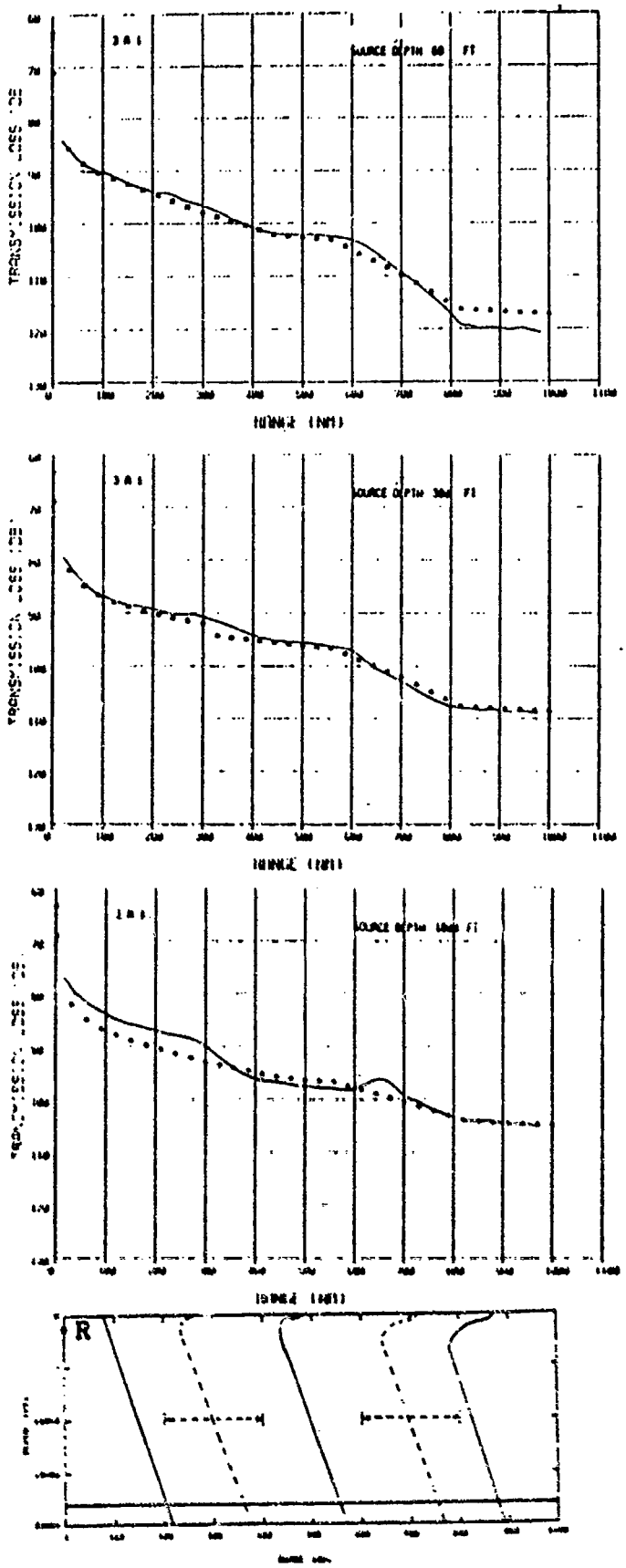

Figure 4-25 Comparison of Range-Smoothed Propagation Loss Versus Range for Test Case 3A1 (1000-ft Receiver-R) for Frequency of 64 Hz. Model(■), PE(—).

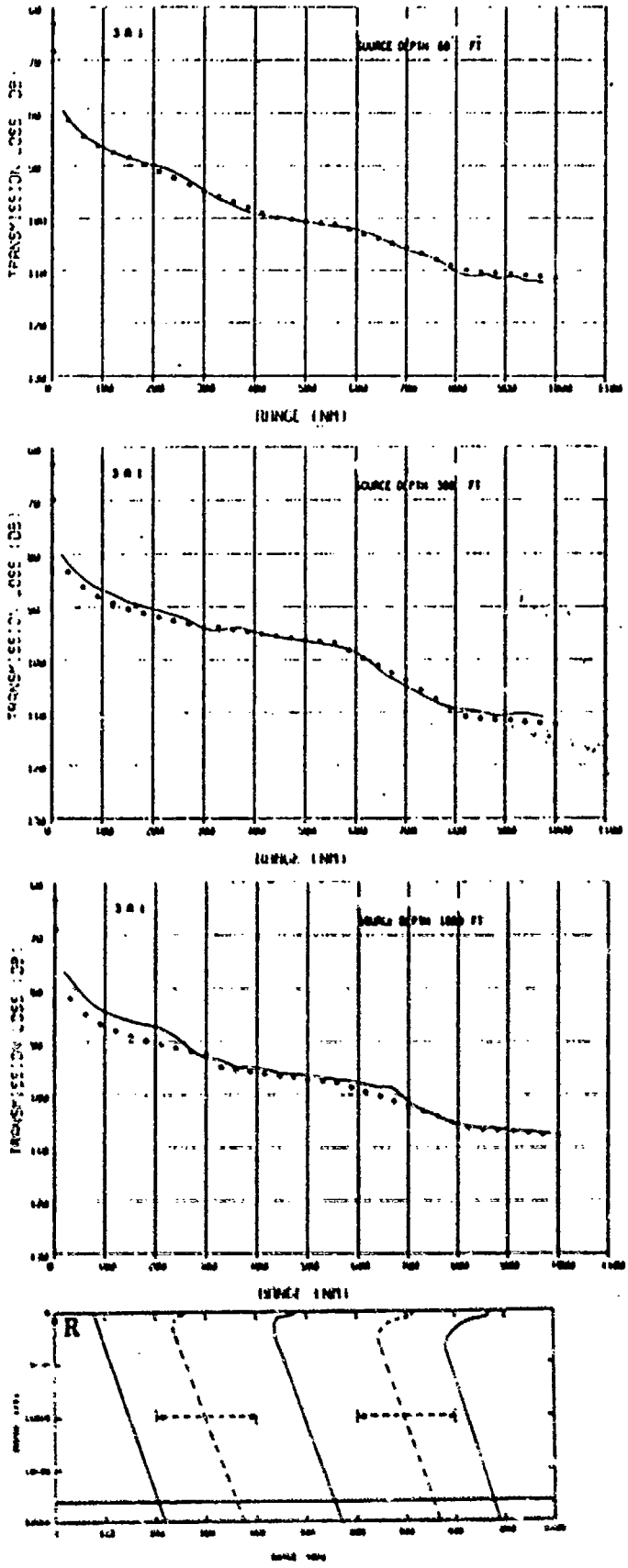

Figure 4-26 Comparison of Range-Smoothed Propagation Loss Versus Range for Test Case 3A1 (1000-ft Receiver-R) for Frequency of 128 Hz. Model(■), PE(—).

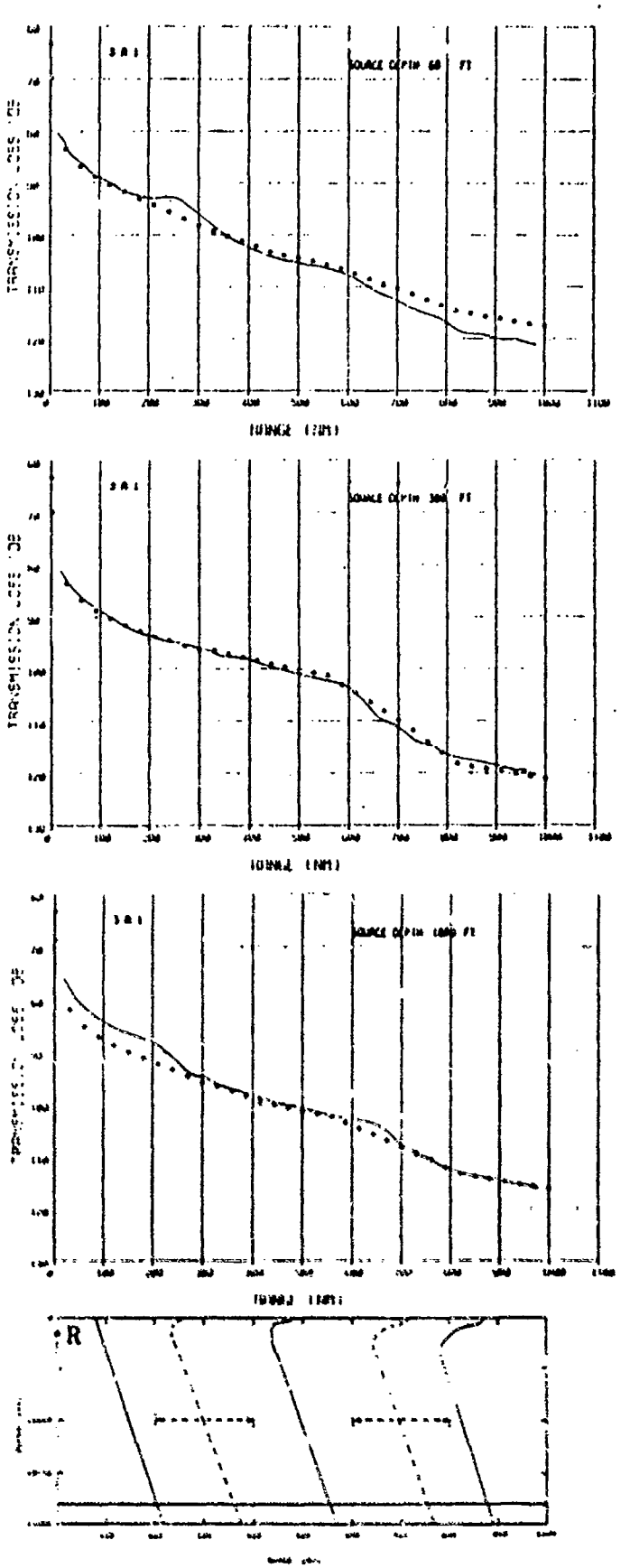

Figure 4-27 Comparison of Range-Smoothed Propagation Loss Versus Range for Test Case 3A1 (1000-ft Receiver-R) for Frequency of 256 Hz. Model(■), PE(—).

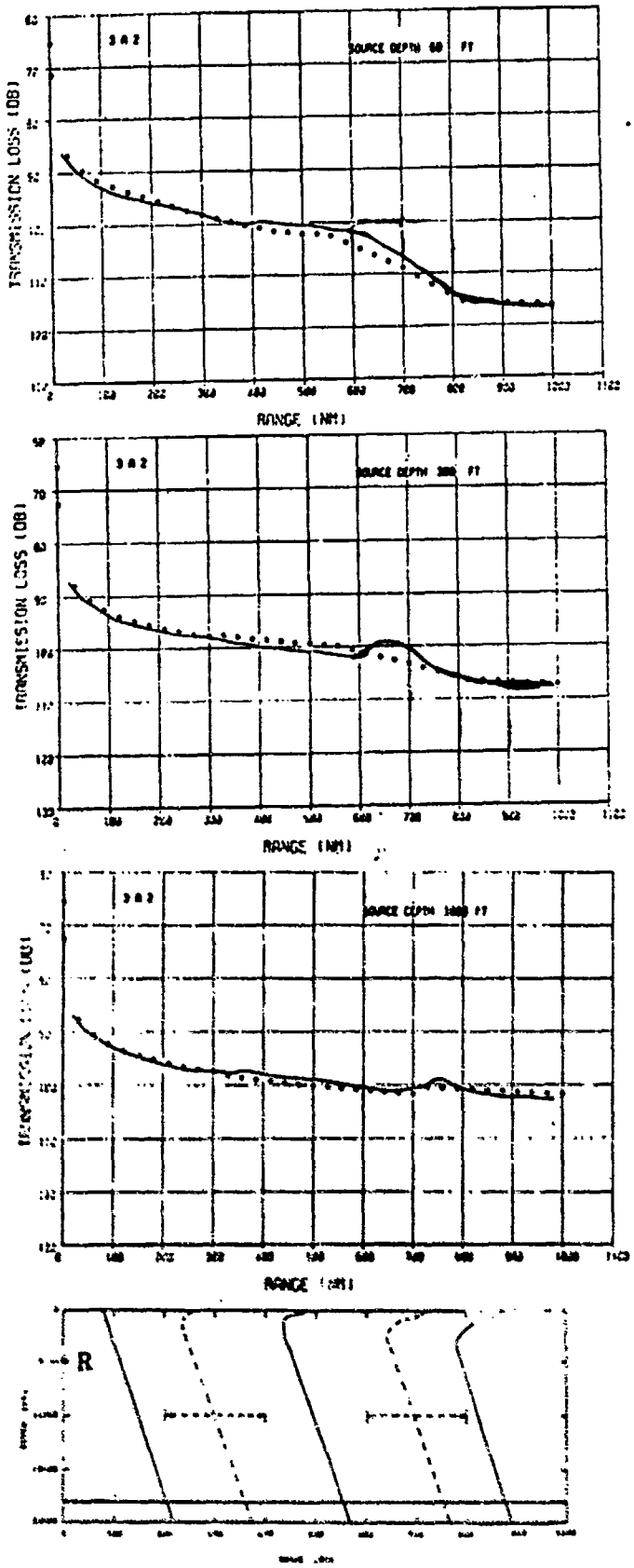

Figure 4-28 Comparison of Range-Smoothed Propagation Loss Versus Range for Test Case 3A2 (5000-ft Receiver-R) for Frequency of 64 Hz. Model(■), PE(—).

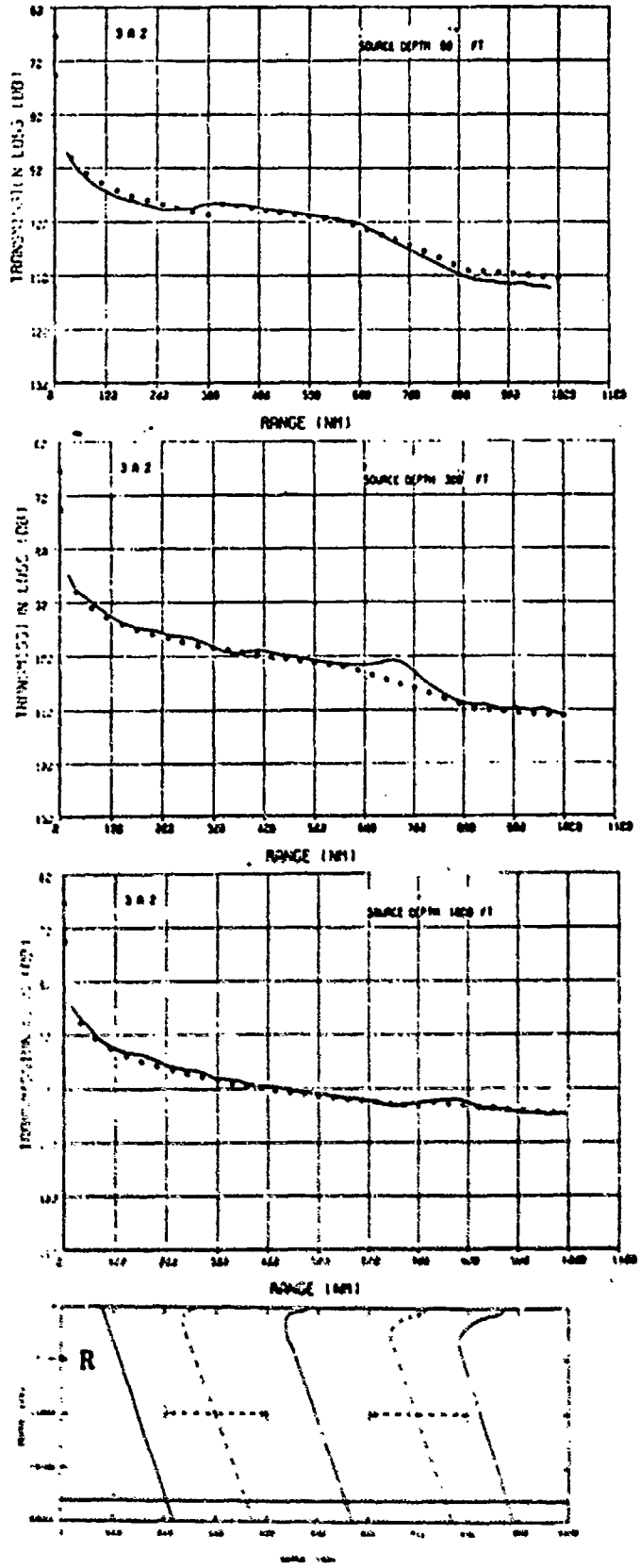

Figure 4-29 Comparison of Range-Smoothed Propagation Loss Versus Range for Test Case 3A2 (5000-ft Receiver-R) for Frequency of 128 Hz. Model(■), PE(—).

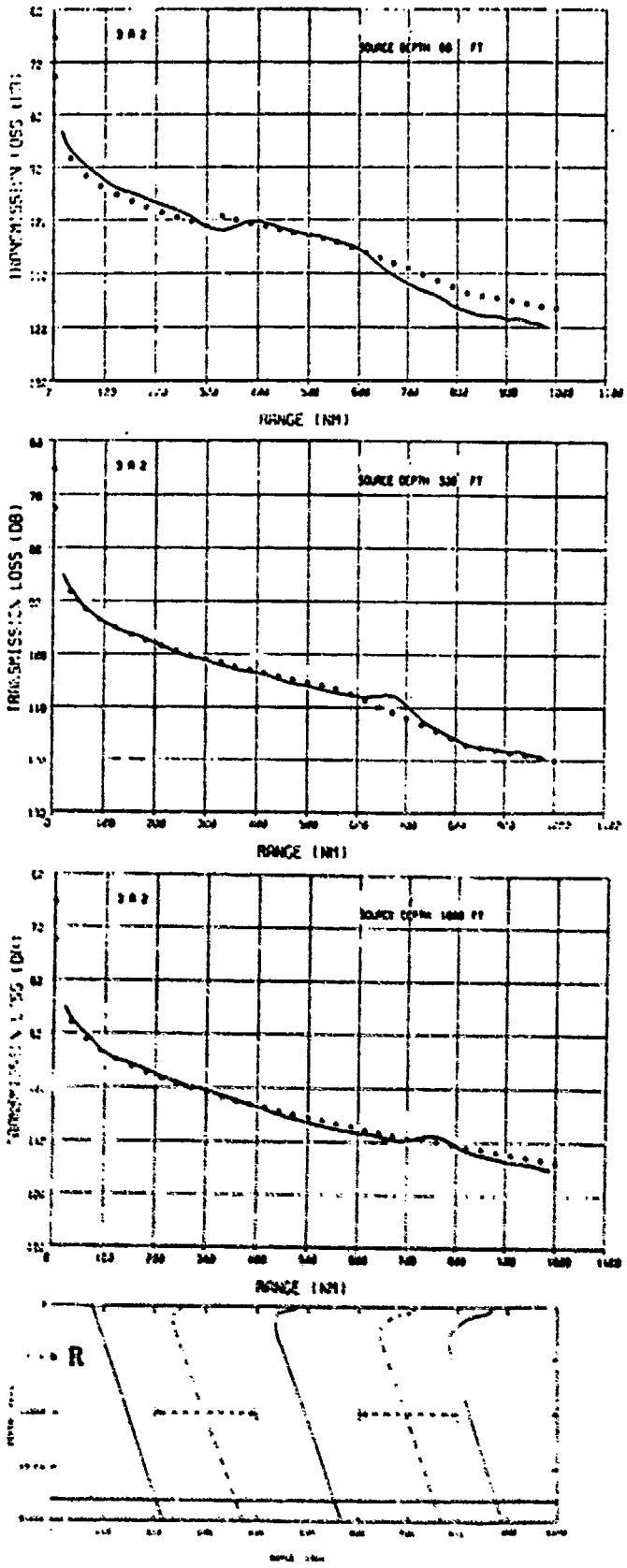

Figure 4-30 Comparison of Range-Smoothed Propagation Loss Versus Range for Test Case 3A2 (5000-ft Receiver-R) for Frequency of 256 Hz. Model(■), PE(—).

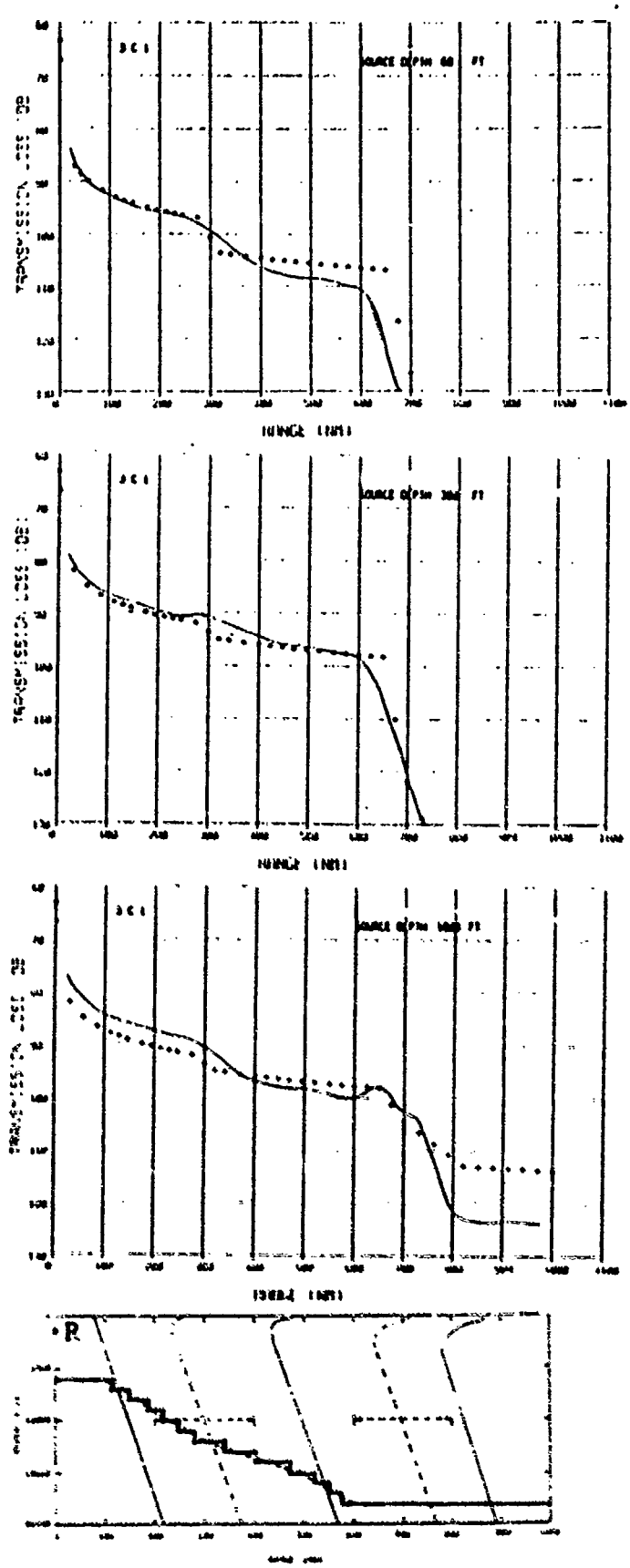

Figure 4-31 Comparison of Range-Smoothed Propagation Loss Versus Range for Test Case 3C1 (1000-ft Receiver-R) for Frequency of 64 Hz. Model(■), PE(—).

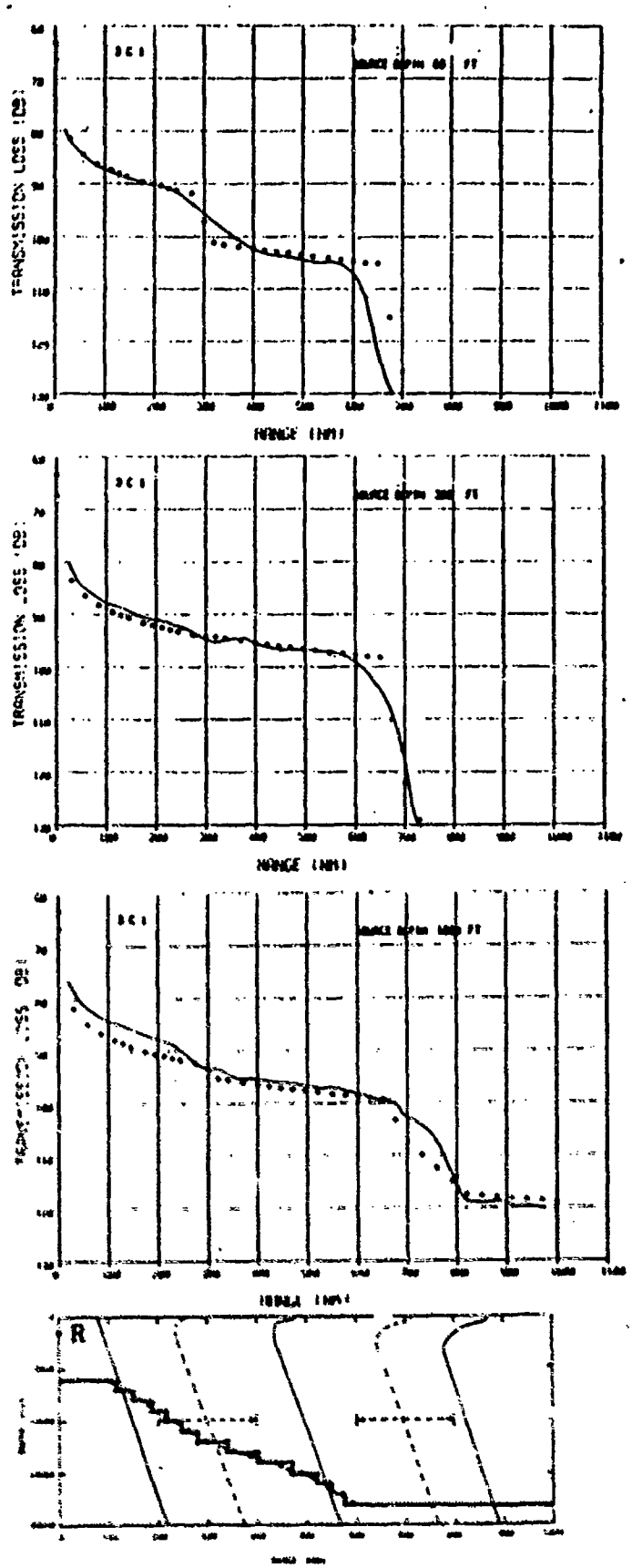

Figure 4-32 Comparison of Range-Smoothed Propagation Loss Versus Range for Test Case 3C1 (1000-ft Receiver-R) for Frequency of 128 Hz. Model([redacted]), PE(—).

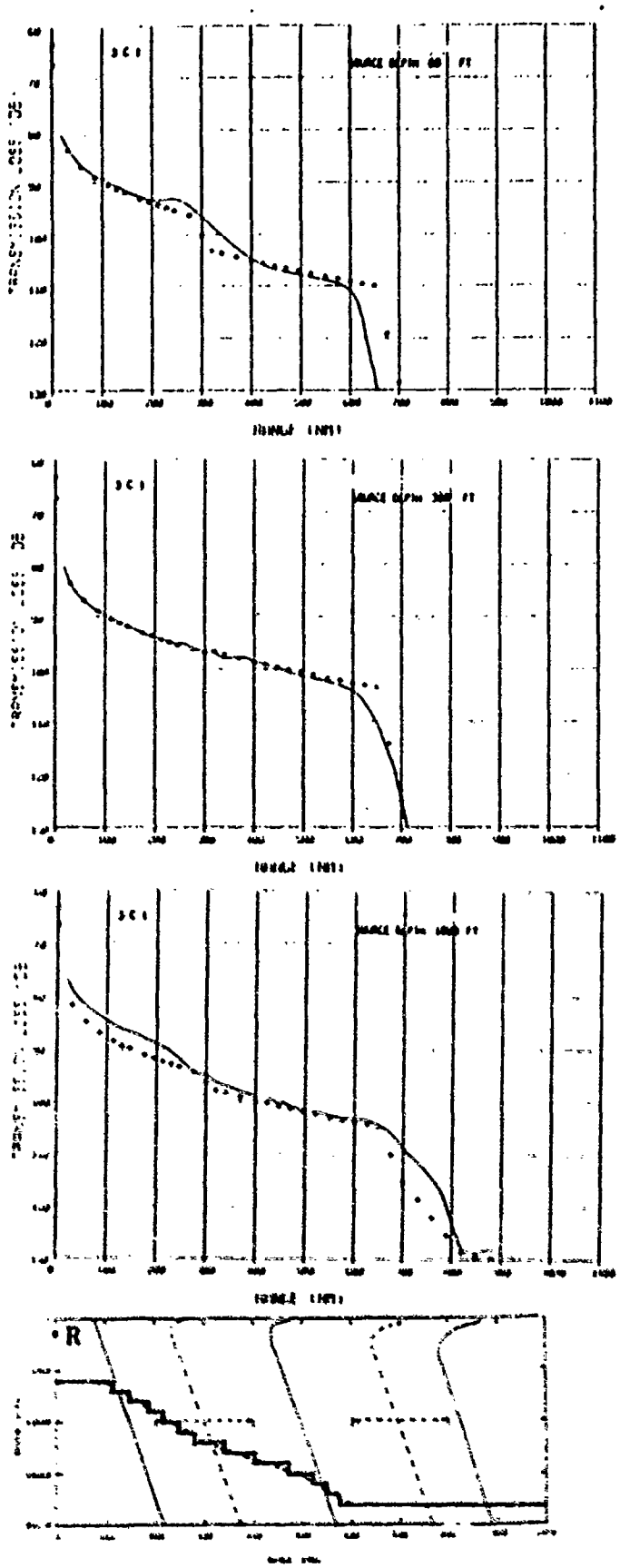

Figure 4-33 Comparison of Range-Smoothed Propagation Loss Versus Range for Test Case 3C1 (1000-ft Receiver-R) for Frequency of 256 Hz. Model(■). PE(—).

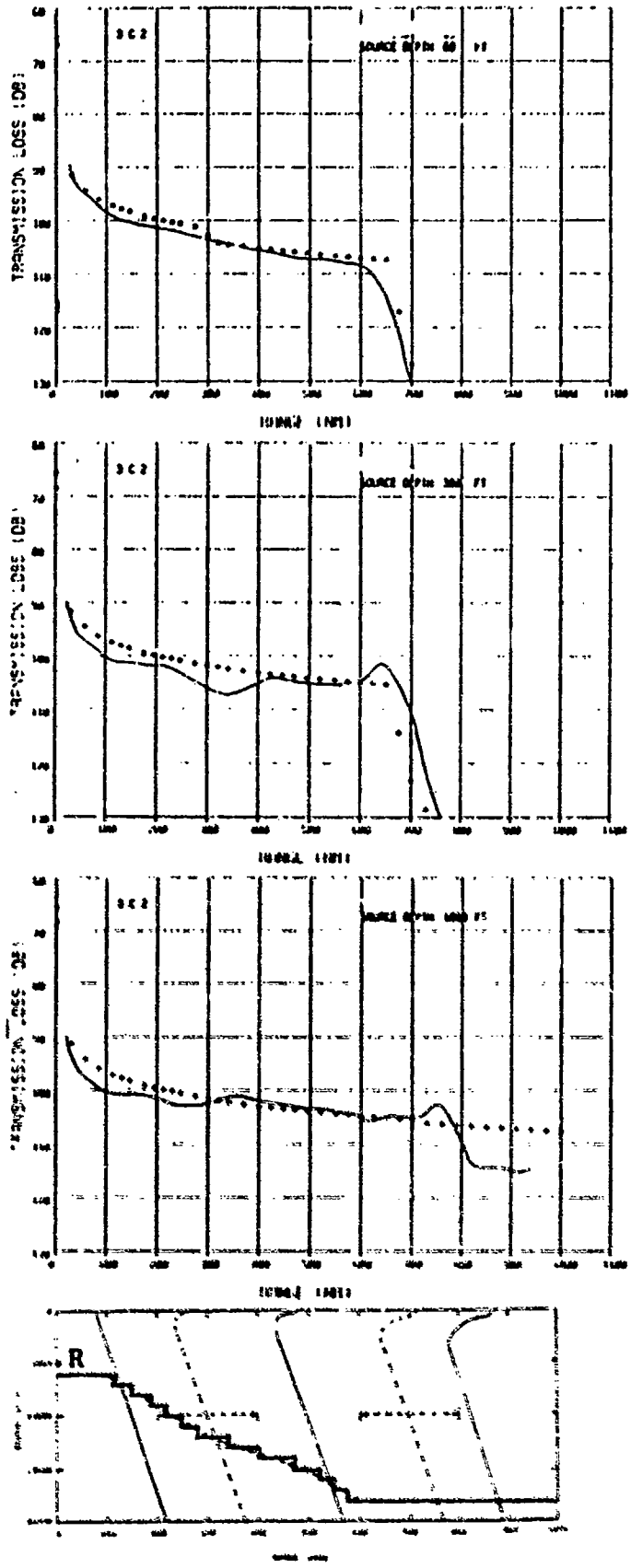

Figure 4-34 Comparison of Range-Smoothed Propagation Loss Versus Range for Test Case 3C2 (5000-ft Receiver-R) for Frequency of 64 Hz. Model (■), PE(—).

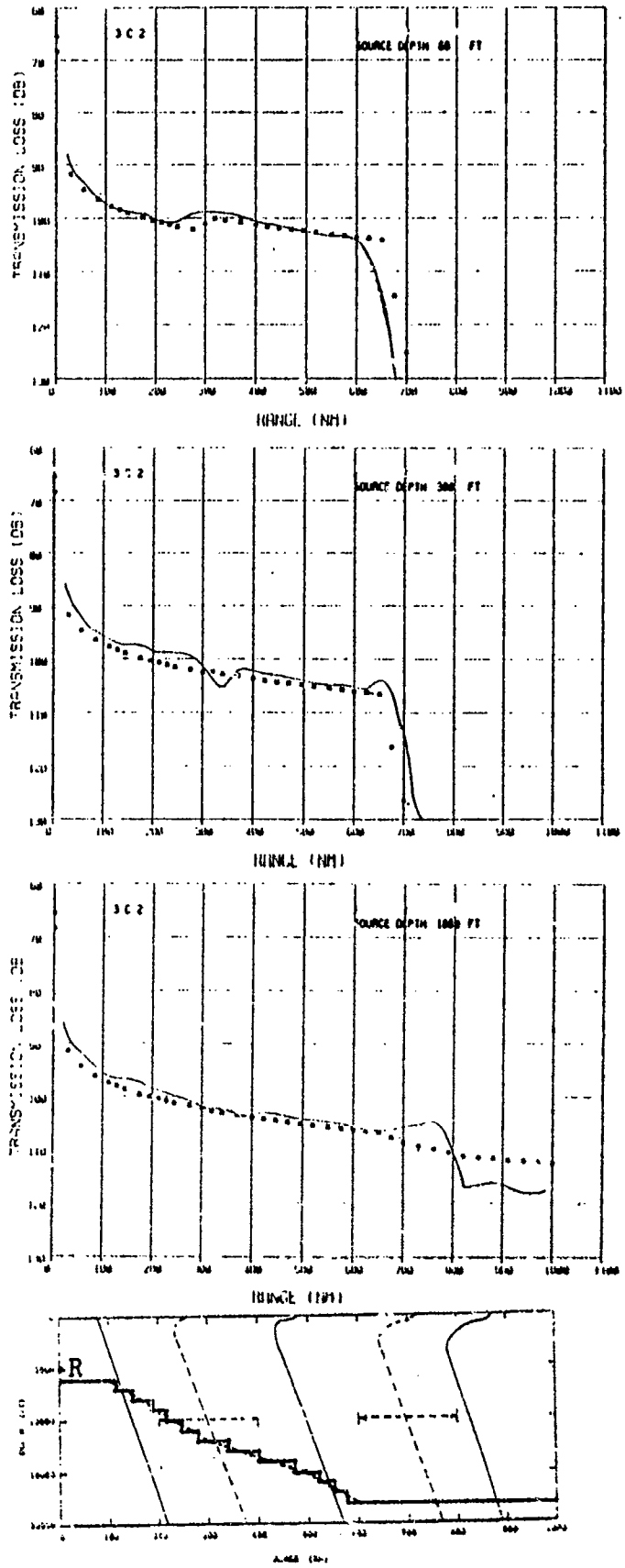

Figure 4-35 Comparison of Range-Smoothed Propagation Loss Versus Range for Test Case 3C2 (5000-ft Receiver-R) for Frequency of 128 Hz. Model (■), PE(—).

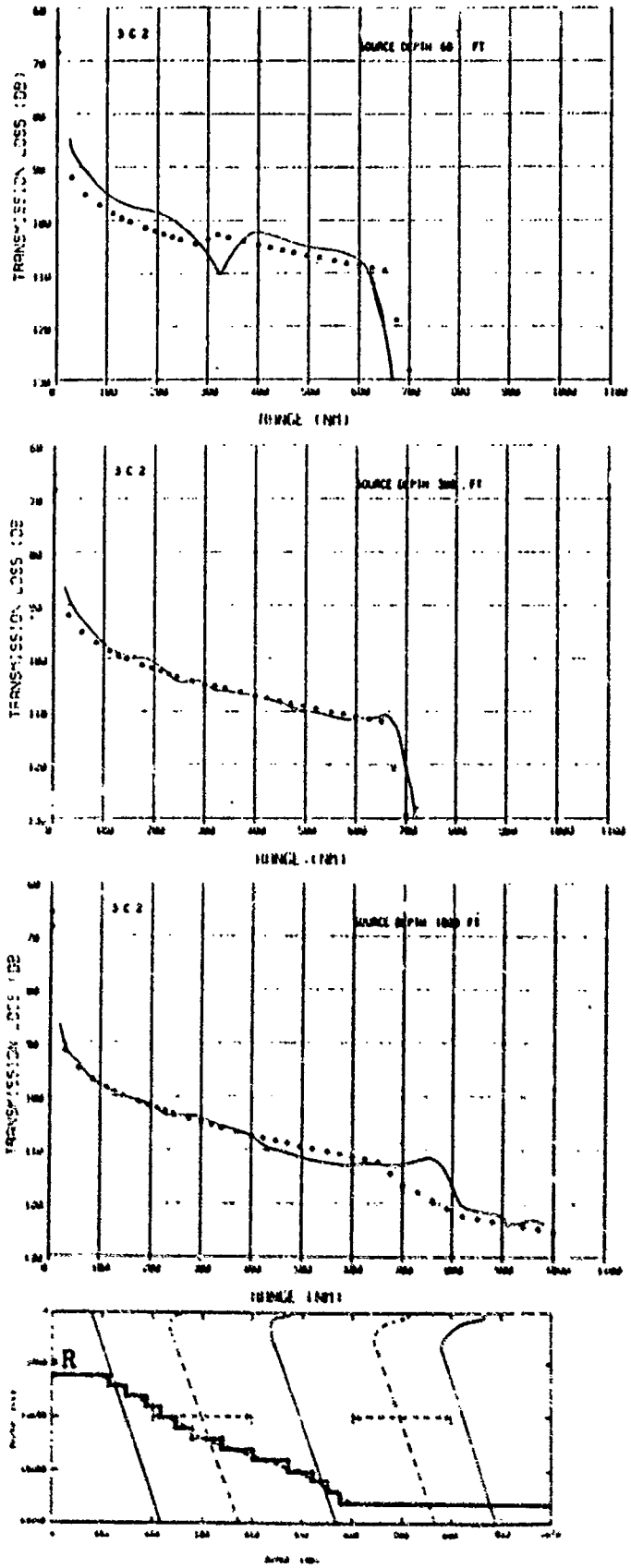

Figure 4-36 Comparison of Range-Smoothed Propagation Loss Versus Range for Test Case 3C2 (5000-ft Receiver-R) for Frequency of 256 Hz. Model (■), PE(—).

4.4 TEST CASE 4

The sound-speed environment for this case (bottom of Figure 4-37) begins with a double channel, followed by a strong-thermocline-gradient single channel, a repeat of the double channel, and finally a deep-axis (Bermuda-like) single channel. A number of model deficiencies associated with double-channel profiles which have already been identified in Test Case 2 will reappear here.

4.4.1 Test Cases 4A1 and 4A2 - Flat Bottom, 4000- and 12000-ft Receivers

64, 128 and 256 Hz Comparisons (Figures 4-37 through 4-42). The 4000-ft receiver is at the axis of the lower channel, whereas the 1000-ft source is at the axis of the upper channel. Discrepancies for this combination in the first 200 miles should indicate the limitations of the double-channel treatment. At all frequencies the model is predicting 3-dB too high an intensity. Assuming no leakage through the subsurface sound-speed maximum at 2000 ft, the difference in actual versus modeled angular aperture at 4000 ft reaching 2000 ft would account for 2 dB of the discrepancy. Focusing effects probably account for the residual differences.

The differences which occur the second time the double channel is encountered (800-1000 nm) are due to ducting effects in the upper channel as already discussed under Test Case 2. The 3-dB difference in long range (> 1200 nm) levels for both receivers to the 60-ft source at 256 Hz is consistent with the surface-image interference problem discussed under Test Case 1.

4.4.2 Test Cases 4D1 and 4D2 - Broad Ridge, 4000- and 12000-ft Receivers

64, 128 and 256 Hz Comparisons (Figures 4-43 through 4-48). This case begins with shallower water (16000 ft) than Case 4A thus restricting the aperture of deep cycling paths. The effect at the 1000-ft source is negligible, however, for the 60-ft source the model consistently underestimates the level at all frequencies. The discrepancy results from the discretization of the modes in terms of axis angle. The critical rays at the axis (which happens to correspond to the 4000-ft receiver) are:

(1) $12^{\circ}.39$ - reaches 60'

(2) $12^{\circ}.94$ - reaches surface

(3) $15^{\circ}.79$ - reaches bottom

(4) $12^{\circ}.54$ - reaches 12000-ft receiver

The modes considered correspond to integral values of this axis angle. Hence the 12° mode only influences 60 ft through its diffraction field. The 13° mode, since it grazes the surface at 1.2 degrees, experiences strong destructive surface image interference at all frequencies (16.6 dB at 64 Hz, 2.6 dB at 128 Hz, and 3.4 dB at 256 Hz). This loss is applied implicitly to the entire aperture from 12 to 13 degrees (including all RR modes in this aperture which reach 60 ft). Only the 14- and 15-degree modes remain with any appreciable energy. For the 12000-ft receiver the first mode considered is the 13°-mode so none of the diffraction field from the 12°-mode is included (hence the larger discrepancy than for the 4000-ft receiver).

If the ray ($12^{\circ}.39$) corresponding to the mode grazing 60-ft had been traced and the energy in the aperture from 12 to 13 degrees assigned to it (as opposed to the 13° mode which was virtually eliminated by surface-image interference), the loss for the 4000-ft receiver at 100 miles associated with this mode alone would be 104, 102, and 101 dB at 64, 128, and 256 Hz, respectively. This level when added to the contribution from other modes (represented essentially by the model prediction) would yield the PE levels to within 1 dB.

The mode-stripping effect of the ridge magnifies the double-channel problems (already discussed), especially for the shallow receiver and the 1000-ft source, between 800 and 1000 miles. The residual discrepancy for the deep sources to this receiver between 1200 and 1300 miles has not been definitively resolved. The level is consistent with leakage from one mode with an upper turning point near 1400 ft. The model clearly underestimates the leakage field. The problem may again be related to mode discretization since the second double-channel profile begins (in the model) at 700 miles when the ridge is still at a depth of 8000 ft. The axial ray grazing the bottom is $7^{\circ}.93$, hence all the energy from 7 to $7^{\circ}.93$ will be erroneously stripped by the bottom. Since this aperture corresponds to the highest-angle (and hence shallowest) surviving modes, the level at 1300 miles would be much higher if the aperture had been included. While the discrepancy here is large, it occurs at a sufficiently high loss that it is not considered a significant model limitation.

Because the ridge effectively blocks all energy to the deep receiver, the only discrepancies in Case 4D2 are

associated with the first profile as already discussed. The trace of a level in the PE results for 64 Hz and the deep sources must correspond to normal modes in the original profile which reach 12000 ft only with their diffraction fields (a case not treated by the model). Again the limitation appears to be insignificant.

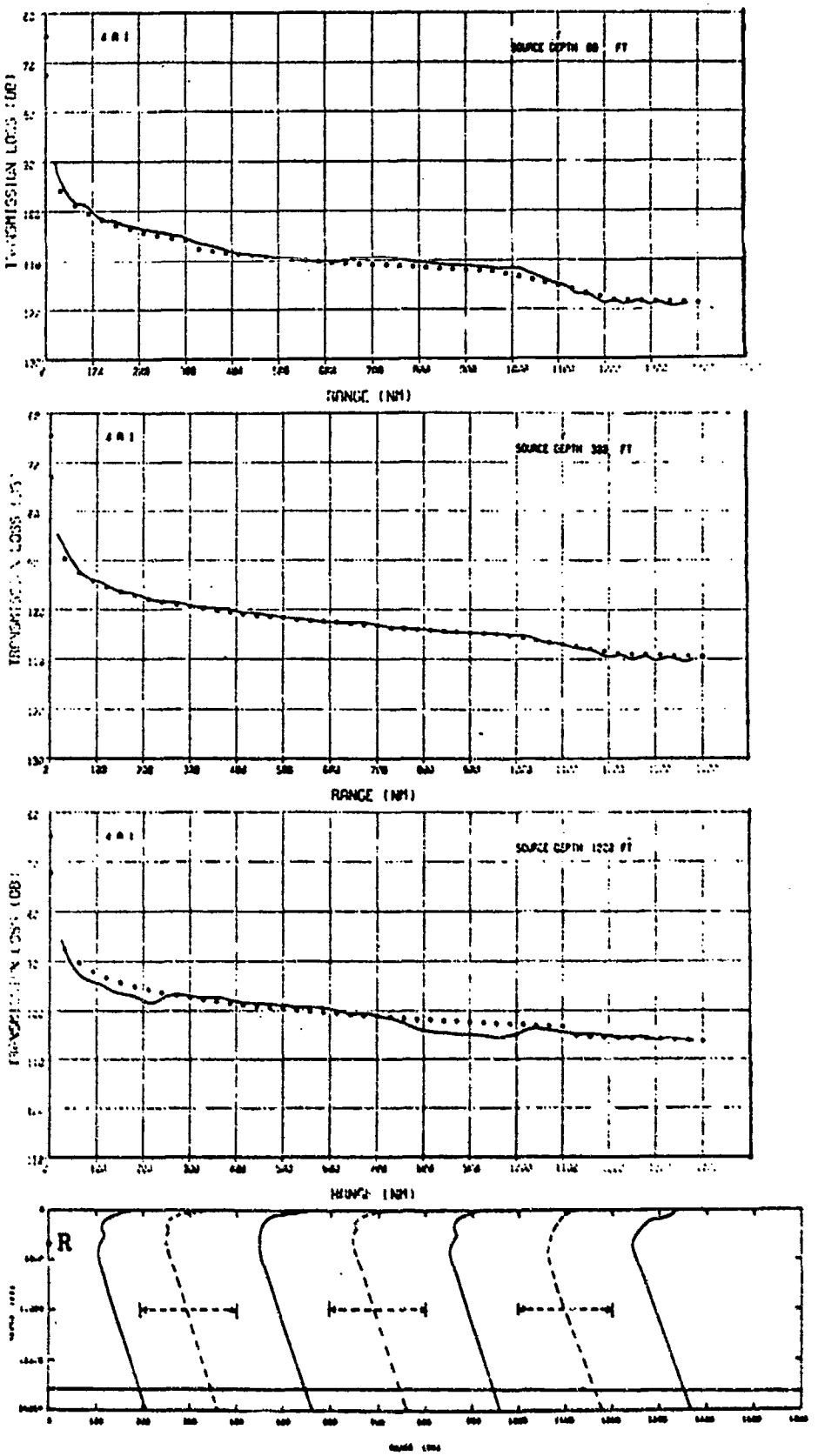

Figure 4-37 Comparison of Range-Smoothed Propagation Loss Versus Range for Test Case 4A1 (4000-ft Receiver-R) for Frequency of 64 Hz. Model (■), PE(—).

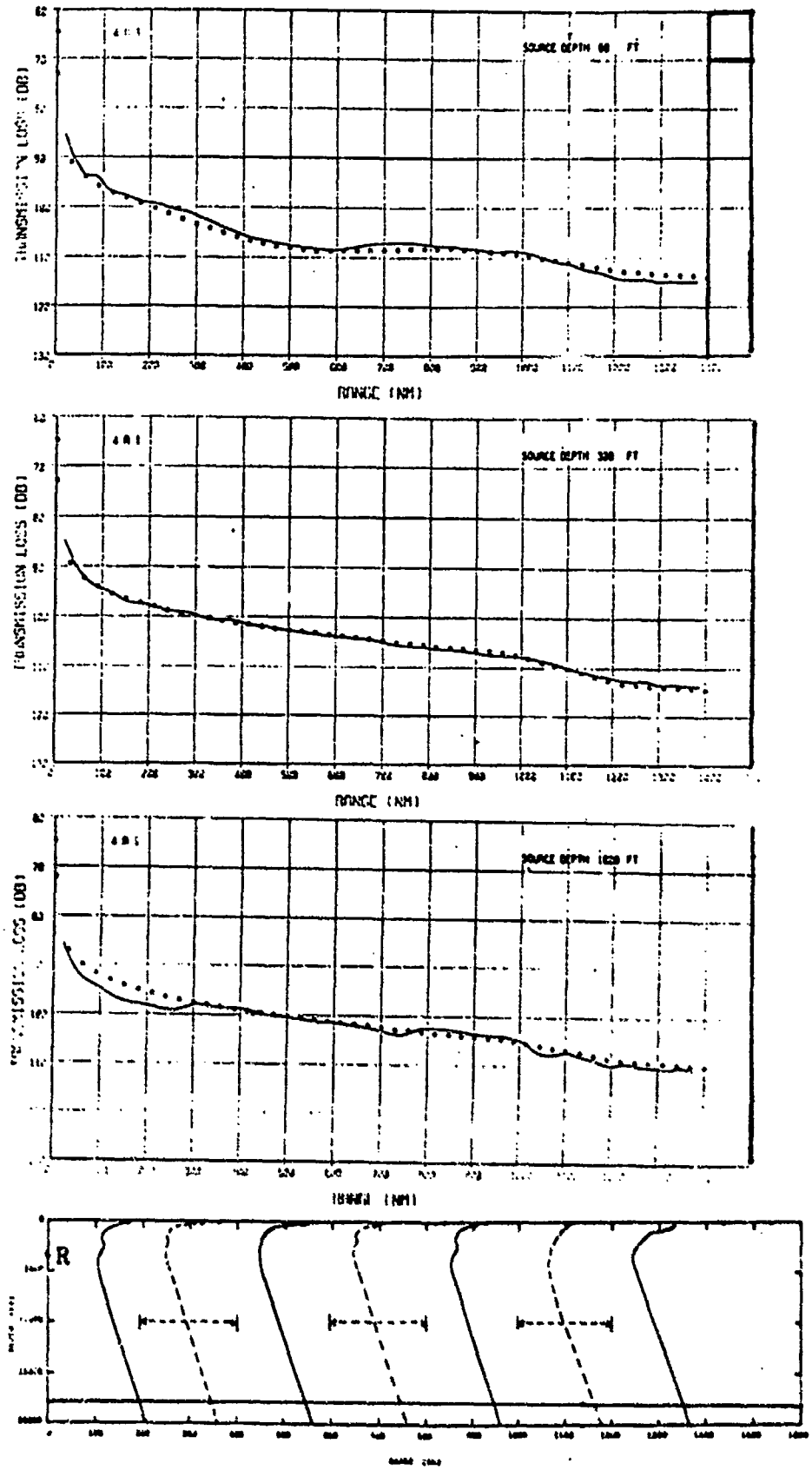

Figure 4-38 Comparison of Range-Smoothed Propagation Loss Versus Range for Test Case 4A1 (4000-ft Receiver-R) for Frequency of 128 Hz. Model (■), PE(—).

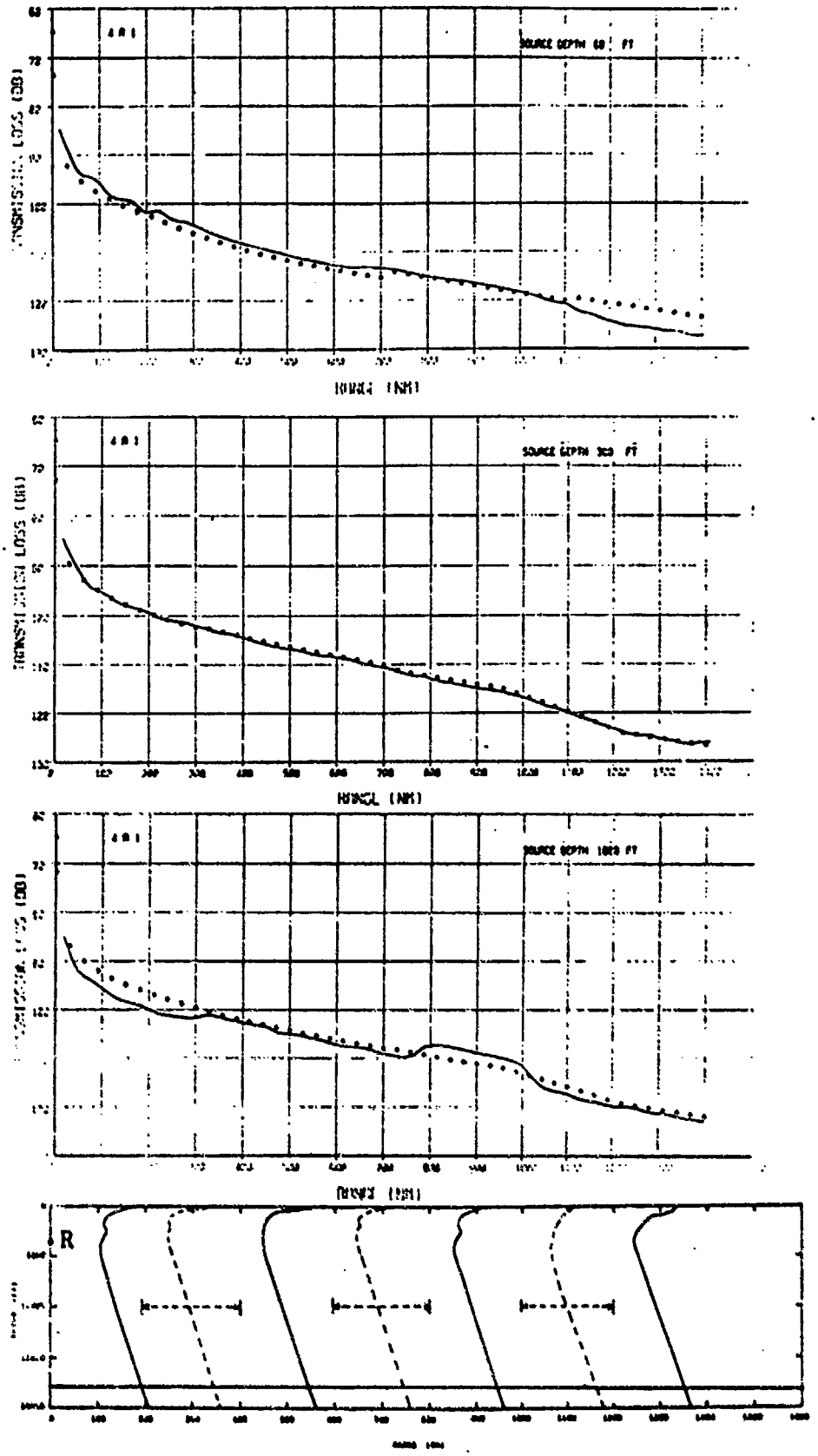

Figure 4-39 Comparison of Range-Smoothed Propagation Loss Versus Range for Test Case 4A1 (4000-ft Receiver-R) for Frequency of 256 Hz. Model (■), PE(—).

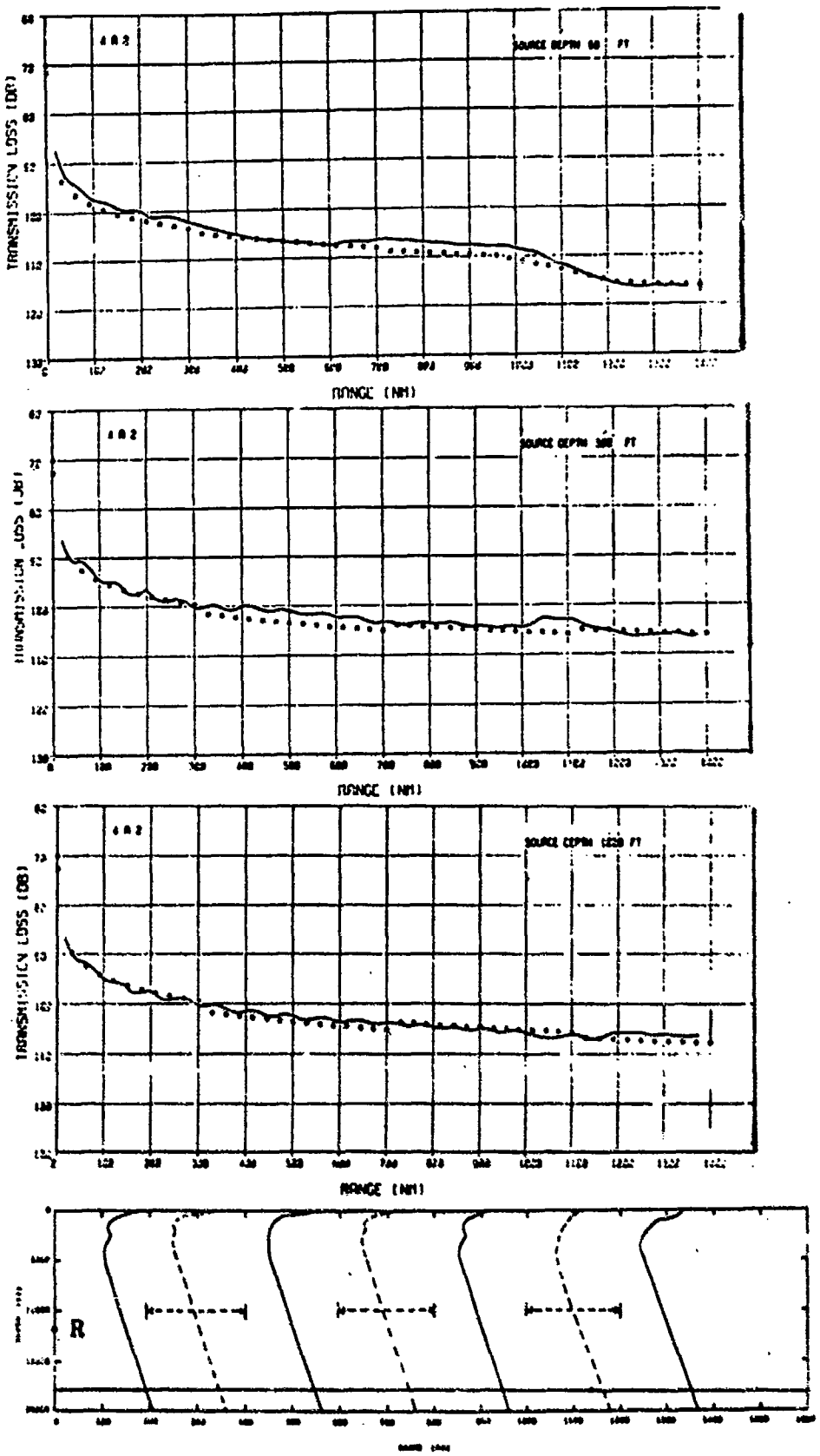

Figure 4-40 Comparison of Range-Smoothed Propagation Loss Versus Range for Test Case 4A2 (12000-ft Receiver-R) for Frequency of 64 Hz. Model (■), PE(—).

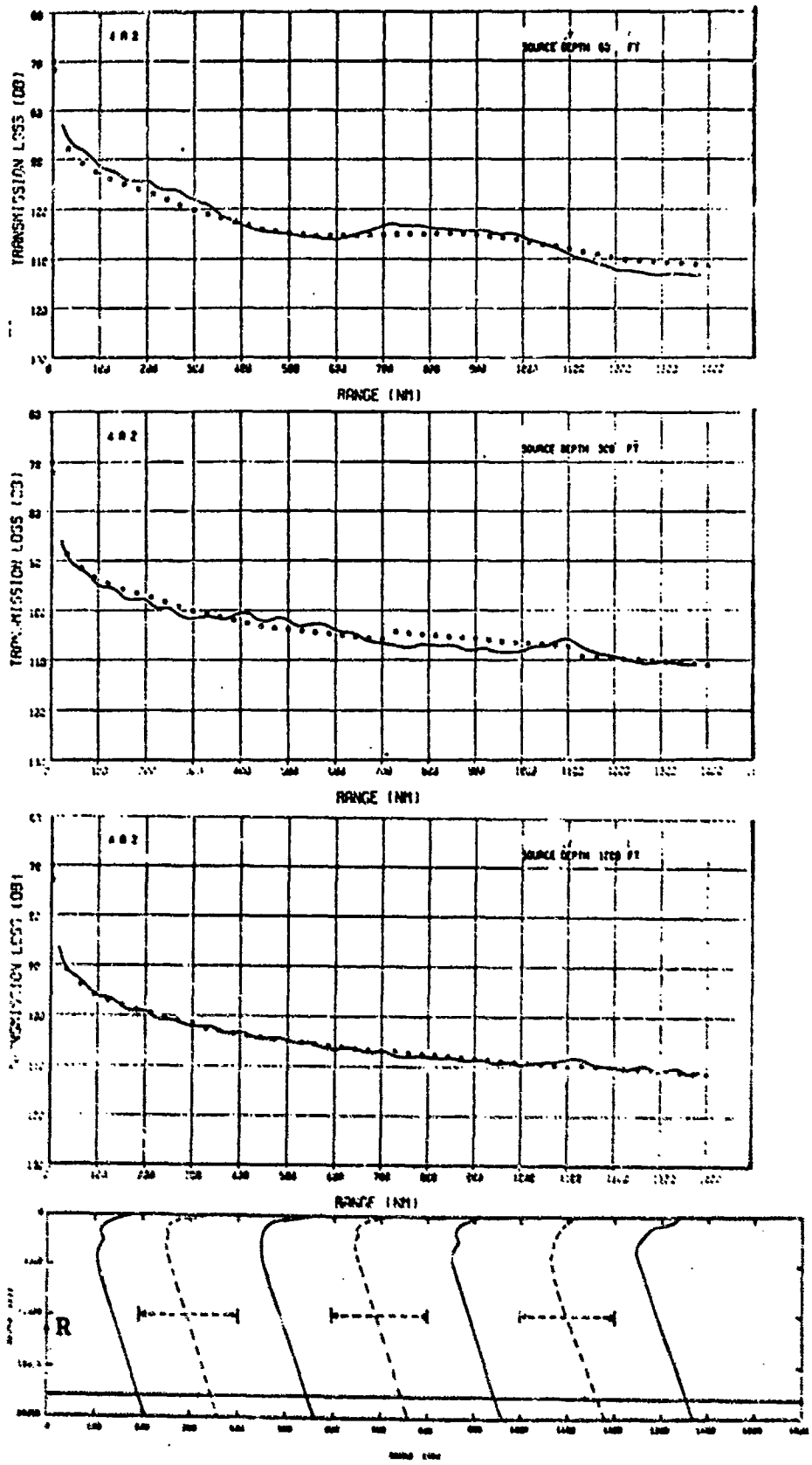

Figure 4-41 Comparison of Range-Smoothed Propagation Loss Versus Range for Test Case 4A2 (12000-ft Receiver-R) for Frequency of 128 Hz. Model (■), PE(—).

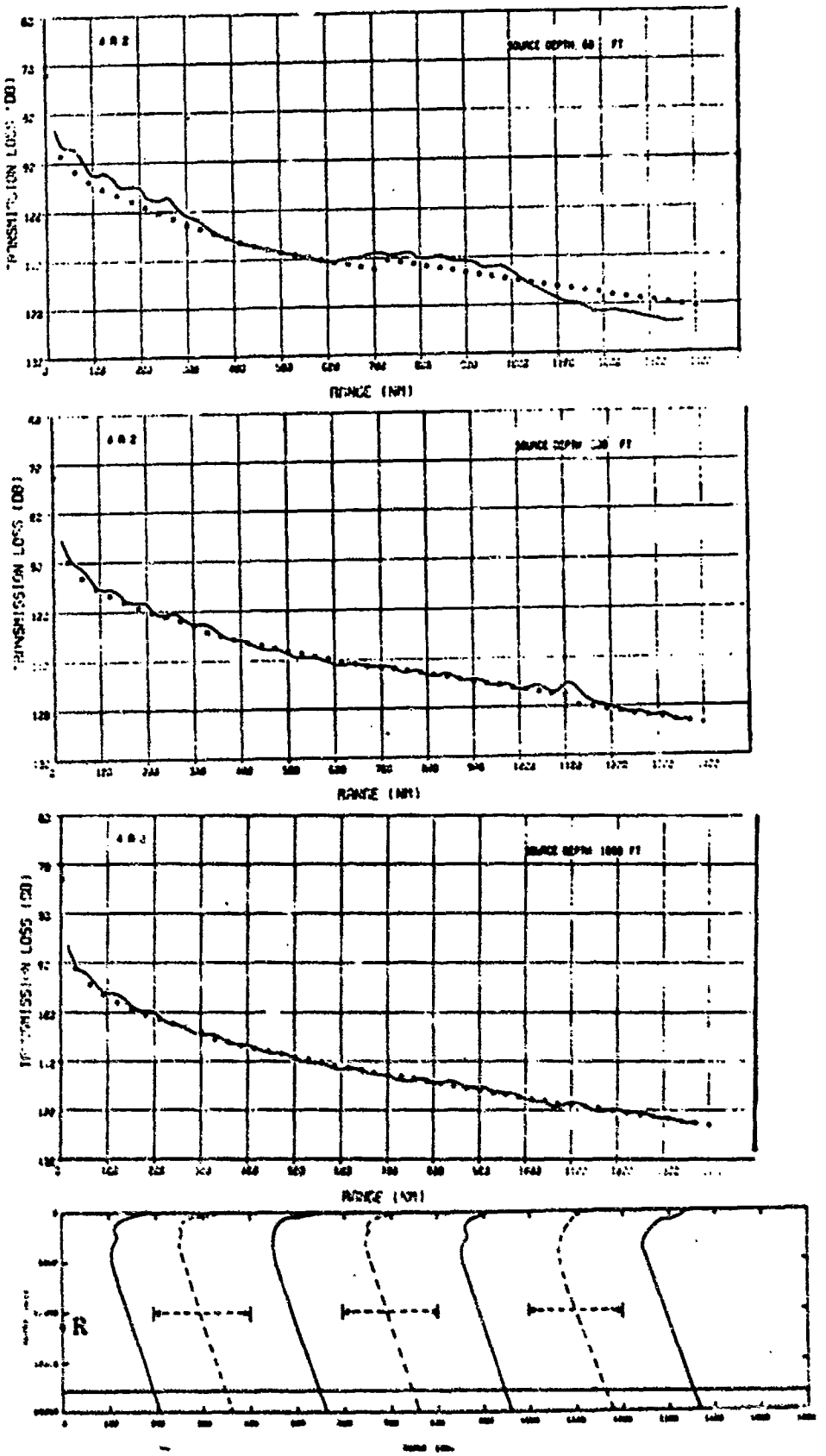

Figure 4-42 Comparison of Range-Smoothed Propagation Loss Versus Range for Test Case 4A2 (12000-ft Receiver-R) for Frequency of 256 Hz. Model (■), PE(—).

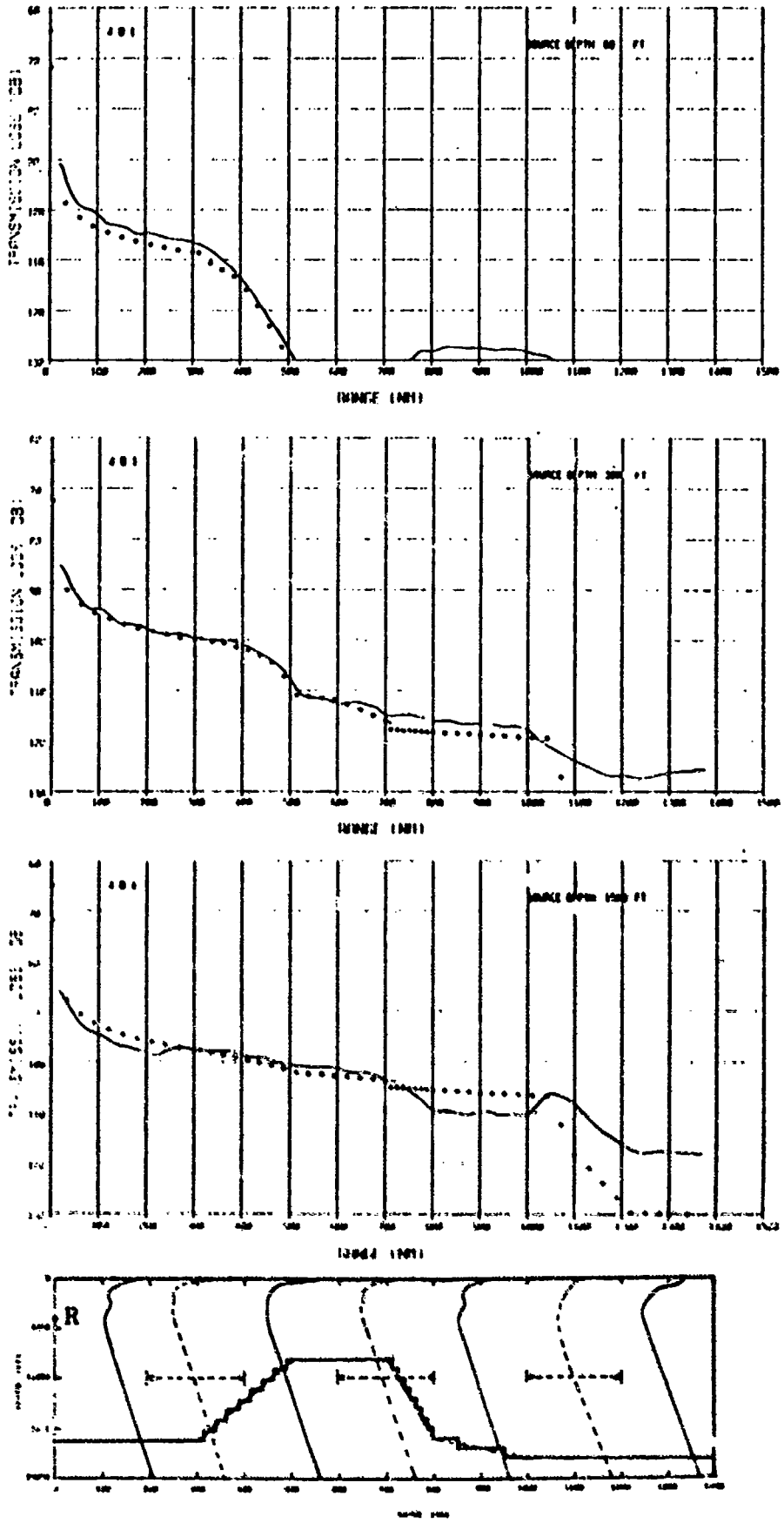

Figure 4-43 Comparison of Range-Smoothed Propagation Loss Versus Range for Test Case 4D1 (4000-ft Receiver-R) for Frequency of 64 Hz. Model (■), PE(—).

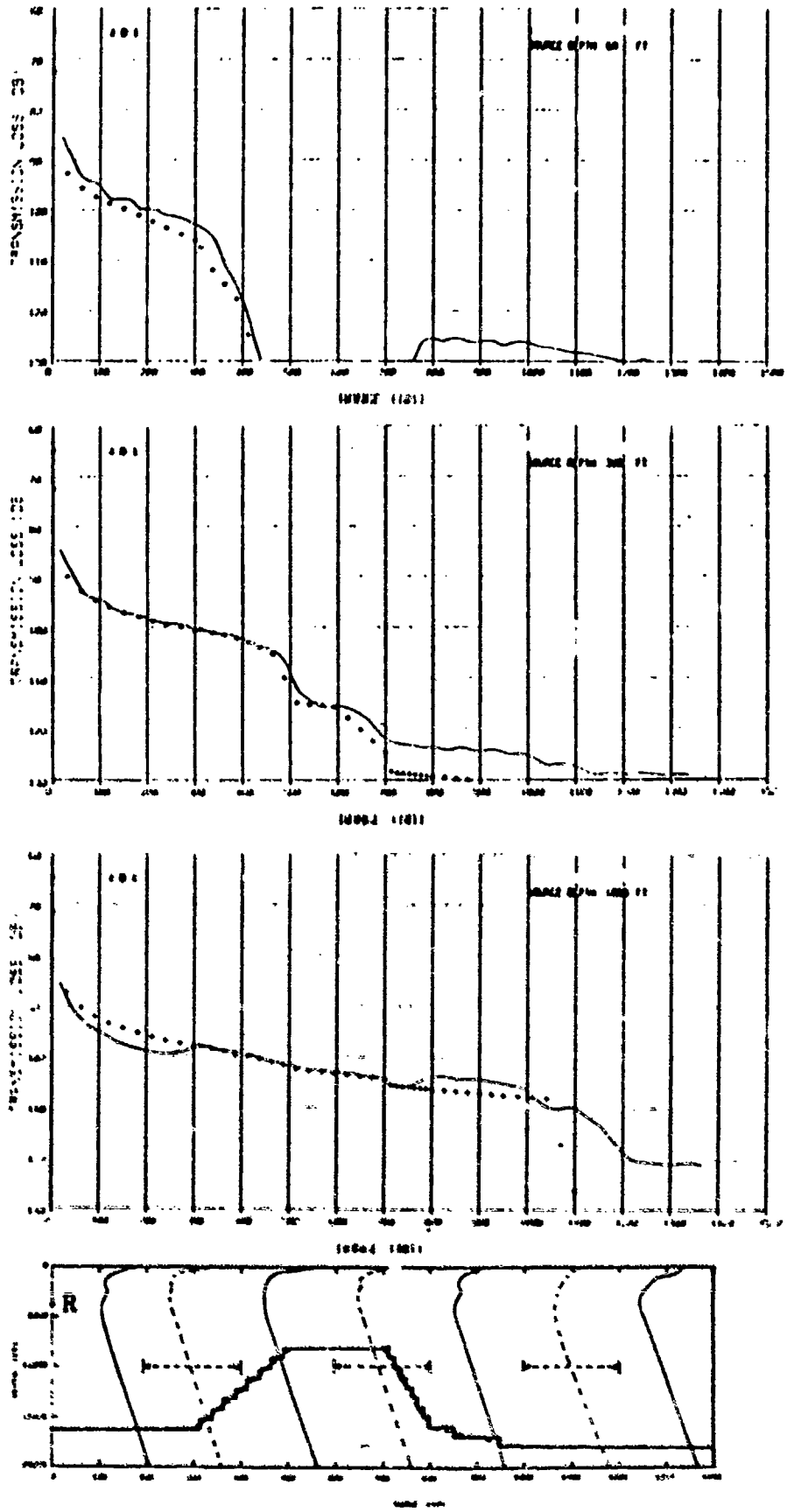

Figure 4-44 Comparison of Range-Smoothed Propagation Loss Versus Range for Test Case 4D1 (4000-ft Reciever-R) for Frequency of 128 Hz. Model (■), PE(—).

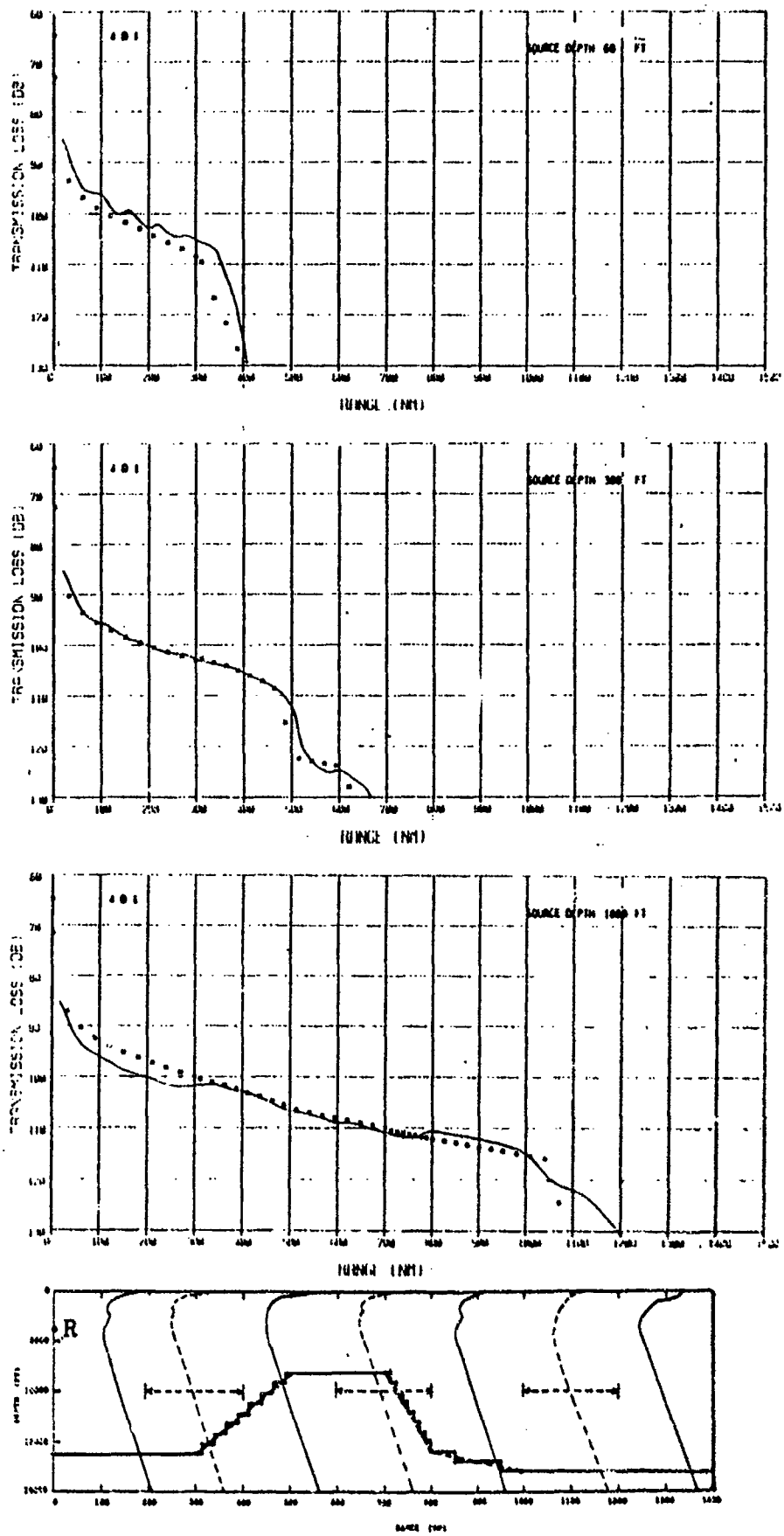

Figure 4-45 Comparison of Range-Smoothed Propagation Loss Versus Range for Test Case 4D1 (4000-ft Receiver-R) for Frequency of 256 Hz. Model (■), PE(—).

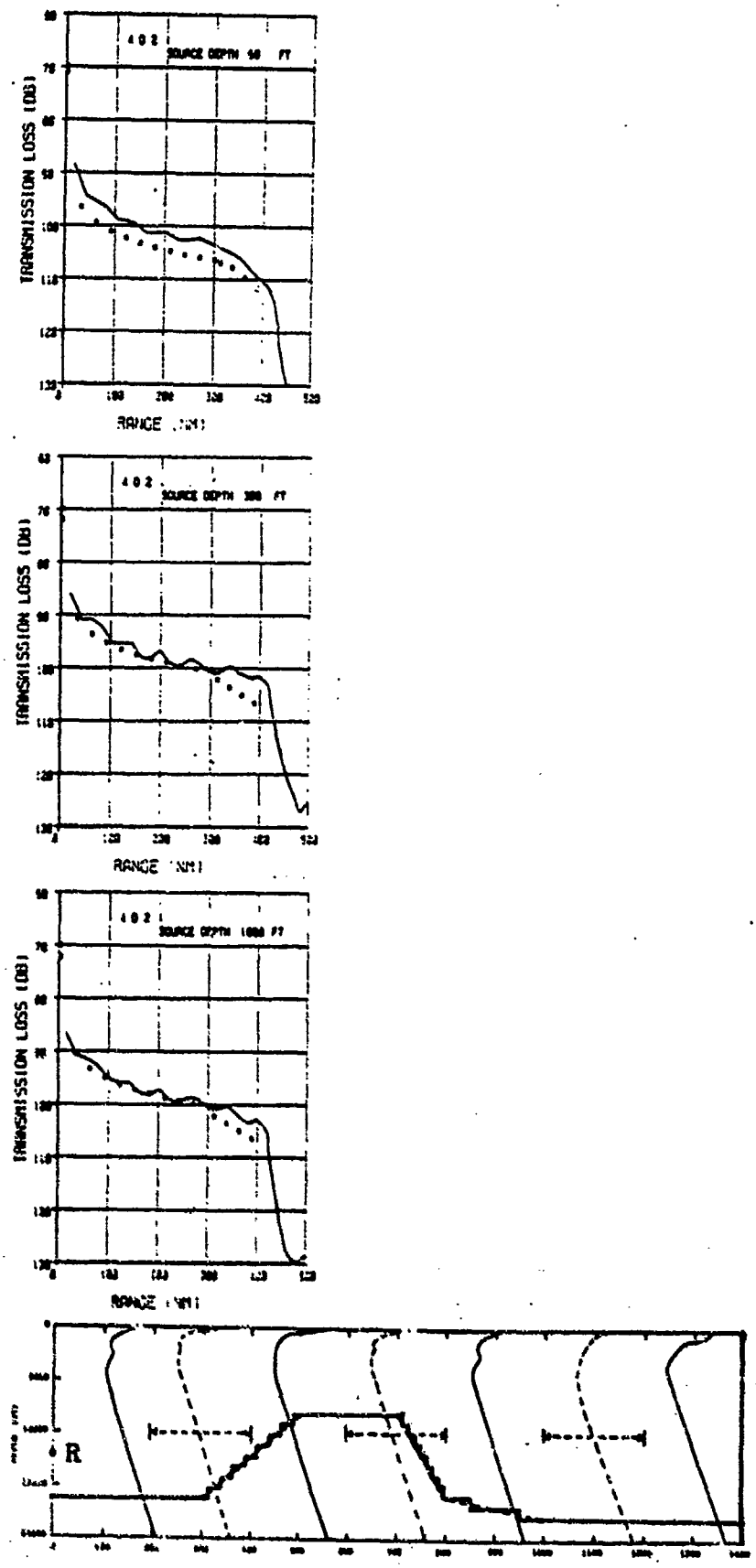

Figure 4-46 Comparison of Range-Smoothed Propagation Loss Versus Range for Test Case 4D2 (12000-ft Receiver-R) for Frequency of 64 Hz. Model (■), PE(—).

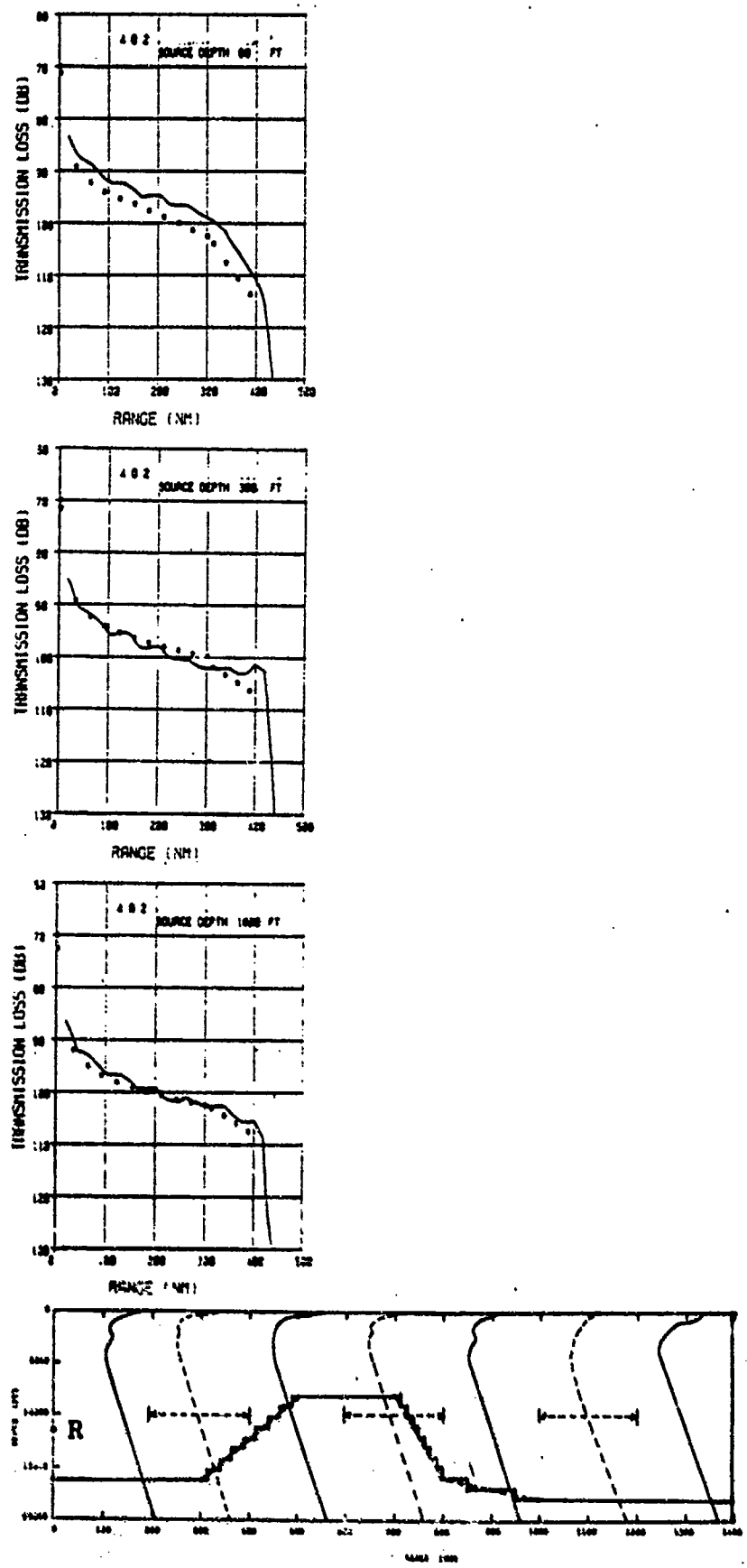

Figure 4-47 Comparison of Range-Smoothed Propagation Loss Versus Range for Test Case 4D2 (12000-ft Receiver-R) for Frequency of 128 Hz. Model(■), PE(—).

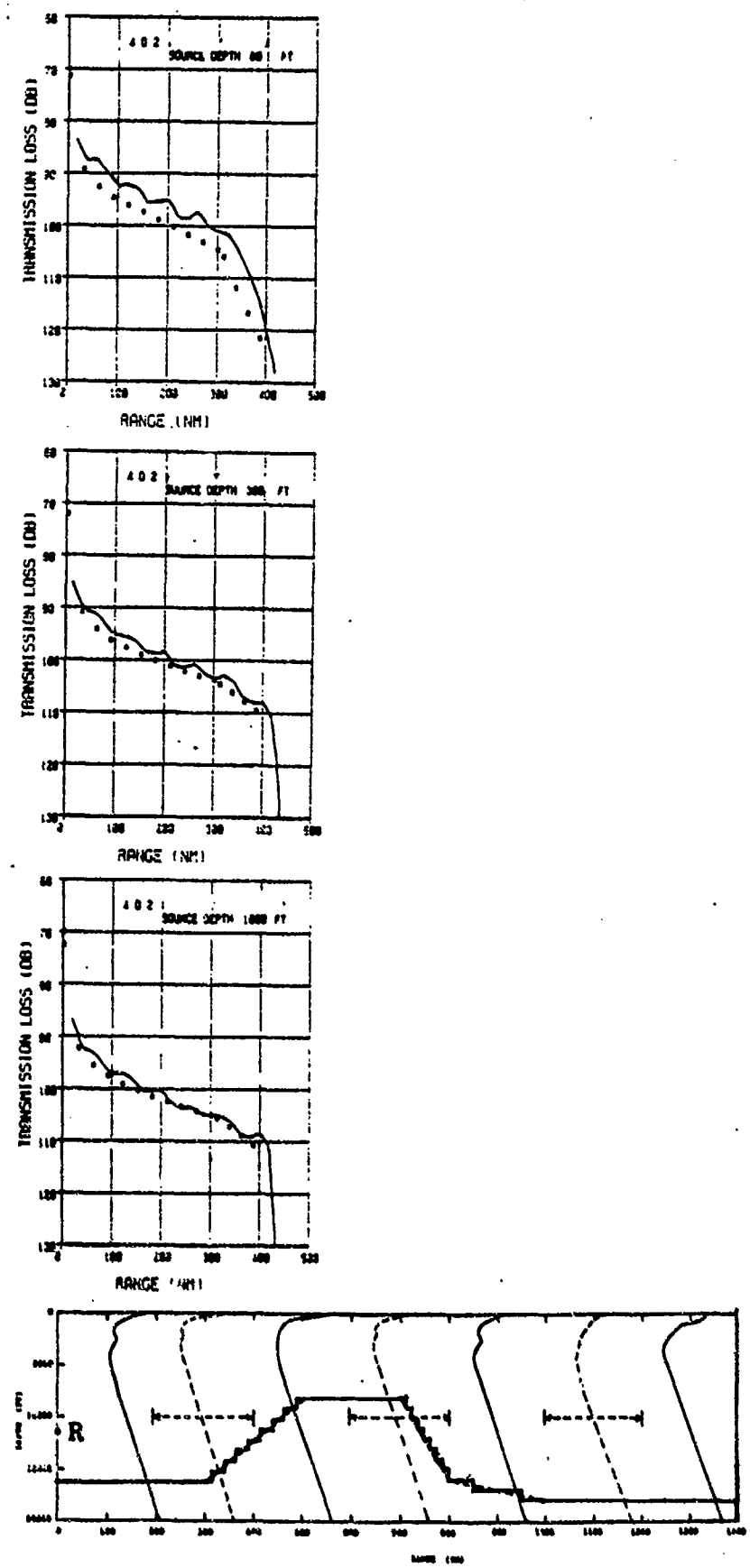

Figure 4-48 Comparison of Range-Smoothed Propagation Loss Versus Range for Test Case 4D2 (12000-ft Receiver-R) for Frequency of 256 Hz. Model (■), PE(___).

4.5 TEST CASE 5

The profiles in this environment evolve from cold northern water to a deep surface duct, to a Bermuda-like environment, to a double channel and finally to a very warm profile (see bottom of Figure 4-49). The only new profile in this case is the second, containing a 900-ft deep surface duct. In the continuous evolution for PE (from 100 to 400 nm) the profile develops an increasingly deep axis with an increasingly thick over-lying duct. When the duct reaches its full depth of 900 ft it is capable of supporting one trapped mode at 64 Hz, and proportionately more at the higher frequencies. This is effectively a double channel in which the model might be expected to have some difficulty.

4.5.1 Test Cases 5A1 and 5A2 - Flat Bottom, 500- and 2000-ft Receivers

64, 128 and 256 Hz Comparisons (Figures 4-49 through 4-54). Aside from the double channel problems encountered for the deep source at 1000 nm, for the 500-ft receiver some small discrepancies are apparent for the shallow sources in the surface duct. The duct appears to be shielding these sources from the receiver between 100 and 300 miles, decreasing the intensity in the duct while increasing it at the deep source when compared with the model (which includes no such shielding).

For the deep (2000-ft) receiver the effect appears to be reversed at the higher frequencies. An analysis of the PE output shows strong trapping by the developing duct between 150 and 600 miles. The apparent lack of such trapping relative to the shallow receiver suggests that the excitation of

these ducted modes is dependent on the evolution of the profile (and hence it is not adiabatic). In fact, the shallow-angle energy from the deep receiver is still fairly collimated as the duct develops and is effectively trapped as it reaches the surface near 150 nm. This effect is more dramatic in the following test case.

4.5.2 Test Cases 5C1 and 5C2 - Gradual Downslope, 500- and 2000-ft Receivers

64, 128 and 256 Hz Comparisons (Figures 4-55 through 4-60). By starting with a shallow bottom many of the high-angle modes are eliminated immediately. As the second profile evolves energy from the 500-ft receiver at 64 Hz (Figure 4-55) appears to be strongly shielded, first to the shallow sources but eventually for the deeper source as well. The high loss from 400 to 700 miles indicates no trapping by the duct at 64 Hz.

At 128 Hz (Figure 4-56) larger residual levels are shown for both shallow sources, however, at 256 Hz (Figure 4-57) there is less trapping. For the deeper receiver (Figures 4-58 through 4-60) much stronger trapping is seen at both 128 and 256 Hz.

The third profile encountered has a small sub-surface duct between 400 and 900 ft. The increase in level for the 1000-ft source at 128 Hz indicates a favorable duct to trap this frequency while leaking some energy to 1000 ft.

Finally, the recovery in level at 300 and 1000 ft as the axis rises is modeled fairly well. Shielding of these sources by the sub-surface maximum of the double channel profile (1000 to 1250 nm) accounts for the discrepancies in this region.

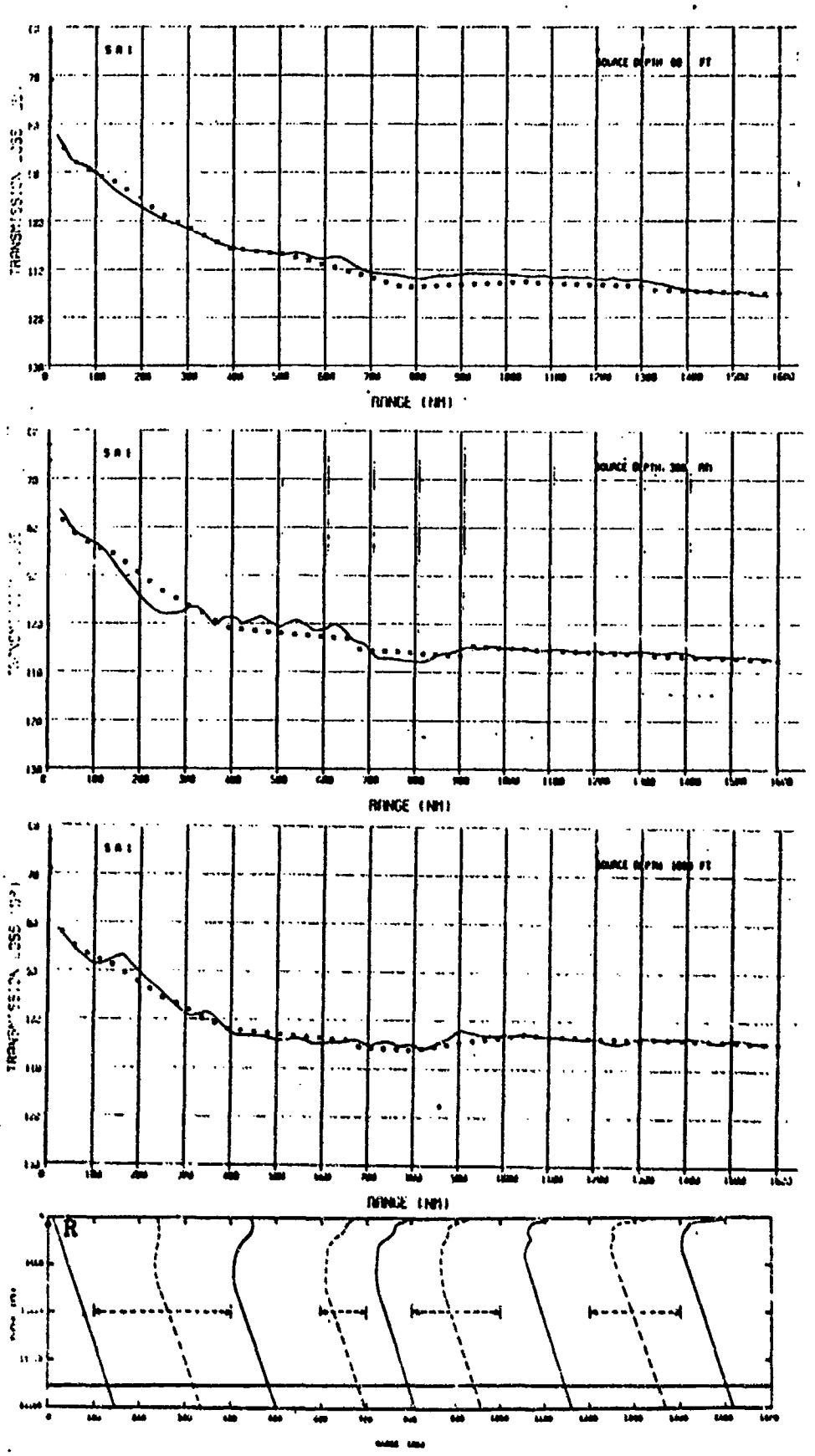

Figure 4-49 Comparison of Range-Smoothed Propagation Loss Versus Range for Test Case 5A1 (500-ft Receiver-R) for Frequency of 64 Hz. Model(■), PE(—).

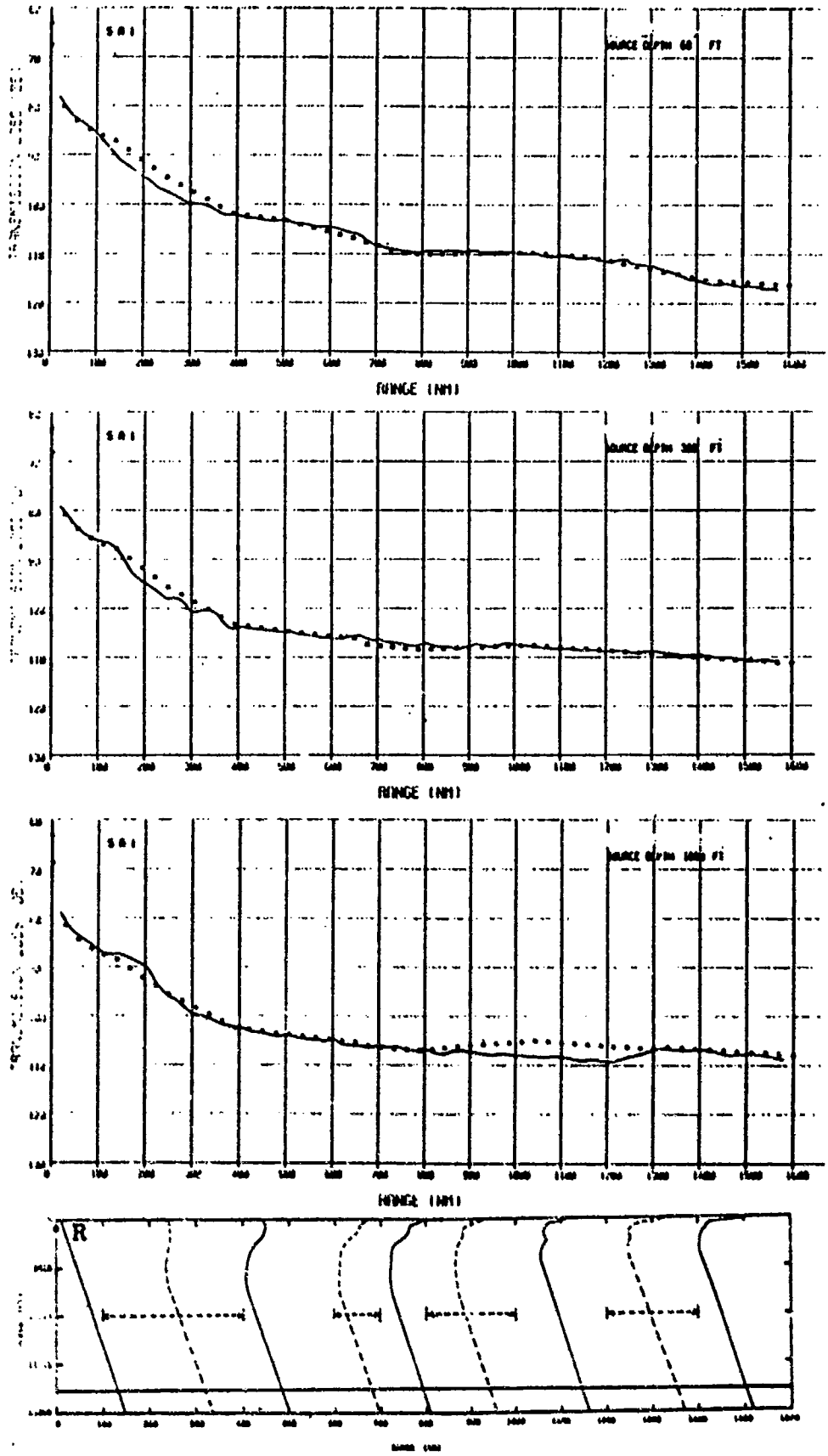

Figure 4-50 Comparison of Range-Smoothed Propagation Loss Versus Range for Test Case 5A1 (500-ft Receiver-R) for Frequency of 128 Hz. Model (■), PE(—).

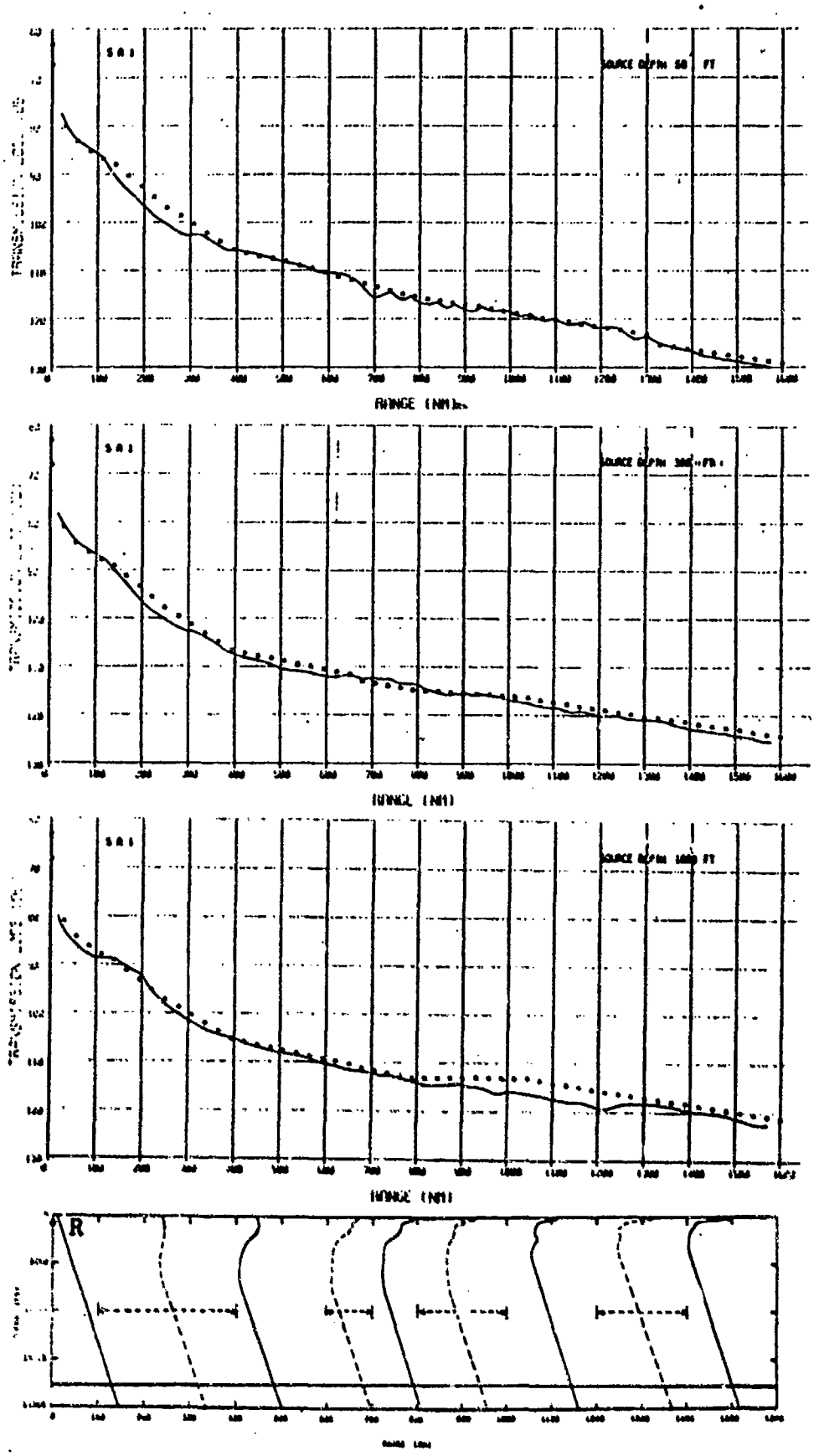

Figure 4-51 Comparison of Range-Smoothed Propagation Loss Versus Range for Test Case 5A1 (500-ft Receiver-R) for Frequency of 256 Hz. Model(■), PE(—).

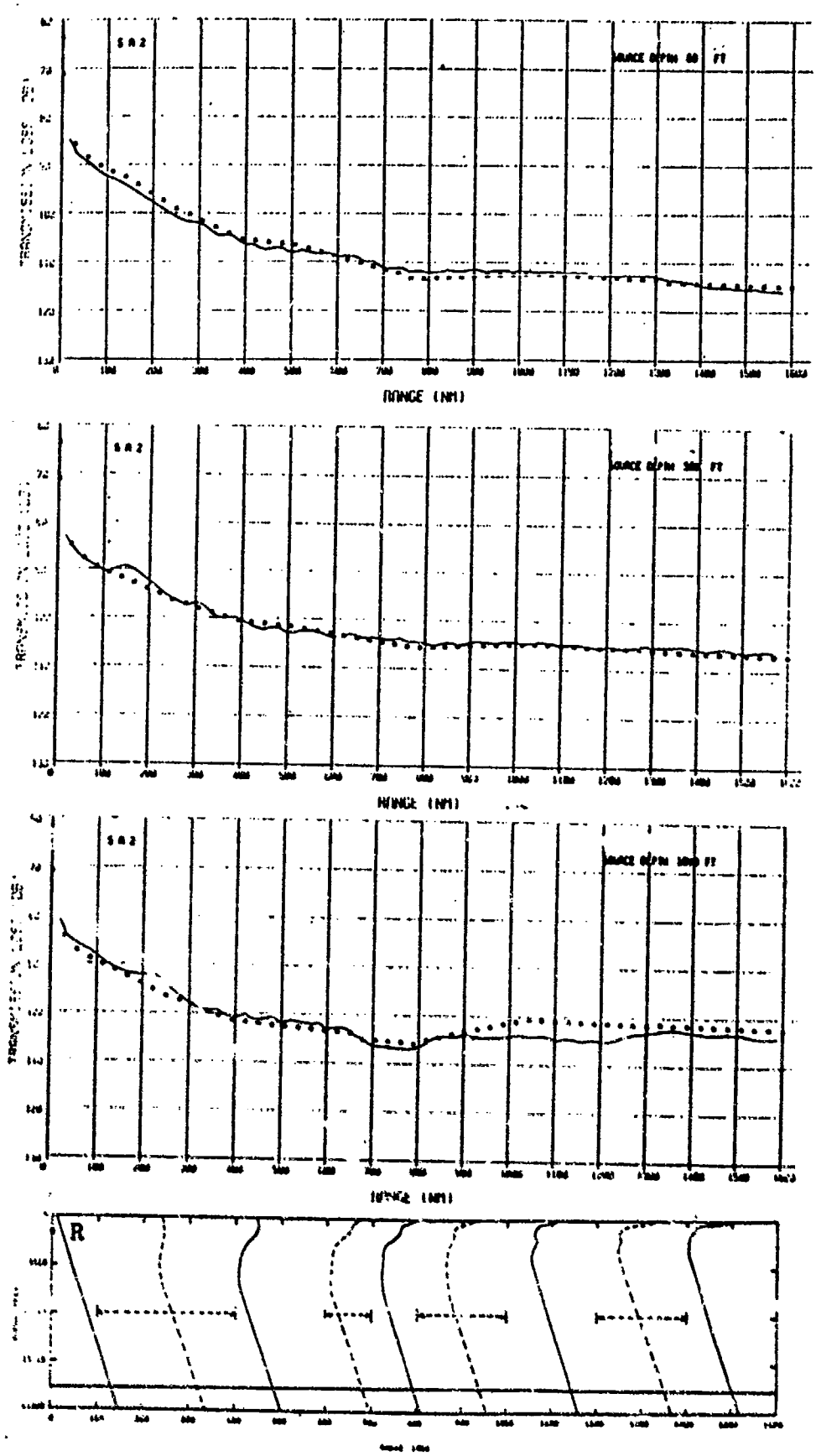

Figure 4-52 Comparison of Range-Smoothed Propagation Loss Versus Range for Test Case 5A2 (2000-ft Receiver-R) for Frequency of 64 Hz. Model(■), PE(—).

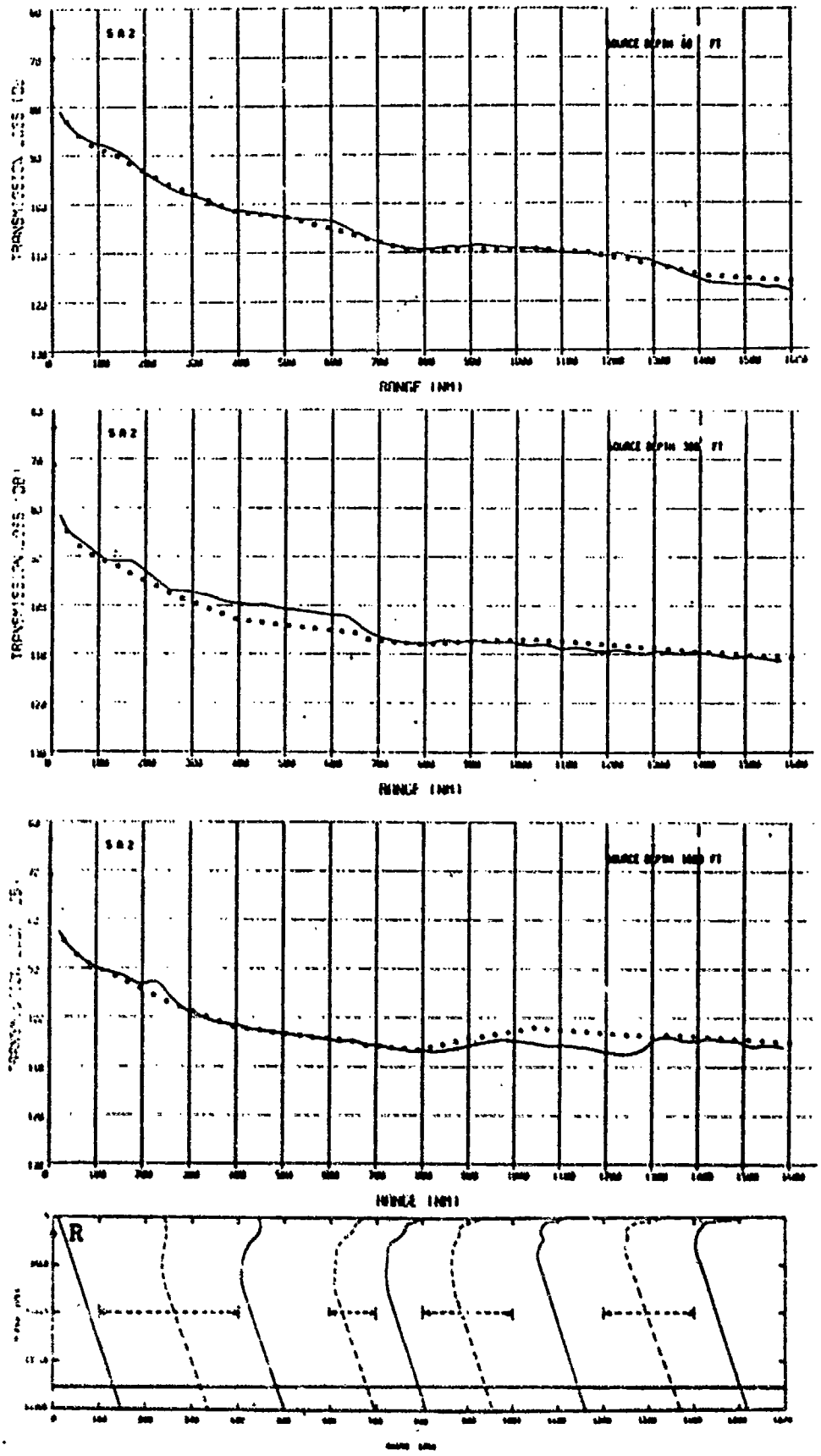

Figure 4-53 Comparison of Range-Smoothed Propagation Loss Versus Range for Test Case 5A2 (2000-ft Receiver-R) for Frequency of 128 Hz. Model(■), PE(—).

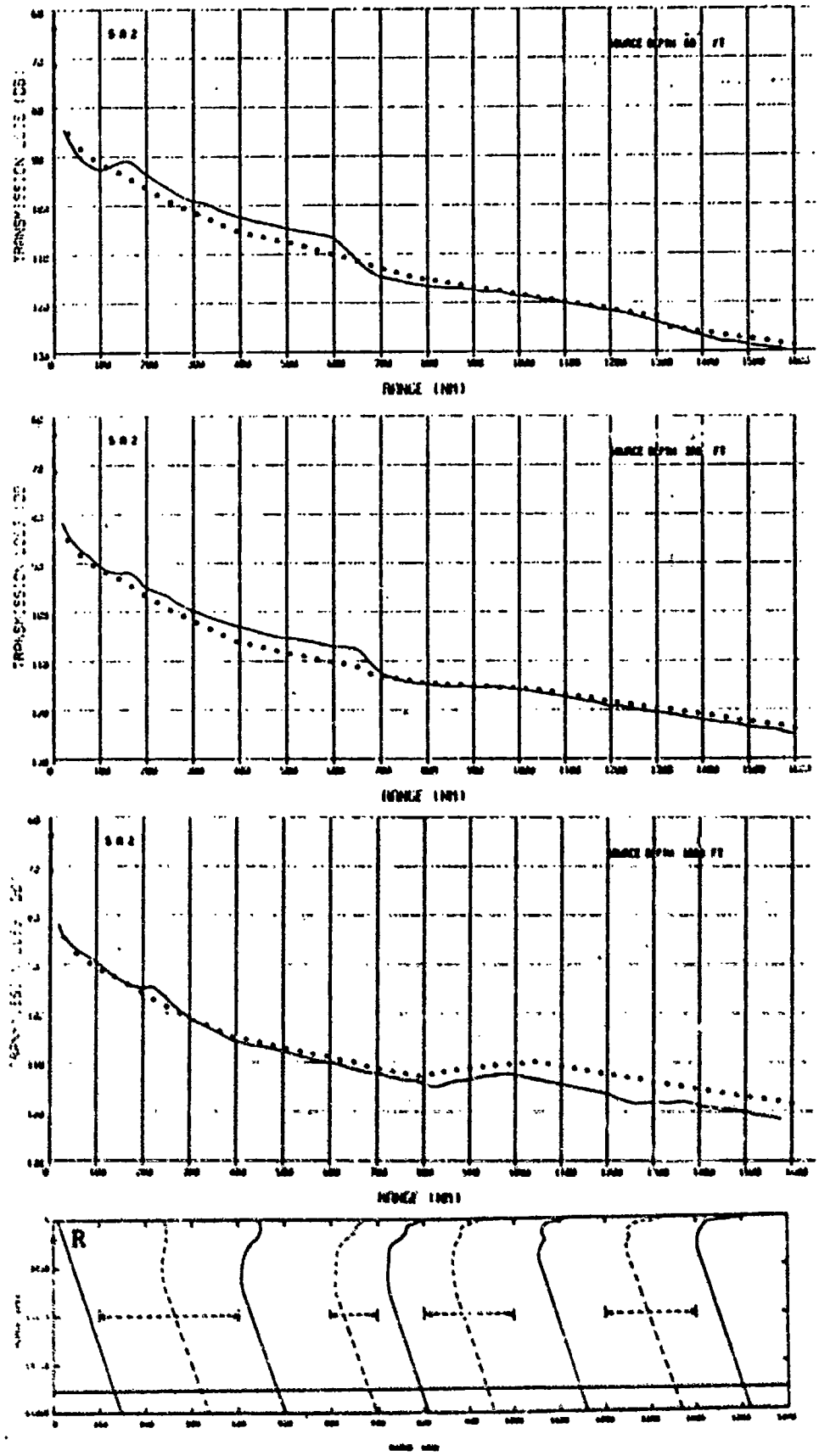

Figure 4-54 Comparison of Range-Smoothed Propagation Loss Versus Range for Test Case 5A2 (2000-ft Receiver-R) for Frequency of 256 Hz. Model(■), PE(—).

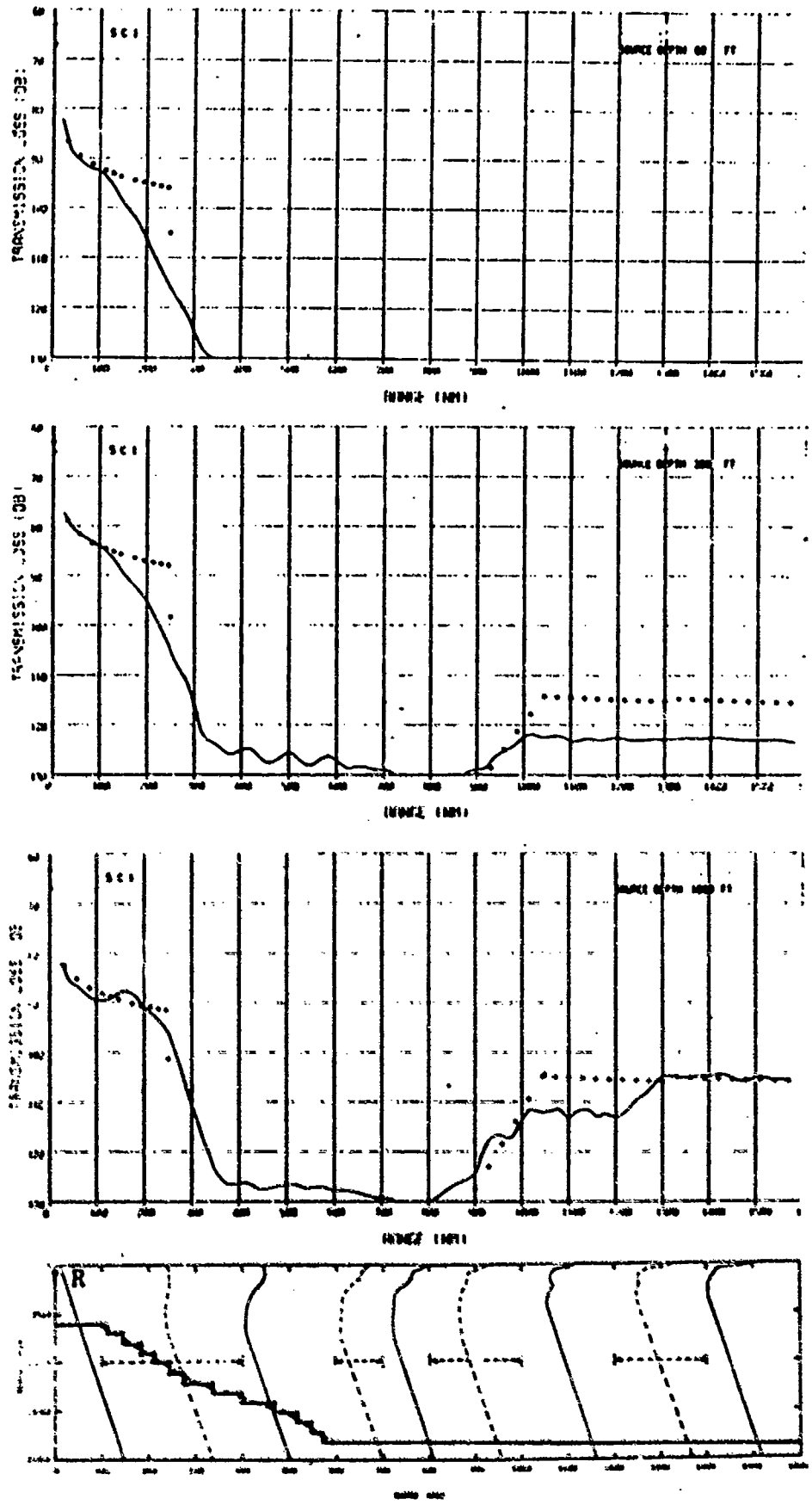

Figure 4-55 Comparison of Range-Smoothed Propagation Loss Versus Range for Test Case 5C1 (500-ft Receiver-R) for Frequency of 64 Hz. Model (■), PE(__).

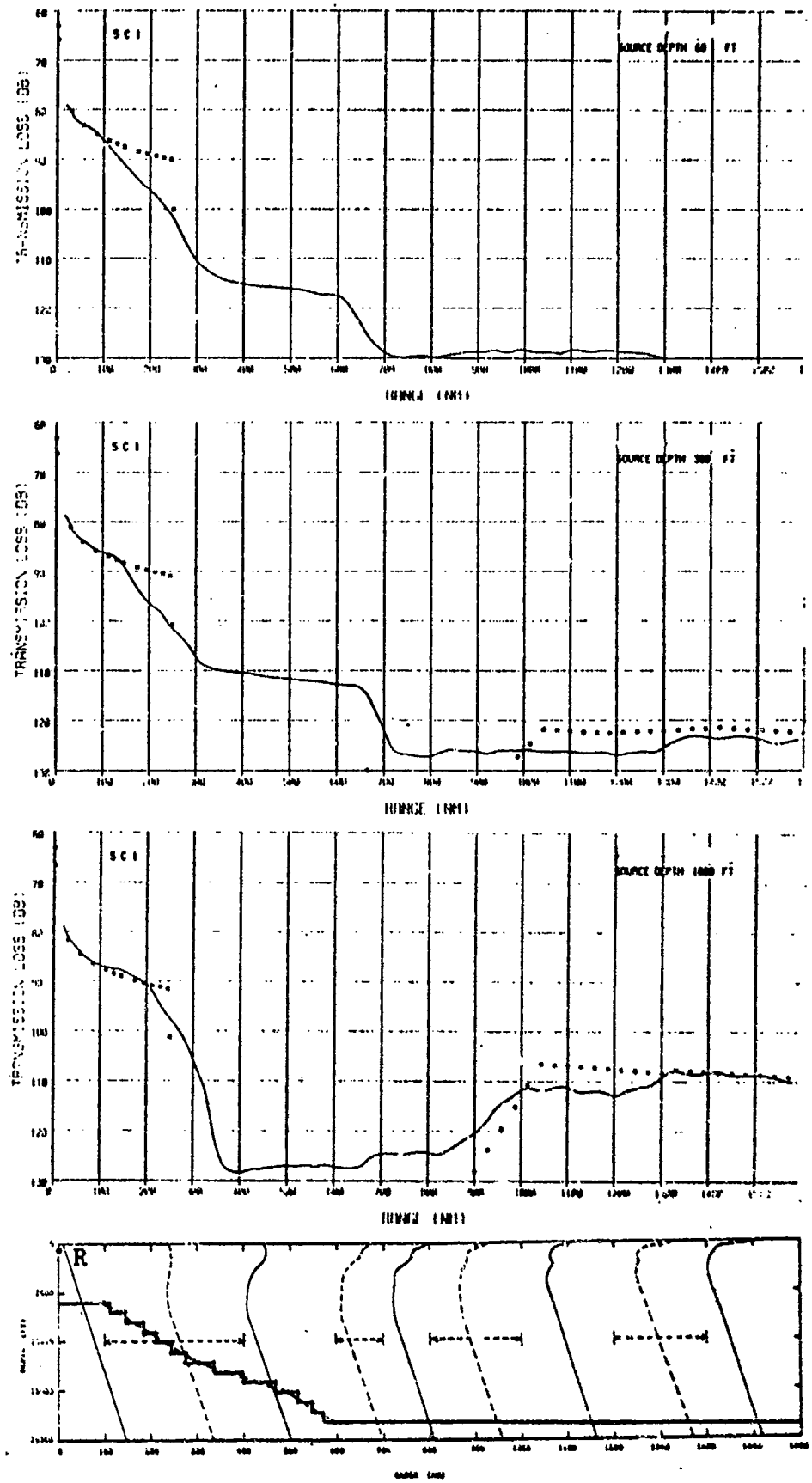

Figure 4-56 Comparison of Range-Smoothed Propagation Loss Versus Range for Test Case 5C1 (500-ft Receiver-R) for Frequency of 128 Hz. Model(■), PE(—).

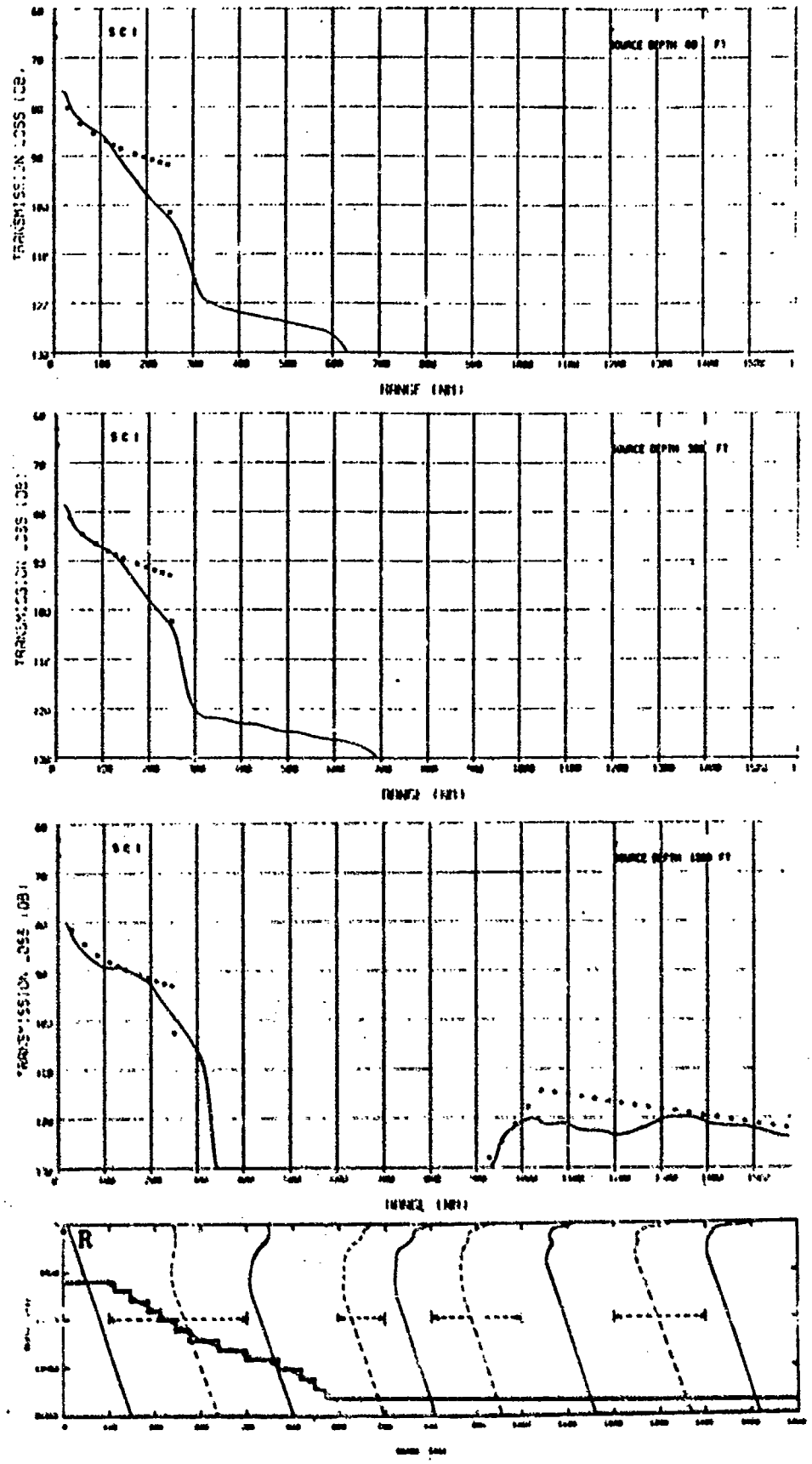

Figure 4-57 Comparison of Range-Smoothed Propagation Loss Versus Range for Test Case 5C1 (500-ft Receiver-R) for Frequency of 256 Hz. Model(■), PE(—).

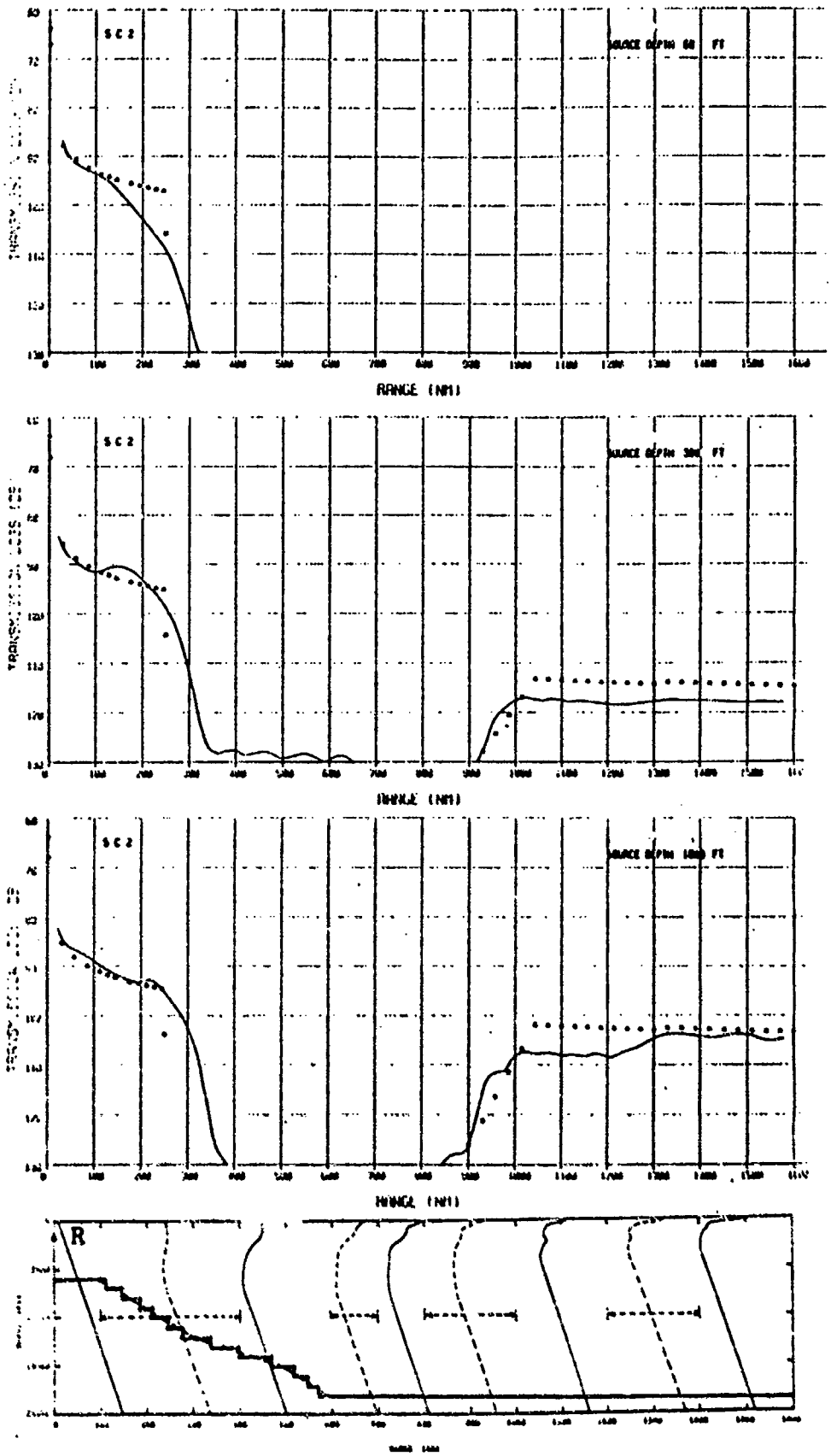

Figure 4-58 Comparison of Range-Smoothed Propagation Loss Versus Range for Test Case 5C2 (2000-ft Receiver-R) for Frequency of 64 Hz. Model (■), PE(—).

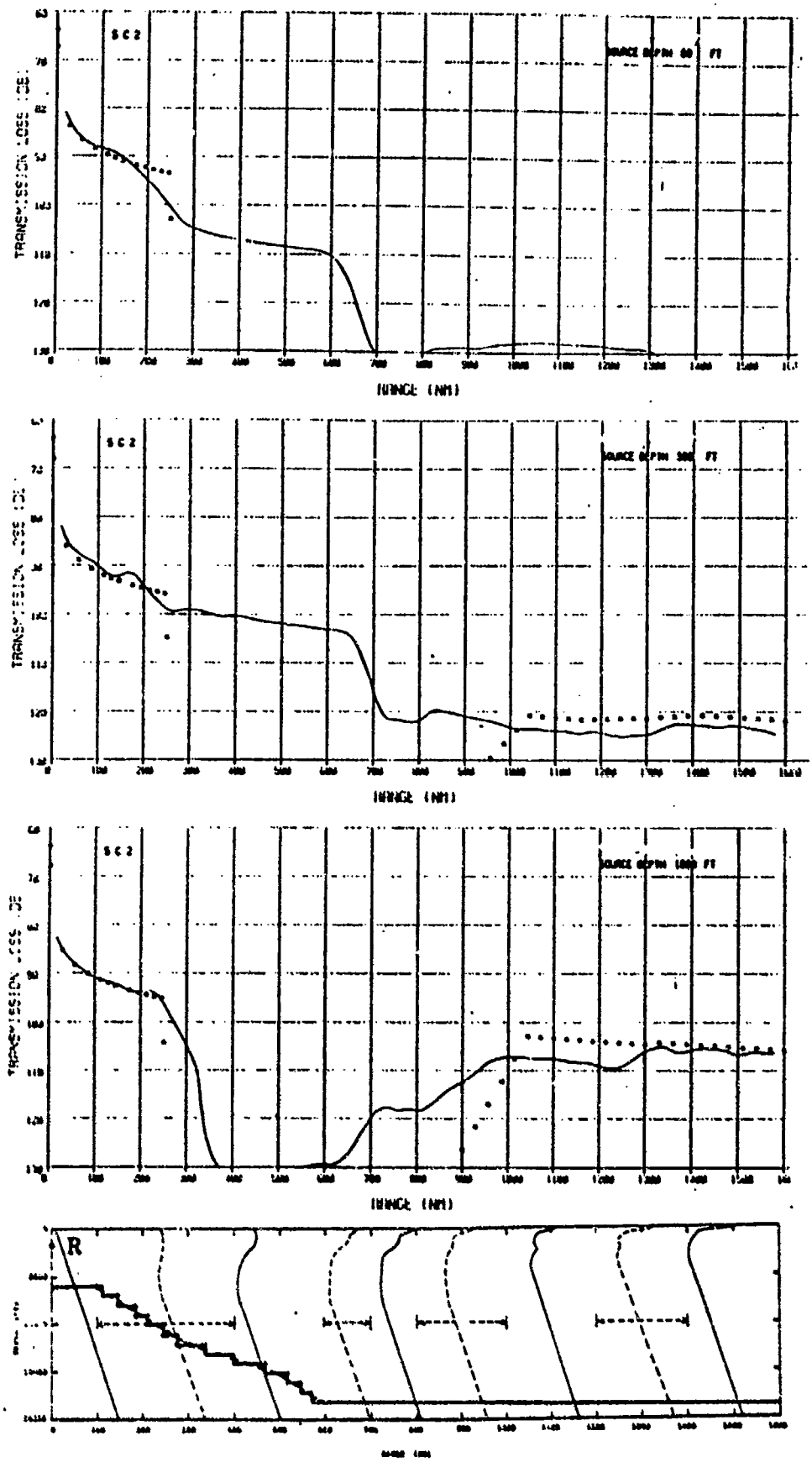

Figure 4-59 Comparison of Range-Smoothed Propagation Loss Versus Range for Test Case 5C2 (2000-ft Receiver-R) for Frequency of 128 Hz. Model(■), PE(—).

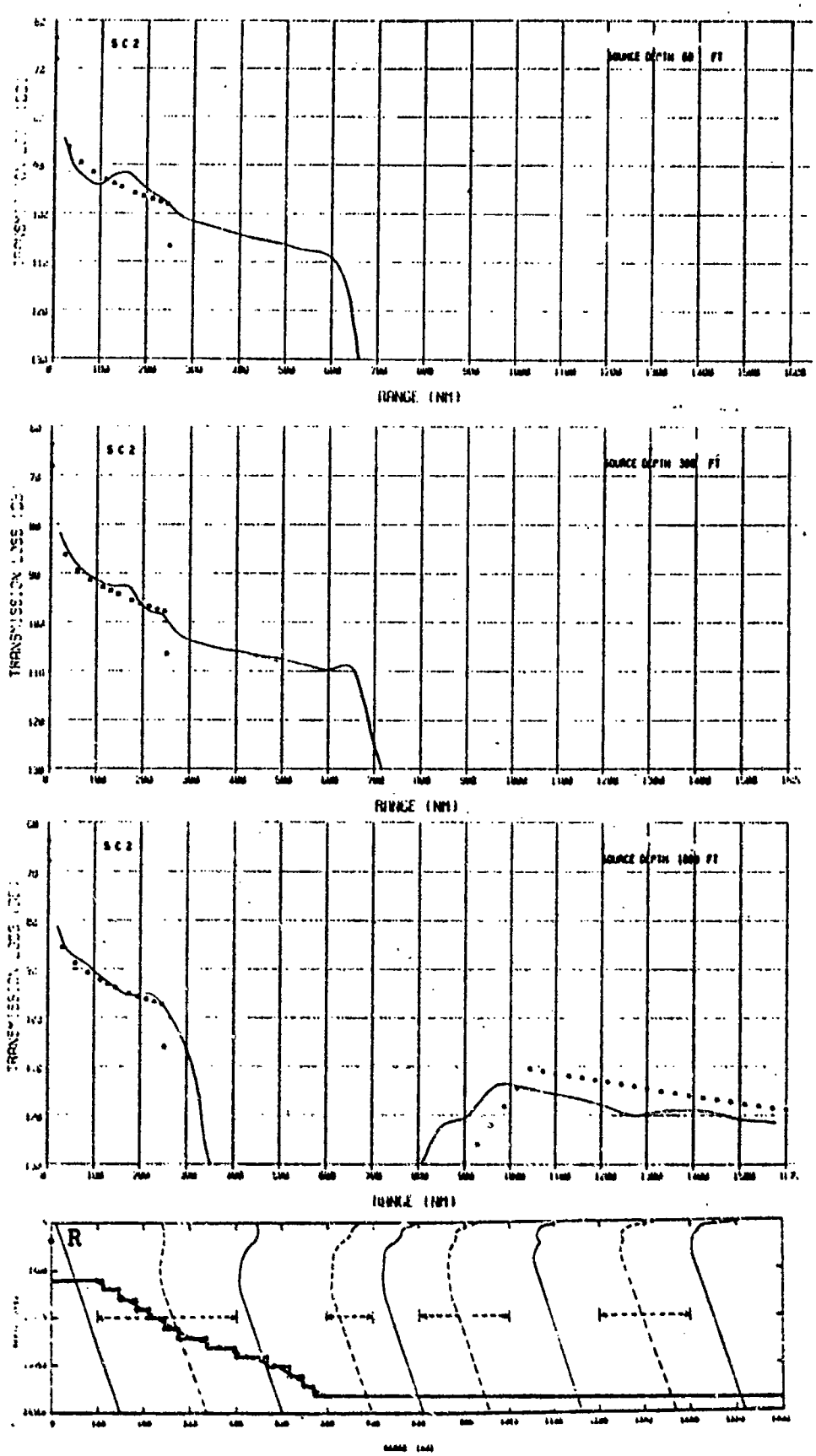

Figure 4-60 Comparison of Range-Smoothed Propagation Loss Versus Range for Test Case 5C2 (2000-ft Receiver-R) for Frequency of 256 Hz. Model(■), PE(—).

4.6 SUMMARY OF IDENTIFIED MODEL DEFICIENCIES

As a result of these comparisons, a number of model deficiencies (recognized in the basic design) have been identified and quantitatively evaluated. Remedies for each of them represent major modifications to the model. Most could be remedied within the model's conceptual framework (i.e., assumed adiabatic invariance). A few suggest real conceptual limitations. The following subsections discuss the specific deficiencies encountered. The final subsection translates these limitations into specific environments/geometries where problems might be encountered. The presence of a low-loss bottom (rather than the high-loss bottom assumed in these comparisons) would nearly always act to reduce the magnitude of the differences.

4.6.1 Angular Discretization

Because a small number of discrete modes are used, and each is assigned all of the energy in the angular band shallower than it, certain discrepancies are possible when there are only a few propagating modes. Especially noticeable is the effect to a shallow source when a 1° aperture of RR energy is assigned to an RSR mode which experiences strong destructive surface-image interference. When a mode is just barely stripped by the bottom all of the energy in its band (at shallower angles) is considered lost. If these angles dominate the field (usually through diffraction leakage) at some greater range, large errors are possible.

In general the discretization problem could be most severe when there are a few propagating modes. The worst environments will be those with marginal depth excess for the receiver and little or none for the source. Because there are only a few modes possible, the error will occur for relatively high values of transmission loss (typically greater than 100 dB).

4.6.2 Receiver Coupling to Diffraction Fields of Modes

While the present treatment considers source coupling to modes through their diffraction fields, modes can only be excited by the receiver if it is contained between their turning points. In a true normal-mode representation for the field, the receiver couples to modes through diffraction fields just as the source does. This is rarely a problem. However, if all paths reaching the receiver become bottom limited over a high-loss bottom the total loss may become so high that such diffraction-coupled modes would dominate. Since these fields are generally quite weak the problem will be most noticeable when the propagation loss is already quite large.

4.6.3 Coherent Effects at the Receiver

All up- and down-going paths (or modes) are summed incoherently (i.e. random phase) at the receiver. This may cause discrepancies (typically up to 3 dB) when the field is dominated by a narrow band of paths which have a small phase difference at the receiver. In range-independent environments where the source and receiver are at the same depth (i.e. a "cusped-caustic" geometry in ray terms) the dominant paths tend to be in phase at the receiver and the level will be underestimated by 3 dB.

For shallow receivers, surface-image interference effects may be quite noticeable. Also for deep receivers when only a few RSR modes are present the spread in phase differences across the aperture may be small enough to cause a net constructive or destructive interference. This requires a very small angular aperture, usually associated with marginal depth excess for the propogating modes at some range of interest, coupled with a receiver well away from the sound-channel axis.

4.6.4 Extended Surface-Image Interference at the Source

The present treatment of surface-image interference for the source extends for each mode to the second rms phase point in depth. In cases where a narrow band of high-angle modes dominates the field, the phase differences across the band at the source depth may be sufficiently small to cause a net difference from incoherent summation.

A similar discrepancy might occur at sufficiently low frequencies and great depths that the straight-path approximation for the phase difference in depth breaks down. This problem would be more acute if the phased sum were extended deeper. Also such an extension would require consideration of the finite band of angles contributing to the mode rather than the interference properties of the single mode angle.

4.6.5 Surface-Image Interference on Refracted Modes

The present treatment extends the diffraction field to the image depth of the source and then subtracts it from the field at the actual source depth. This is equivalent

to assuming a constant gradient to the image depth and a precisely out of phase field. Even if the gradient were constant to the surface, the diffracted field to the image depth (replacing the surface by a mirrored environment) would be higher since the gradient would effectively decrease above the surface. More significantly, inspection of PE contours in near-surface RR shadow zones suggests that the phase difference is depth dependent and equals π only at the surface.

This limitation might be most noticeable in bottom-limited geometries where the only energy to a shallow source is via diffraction fields.

4.6.6 Improved Diffraction Fields

As mentioned above, the diffraction field of a mode is determined solely by the gradient at the mode turning point. If the gradient increases in the shadow zone the field will be weaker, and if it decreases the field will be stronger. No attempt is made to compute an average effective gradient to the source depth. Hence if the profile is modeled with a few segments and strong gradient discontinuities, the diffraction field might appear to change discontinuously for a small change in the mode turning point depth (due to a very small change in the profile, for example).

This problem will also be most noticeable in environments where the source couples only to diffraction fields.

4.6.7 Double-Channel Environments

This may be the most severe basic limitation of the model. Its present treatment of double (or multiple) channels including surface ducts is to define the outermost extremes of a mode in terms of its phase velocity, and treat the mode as propagating between these turning points. No exclusive propagation in one of the channels is permitted. Hence if the lower channel becomes bottom limited no ducting over the bottom in the upper channel is possible -- the mode is bottom reflected.

Also no shielding of a source from modal energy by a subsurface maximum is permitted. The eigenfunctions are limited to their caustic values through such interior shadow zones (rather than decaying and then recovering).

A proper treatment of this problem is most difficult, even when adiabatic invariance holds (cf. Smith (1974) for a ray treatment with no diffraction considerations). When a double channel develops from a single channel the adiabatic assumption may be limiting as well. This problem can be most severe in areas where the lower channel is bottom limited, however it can also lead to $\sim$ 3 dB errors when there is a large depth excess.

4.6.8 Asynchronous Changes in Bathymetry and Water Mass

The discretized treatment in range of the sound-speed profile can lead to substantial errors when the bathymetry changes substantially just before the water mass does. For example, a profile's rising critical depth is modeled discontinuously at the water-mass boundary. If

the rise had been accompanied by shoaling bathymetry (which was always deeper than the critical depth) the net actual effect might be small. If the water-mass boundary were not encountered until after the first region became bottom-limited the effect could be modeled as unrealistically large.

This effect will be most noticeable where significant changes in both bathymetry and water mass occur in the same area, but either the water mass change is under-resolved in space, or the change is in fact gradual. An example might be the rising sound-channel in the North Pacific near the Mendocino Fracture Zone. Clearly, one solution is better water-mass resolution, at least in areas where bathymetry might be critical.

4.6.9 Transmission-Loss Smoothing

The transmission-loss smoother has been designed to ease transition regions and does so by attempting to identify the source of large, abrupt changes in loss. If a change in bathymetry (which happens to be concurrent with a minor change in water mass) is the source, the water mass will be incorrectly identified and the change will be smoothed over too wide a region. Gradual smoothers operating on the individual modes (and their coupling) are feasible but by no means trivial. The problem is not generally severe since the effect is limited in range to no more than ± 150 miles.

4.6.10 Summary of Likely Problem Areas

Nearly all the deficiencies are most likely to become significant in large areas which are bottom limited (with a high-loss bottom) for one or more sources. When this environment includes a double channel or deep surface duct the problem may be acute. Without double channels, low frequencies may be most severely affected. With double channels the errors may be largest at high frequencies. Significant, nearly coincidental changes in water mass and bathymetry may cause additional problems.

4.7 STATISTICAL RESULTS

While the comparisons of the previous section are most helpful in identifying model weaknesses and limitations, they do not directly address the question of model accuracy. Assuming the definition of model error developed earlier,

$$\varepsilon_{MOD} = TL_{PE} - TL_{MOD}$$

the question concerns the properties of ε_{MOD}. In the following two subsections the distributional and statistical properties of ε_{MOD} are respectively established.

4.7.1 Distribution Functions for Model Error

The model error for any one of the 180 cases shown in Section 4.5 can be estimated by inspection of the comparison plots. The purpose of this section is to summarize the distribution of the differences across all cases as a function of three parameters: source depth, frequency, and Figure-of-Merit (FOM) range. For example: The distribution of ε_{MOD} for all values of PE-predicted transmission loss (FOM) between 90 and 100 dB for 64 Hz and 60-ft source depth.

The specific distribution functions developed correspond to each source-depth/frequency combination for four FOM ranges: 90-100 dB, 100-110 dB, 90-110 dB and all values. In addition, for these FOM ranges summaries for each source depth and all frequencies, and each frequency and all source depths are developed. Finally for these FOM ranges as well as FOM's less than 90 dB and FOM's greater than 110 dB the distributions across all source depths and frequencies are presented. The extreme low and high FOM

ranges represent only 10% and 2% of the data and a further breakdown for specific source depths and frequencies would contain insufficient data to be meaningful.

The 16 distribution functions (3 source depths × 3 frequencies, plus 6 summaries (for each source depth and frequency), plus overall summary) are displayed on one figure for each of the four FOM ranges. They have been discretized in 2 dB bins and represent the fraction of points in each bin for the case being displayed. The number of samples (N) is also indicated. Each case is discussed below with all figures consolidated at the end of this subsection. The statistical properties of the distributions are summarized in Section 4.7.2.

90-110 dB FOM Range (Figure 4-61)

The rows of distribution functions in each figure correspond to indicated source depths (60, 300, 1000 ft and all depths) and the columns correspond to indicated frequencies (64, 128, 256 Hz, and all frequencies). In this FOM range there is a slight tendency for the model to overestimate the loss (negative ε_{MOD}). The tendency is most pronounced for 256 Hz at 60 ft and 128 Hz at 300 ft. In these cases the sources are a sufficient number of wavelengths below the surface to usually be treated incoherently, whereas they are close enough to the surface for the proper coherent summation to result in a mean net effect.

These low FOM values may also correspond to strong focal regions (e.g., cusped caustic geometries) where coherent effects at the receiver (which are currently omitted) tend to be constructive, decreasing the loss by as much as 3 dB.

This may account for the negative bias even for the 1000-ft source.

100-110 dB FOM Range (Figure 4-62)

In this case the only persistent, significant bias is at 300 ft where again extended surface-image interference is the likely source. The distributions tend to be somewhat tighter, especially at 1000 ft for the higher frequencies.

90-110 dB FOM Range (Figure 4-63)

A slight bias persists, however the differences between the two subintervals (90-100, 100-110) appear to be somewhat cancelling, leading to tighter summary distributions.

All FOM's (Figure 4-64)

The addition of the low and high FOM points (~12% of the total) has little impact on the previous distribution functions. The bias of these ensemble distributions is concentrated near 300 ft for all frequencies and deeper for 64 Hz.

Each FOM Range - All Sources and Frequencies (Figure 4-65)

The top four histograms in this figure correspond to the four FOM ranges indicated. Only the low- and high-FOM curves have not been shown in any of the previous figures. While the high FOM area is likely to lead to the largest errors, it corresponds to a small sample of points and contains no bottom-bounce paths (which, given the proper input reflectivity, should lead to smaller errors).

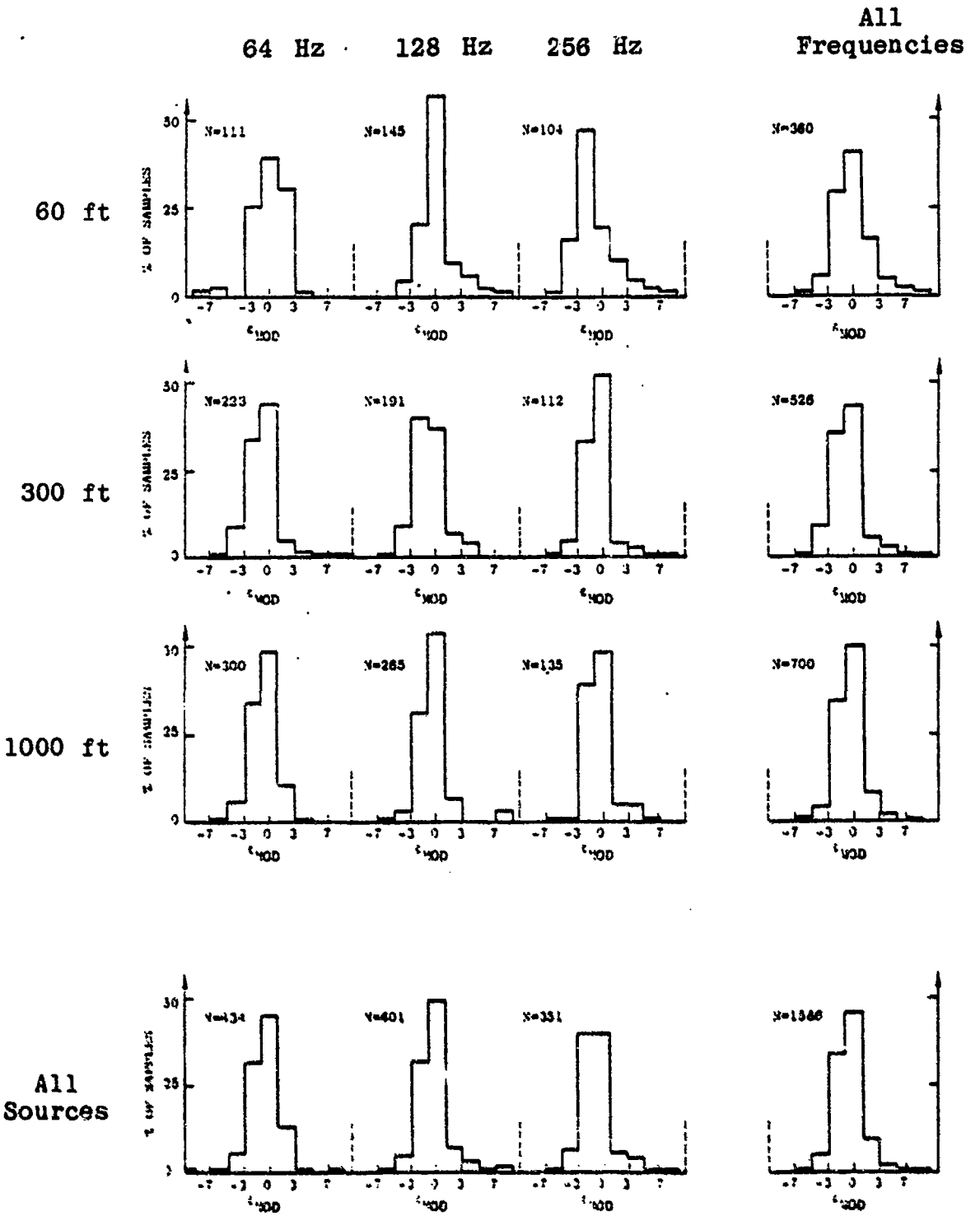

Figure 4-61. Sample Distribution Functions of Model Error, $\epsilon_{MOD} = TL_{PE} - TL_{MOD}$, for FOM Range 90 to 100 dB, 3 Source Depths × 3 Frequencies Plus Distributions across frequency and/or source depth. N = number of samples.

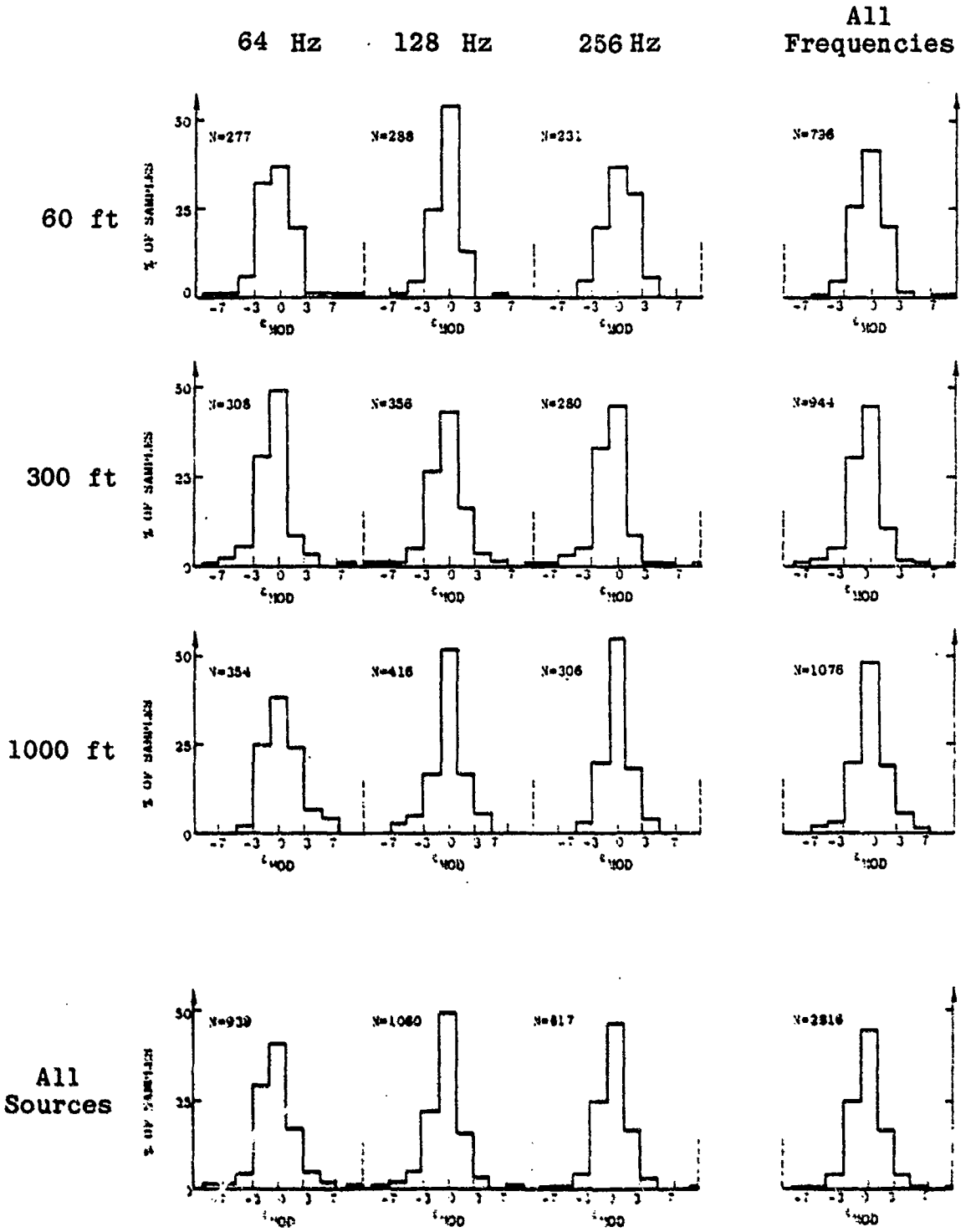

Figure 4-62. Sample Distribution Functions of Model Error, $\varepsilon_{MOD} = TL_{PE} - TL_{MOD}$, for FOM Range 100 to 110 dB, 3 Source Depths × 3 Frequencies Plus Distributions across frequency and/or source depth. N = number of samples.

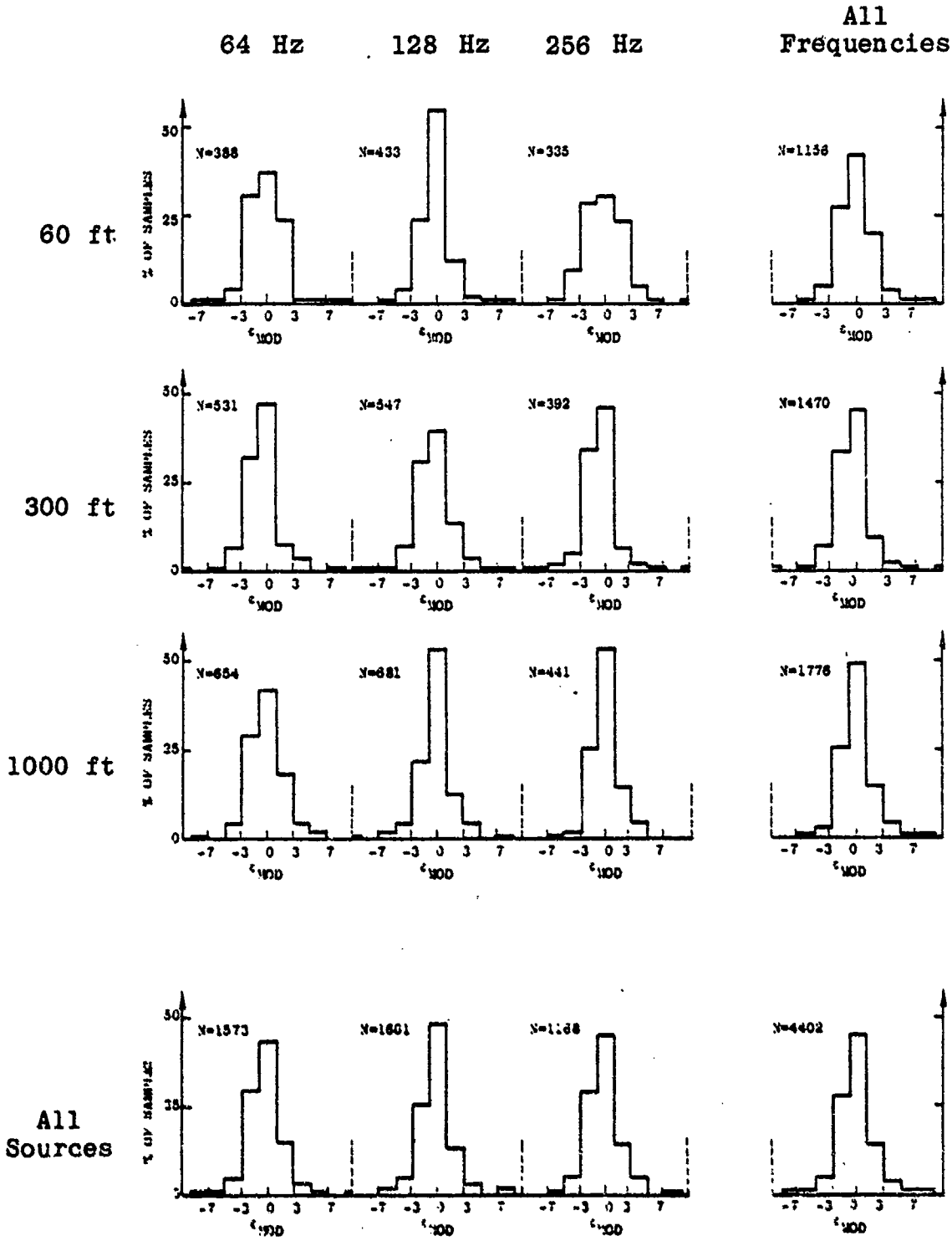

Figure 4-63. Sample Distribution Functions of Model Error, $\varepsilon_{MOD} = TL_{PE} - TL_{MOD}$, for FOM Range 90 to 110 dB, 3 Source Depths × 3 Frequencies Plus Distributions across frequency and/or source depth. N = number of samples.

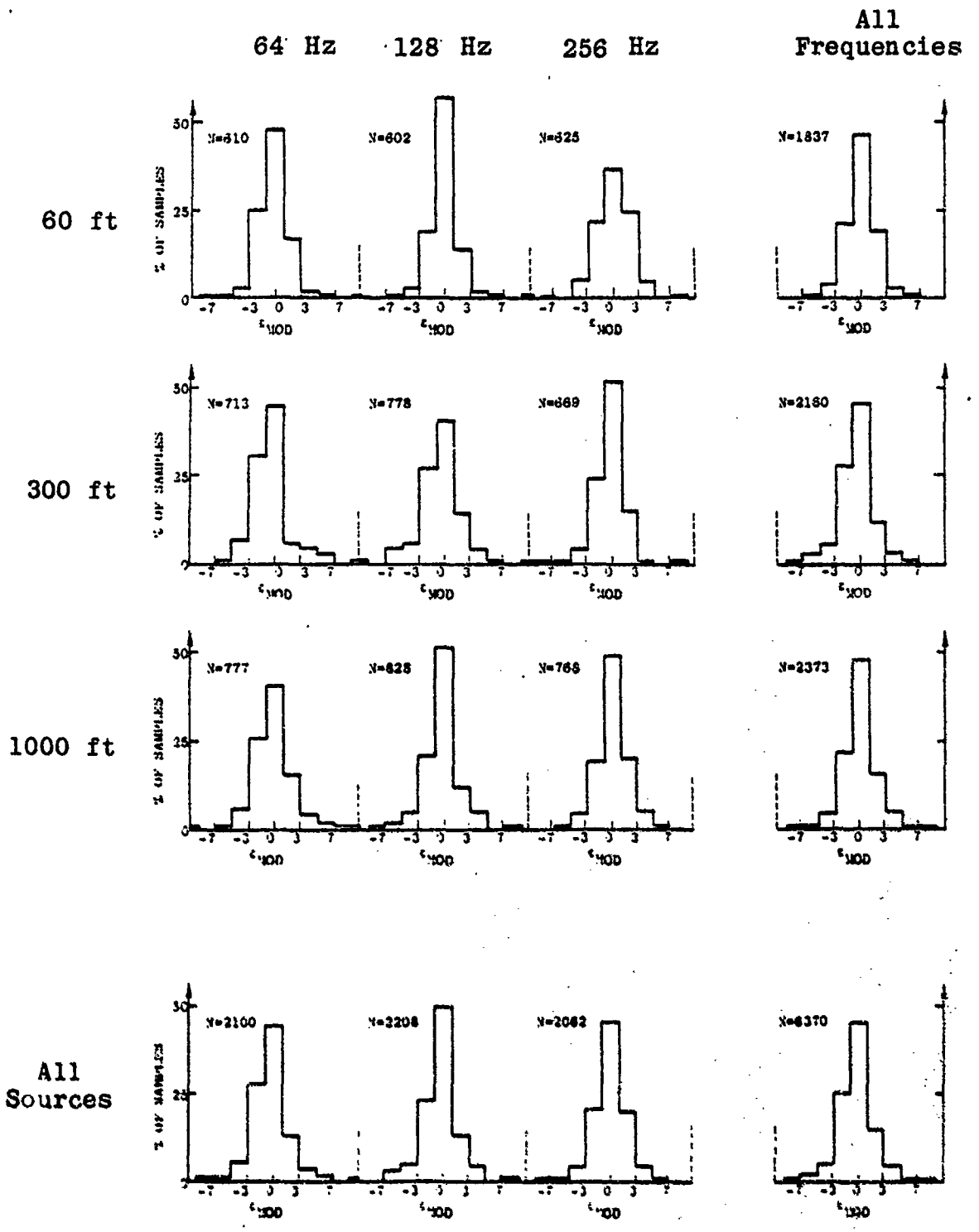

Figure 4-64. Sample Distribution Functions of Model Error, $\varepsilon_{MOD} = TL_{PE} - TL_{MOD}$, for FOM Range 80 to 120 dB, 3 Source Depths × 3 Frequencies Plus Distributions across frequency and/or source depth. N = number of samples.

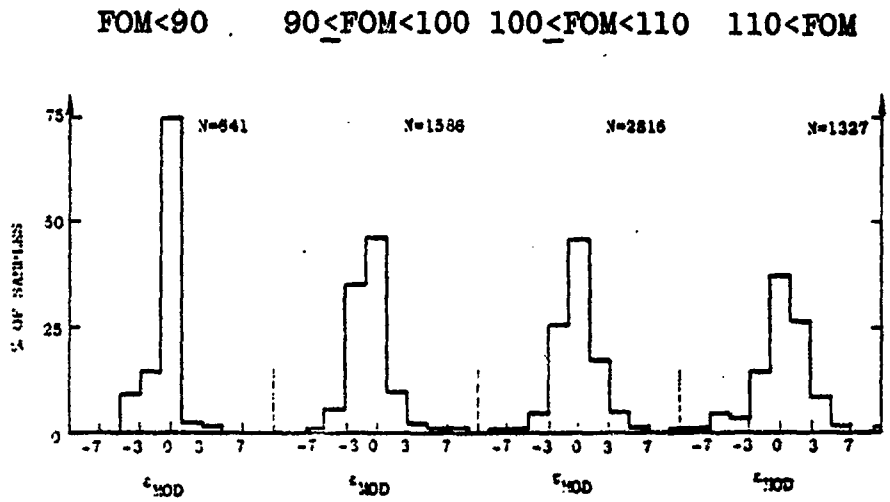

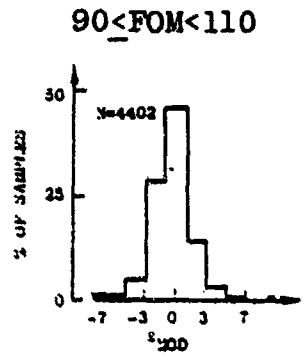

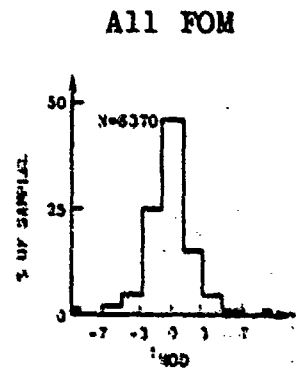

Figure 4-65. Sample Distribution Functions of Model Error, $\varepsilon_{MOD} = TL_{PE} - TL_{MOD}$, all source depths and frequencies, indicated FOM ranges. N = number of samples.

4.7.2 Statistics of Model Error

For each of the summary distributions across frequency, source depth, or both (i.e., for each marginal histogram in Figures 4-61 through 4-64 and for all histograms in Figure 4-65) the following statistics have been computed:

- μ - the estimated mean model error (= TL_{PE} - TL_{MOD})
- N - the number of samples for this case
- P_1 - the fraction of samples with absolute errors of less than 1 dB
- P_3 - the fraction of samples with absolute errors less than 3 dB
- σ_1 - the standard deviation of a normal distribution of zero mean containing the fraction P_1 in ±1 dB.
- σ_3 - the equivalent standard deviation corresponding to P_3 in ±3 dB.

Note that the σ's defined above are not true estimates of σ for the distribution unless the mean is zero (i.e., strictly, σ should correspond to the fraction in μ ±1 dB). Since all the mean errors are less than 1 dB this approximation is reasonable.

By introducing the two σ's a rough check on the normality of the distribution function may be made. If σ_1 and σ_3 are equal, the distribution function is approximately normal for errors between ±3 dB (with a corresponding likelihood, P_3, that the error is less than 3 dB). If (as is more typically the case in these data) $\sigma_3 > \sigma_1$, then the distribution function is tighter than a normal distribution. Alternatively, an estimated standard deviation

made on a pointwise basis using all points in ±3 dB (assuming $\mu = 0$) would be between σ_1 and σ_3, when $\sigma_1 < \sigma_3$.

Table 4-1 summarizes these statistics for the various FOM ranges, source depths, and frequencies, as indicated. In nearly all cases a slight (<1 dB) negative bias of the mean (model predicting too much loss) is found. It is largest for the low FOM's but tends to persist at 300 ft for all FOM's.

In all but the extreme low and high FOM cases a very consistent 40 to 50% of the points have errors of less than 1 dB and 85 to 92% have errors of less than 3 dB. In terms of comparable normal distributions, the central 50% of the points yield estimated standard deviations of 1.5 to 1.9 dB. The distributions are all slightly tighter than normal with standard deviations less than 2.1 dB over 90% of the points. Even for the extreme high FOM case the standard deviation is on the order of 2.5 dB.

Table 4-1

SUMMARY STATISTICS FOR COMPARISONS WITH PE
(See Text for Definition of Terms)

FOM Range	z_s or f	N	μ(dB)	Fractions P_1	Fractions P_3	Standard Deviations σ_1(dB)	Standard Deviations σ_3(dB)
<90 dB	All	641	-0.6	.74	.90	.9	1.8
90-100 dB	60 ft	360	-0.2	.41	.86	1.8	2.0
	300 ft	526	-0.8	.43	.85	1.7	2.1
	1000 ft	700	-0.6	.50	.92	1.5	1.7
	64 Hz	634	-0.7	.45	.90	1.7	1.8
	128 Hz	601	-0.4	.49	.88	1.5	1.9
	256 Hz	351	-0.7	.40	.86	1.9	2.0
	All	1586	-0.6	.46	.89	1.6	1.9
100-110 dB	60 ft	796	-0.3	.42	.88	1.8	1.9
	300 ft	944	-0.7	.45	.87	1.7	2.0
	1000 ft	1076	0.1	.48	.87	1.5	2.0
	64 Hz	939	-0.2	.41	.87	1.8	2.0
	128 Hz	1060	-0.4	.49	.87	1.5	2.0
	256 Hz	817	-0.3	.47	.89	1.6	1.9
	All	2816	-0.3	.45	.87	1.7	2.0
90-110 dB	60 ft	1156	-0.3	.42	.88	1.8	2.0
	300 ft	1470	-0.7	.45	.87	1.7	2.0
	1000 ft	1776	-0.1	.49	.90	1.5	1.8
	64 Hz	1573	-0.4	.43	.88	1.7	1.9
	128 Hz	1661	-0.4	.48	.87	1.5	2.0
	256 Hz	1168	-0.4	.45	.88	1.7	1.9
	All	4402	-0.5	.45	.87	1.7	2.0
>110 dB	All	1327	0.1	.37	.77	2.1	2.5
	60 ft	1837	0.0	.47	.88	1.6	1.9
All	300 ft	2160	-0.7	.46	.86	1.6	2.0
	1000 ft	2373	-0.1	.48	.86	1.5	2.0
	64 Hz	2100	-0.3	.44	.85	1.7	2.1
	128 Hz	2208	-0.4	.50	.86	1.5	2.0
	256 Hz	2062	-0.1	.46	.87	1.6	2.0
	All	6370	-0.4	.46	.86	1.6	2.0

4.8 SUMMARY OF MODEL EVALUATION

Extensive comparisons of model output with PE predictions for identical environments have been made. The model's ability to predict range-smoothed propagation loss for water-borne paths in a variety of environments has been the principal objective of these comparisons. Subsequent comparisons for bottom-interacting paths will be made. Such paths typically are less difficult to model since they rarely experience complex channeling and focusing effects, and model errors given the proper reflectivity are expected to be small. The principal difficulty for bottom-interacting paths will be the definition of appropriate reflection losses for the bottom.

The 180 separate comparisons with PE have been examined to identify likely sources of model error. At present all significant discrepancies appear to be traceable to recognized model limitations. Few of these limitations appear to be fundamental, however their remedy is not trivial. None of them is serious enough to warrant delaying release of the model.

Statistical comparisons have been made in an attempt to quantify the expected model accuracy. The model appears to have a slight bias (less than 1 dB) towards higher loss for reasons which have been identified. Model errors will be less than 1 dB 50% of the time and less than 3 dB 90% of the time. The error appears to have a distribution slightly more central than a normal distribution and its standard deviation is between 1.5 and 2.0 dB.

Because PE was used as the standard for comparison, "model error" here is with respect to PE. PE model errors with considerably less range-smoothing appear to have zero mean and a standard deviation of 1 dB (or less). Since the discrepencies have been traced to recognized model deficiencies, the above estimates are felt to represent actual errors and not be biased by PE errors.

4.8.1 Computer Running Times

In order for ASEPS to be a viable Fleet Support Product stringent requirements were placed on the running time of the propagation-loss model. The requirement was to be able to compute propagation loss from a receiver to three source depths at three frequencies to a range of 1000 nm in 1 CPU second on a CDC 6400. In the above test cases "speeds" were between 1000 and 2000 nm per CPU second with an average of 1500 nm per second.

Testing at FNWC has shown comparable speeds. A significant contributor to program speed has been the ability to use stored information from previously processed tracks. In comparison with the old FACT-extended version (FACT plus A+BLogR) the new model takes approximately twice the running time. This is a remarkable result considering the contrasting levels of sophistication in the two models. (The old FACT-extended model computed changes tc B strictly from depth-excess considerations.)

Considering the level of agreement obtained between ASTRAL and PE, comparisons of these running times are also interesting. The entire set of test cases required 20 seconds of CDC 6400 CPU time for ASTRAL and 14000 seconds

(4 hours) of TI-ASC CPU time for the PE runs. On a CDC 6400 the PE runs would have consumed more than 2 million CPU seconds (1 month). In terms of actual costs, the ASTRAL runs cost approximately $3.20, the PE (TI-ASC) runs cost approximately $3000, and the PE runs on the CDC 6400 would have cost approximately $300,000.

REFERENCES

1. C. L. Baker and C. W. Spofford, The FACT Model, Volume I, Maury Center Report 109, AESD, November 1974.

2. C. G. Bassett and P. M. Wolff, Fleet Numerical Weather Central Bottom Loss Values (U), FNWC, PRT #2, August 1970. (CONFIDENTIAL)

3. L. S. Blumen and C. W. Spofford, The ASTRAL Model, Volume II; Software Implementation, SAI Technical Report SAI-79-743-WA, January 1979.

4. D. F. Gordon, "Comparison of Low Frequency Acoustic Propagation in Deep Water With Normal-Mode Computations (U)," USN Journal of Underwater Acoustics 22, No. 4, pp. 325-346, October 1972. (CONFIDENTIAL)

5. D. M. Milder, J. Acoust. Soc. Am. 46, 1259-1263 (1969).

6. P. W. Smith, J. Acoust. Soc. Am. 55, 1197-1204 (1974).

7. C. W. Spofford, The FACT Model, Volume I, Maury Center Report 109, AESD, November 1974.

8. W. H. Thorp, J. Acoust. Soc. Am. 42, 270(L) (1967).

9. H. Uberall, R. D. Graves, A. Nagl., and G. L. Zarur, J. Acoust. Soc. Am. 58, 1171 (1975).

10. H. Weinberg and R. Burridge, J. Acoust. Soc. Am. 55, 63 (1974).

Assistant Secretary of the Navy
(Research, Eng. and Systems)
Department of the Navy
Washington, D. C. 20350
Attn: G. A. Cann 1

Chief of Naval Operations
Department of the Navy
Washington, D. C. 20350
Attn: OP-095 1
OP-095E 1
OP-096 1
OP-951 1
OP-952 1
OP-952D 1

Headquarters
Naval Material Command
Washington, D. C. 20360
Attn: Code Mat-08T245 2

Project Manager
Antisubmarine Warfare System Proj.
Department of the Navy
Washington, D. C. 20360
Attn: A. V. Bernard, PM-4 2

Office of Naval Research
800 North Quincy Street
Arlington, Virginia 22217
Attn: CODE 100 1
CODE 102B 1
CODE 220 1
CODE 230 1
CODE 460 1
CODE 480 1

Commander
Naval Electronic Systems Command
Naval Electronic Sys Command Hdqrs
Washington, D. C. 20360
Attn: PME-124 1
PME-124TA 1
PME-124/30 1
PME-124/40 1
PME-124/60 1
ELEX-320 2

Commander 1
Naval Sea Systems Command
Naval Sea Systems Command Hdqrs
Washington, D C. 20362
Attn: NSEA-06H1 1

Commander 1
Naval Air Systems Command
Naval Air Systems Command Hdqrs
Washington, D.C. 20361
Attn: NAIR-370 1

Deputy Under Sec. of Defense for
Research and Engineering
Department of Defense
Washington, D. C. 20301 1

Defense Adv. Research Proj Agency
1400 Wilson Boulevard
Arlington, Virginia 22209
Attn: Dr. T. Kooij 1

Commander in Chief, Pacific Fleet 1
P. O. Box 3
Pearl Harbor, Hawaii 96860
Attn: Code 3521 1

Commander in Chief 1
U. S. Atlantic Fleet
Norfolk, Virginia 23511
Attn: Code N353A 1

Commander 1
Third Fleet
Pearl Harbor, Hawaii 96860
Attn: Code N-7 1

Commander
Second Fleet
FPO New York 09501 1

Commander
Sixth Fleet
FPO New York 09501 1

Commander Fleet Air, Mediterranean
Commander, Antisubmarine War Force
U.S. Sixth Fleet
FPO New York 09521 1

Commander
Submarine Forces
U. S. Pacific Fleet
Pearl Harbor, Hawaii 96860
Attn: T. Curry 1

Commander
Submarine Development Group 12
Box 70 Nav. Sub. Base, N. London
Gronton, Connecticut 06340 1

Commander
Operational Test and Eval. Force
Naval Base
Norfolk, Virginia 23511 1

Commander Patrol Wings
U. S. Pacific Fleet
Naval Air Station
Moffett Field, California 94035 1

Commander
Oceanographic System, Atlantic
Box 100
Norfolk, Virginia 23511

Commander
Oceanographic System, Pacific
Box 1390
Pearl Harbor, Hawaii 96860

Commanding Officer
Fleet Numerical Weather Central
Monterey, California 93940

Commanding Officer
Fleet Weather Central
Box 113
Pearl Harbor, Hawaii 96860

Acoustic Research Center, DARPA
Naval Air Station
Moffett Field, California 94035
Attn: E. L. Smith

Commanding Officer
Naval Research Laboratory
Washington, D. C. 20375
Attn: CODE 8100
CODE 8160
CODE 2627

Commander
Naval Oceanographic Office
NSTL Station, Mississippi 39522
Attn: CODE 3000
CODE 3440
Library

Commanding Officer
Naval Ocean Research & Development
Activity
NSTL Station, Mississippi 39529
Attn: CODE 110
CODE 200
CODE 300
CODE 320
CODE 340
CODE 500
CODE 600

Naval Ocean Research & Devel. Act.
Liaison Office
800 North Quincy Street
Arlington, Virginia 22217
Attn: Code 130 1

Officer in Charge 1
New London Laboratory
Naval Underwater Systems Center
New London, Connecticut 06320
Attn: Code 31 1
Code 312 1
Code 542 1

Commander 1
Naval Ocean Systems Center
San Diego, California 92152
Attn: Code 5301 1
Code 714 1
Code 7143 1

Commander 1
Naval Air Development Center
Warminster, Pennsylvania 18974
Attn: E. Garabed 1
P. Van Schuyler 1

Commanding Officer
Naval Coastal Systems Laboratory
Panama City, Florida 32407 1

Officer in Charge
White Oak Laboratory
Naval Surface Weapons Center
Silver Spring, Maryland 20910 1

Officer in Charge Carderock Lab.
David W. Taylor Naval Ship Res &
Development Center
Bethesda, Maryland 20084 1

Director
Naval Ocean Surveillance Inf. Ct.
4301 Suitland Road
Washington, D. C. 20390 1

Commanding Officer
Naval Intelligence Support Ct.
4301 Suitland Road
Washington, D. C. 20390 1

Superintendent
Naval Postgraduate School
Monterey, California 93940
Attn: Library 1

Commanding Officer
Naval Environmental Prediction
Research Facility
Monterey, California 93940 1

Director of Naval Matters 1
Center of Naval Analysis
Arlington, Virginia 22209
Attn: C. E. Woods 1

Applied Physics Laboratory
University of Washington
1013 NE Fortieth Street
Seattle, Washington 98195 1

Applied Physics Laboratory 1
Johns Hopkins University
Johns Hopkins Road
Laurel, Maryland 20910
Attn: Dr. G. L. Smith 1
W. L May 1
A. Boyles 1

Applied Research Laboratory 1
Pennsylvania State University
P. O. Box 30
State College, Pennsylvania 16801
Attn: Dr. S. McDaniel 1

Applied Research Laboratories 1
University of Texas
P. O. Box 8029
Austin, Texas 78712
Attn: Dr. L. D. Hampton 1
G. E. Ellis 1

Marine Physical Laboratory
Scripps Inst. of Oceanography
San Diego, California 92152
Attn: Dr. V. C. Anderson 1
Dr. F. N. Spiess 1
Dr. F. H. Fisher 1

Palisades Geophysical Inst. Inc.
131 Erie Street
P. O. Box 396
Blauvelt, New York 10913 1

Rosenstiel School of Marine Sciences
University of Miami
4600 Rickenbacker Causeway
Miami, Florida 33156
Attn: Dr. H. DeFerrari 1

Woods Hole Oceanographic Inst.
Woods Hole, Massachusetts 02543
Attn: Dr. E. E. Hays 1

Analysis and Technology, Inc. 1
Route 2
North Stonington, Connecticut 06359
Attn: S. Elam 1

Arthur D. Little, Inc.
15 Acorn Park
Cambridge, Massachusetts 02140
Attn: W. G. Sykes 1
Dr. G. Raisbeck 1

B-K Dynamics, Inc.
15825 Shady Grove Road
Rockville, Maryland 20850
Attn: P. G. Bernard 1
L. T. Lynch 1

Bell Telephone Laboratories
1 Whippany Road
Whippany, New Jersey 07981
Attn: Dr. J. F. Gianola 1
Dr. J. H. Doles 1

Bolt, Beranek and Newman
1701 N. Fort Myer Drive
Suite 1001
Arlington, Virginia 22209 1

Bolt, Beranek and Newman
50 Moulton Street
Cambridge, Mass. 02138
Attn: Dr. P. W. Smith 1

Daniel H. Wagner Associates
Station Square One
Paoli, Pennsylvania 19301 1

Daubin Systems Corp.
104 Crandon Boulevard
Suite 315
Key Biscayne, Florida 33149
Attn: Dr. S. C. Daubin 1

Ocean Data Systems, Inc.
6000 Executive Boulevard
Rockville, Maryland 20852
Attn: Dr. E. Morenoff 1
E. Ver Hoef 1

Ocean Data Systems, Inc.
2400 Garden Road
Monterey, California 93940 1

Operations Research, Inc.
1400 Spring Street
Silver Spring, Maryland 20910
Attn: Dr. J. I. Bowen 1

Planning Systems Inc.
7900 Westpark Drive
Suite 600
McLean, Virginia
Attn: Dr. L. P. Solomon 1
R. Klinkner 1

Raytheon Company
Submarine Signal Division
P. O. Box 360
Portsmouth, Rhode Island 02871
Attn: Dr. B. A. Becken 1
Dr. H. Woodsum 1

Summit Research Corp.
1 West Deer Park Drive
Gaithersburg, Maryland 20760 1

SUTRON Corp.
1925 N. Lynn Street
Suite 700
Arlington, Virginia 22209
Attn: C. H. Dabney 1

TRACOR, Inc.
6500 Tracor Lane
Austin, Texas 78721
Attn: Dr. A. F. Wittenborn 1

TRACOR, Inc.
1601 Research Boulevard
Rockville, Maryland 20850
Attn: J. T. Gottwald 1

TRW Systems Group
7600 Colshire Drive
McLean, Virginia 22101
Attn: I. B. Gereben 1
R. T. Brown 1

Undersea Research Corp.
7777 Leesburg Pike
Suite 306
Falls Church, Virginia 22043
Attn: V. F. Anderson 1

Underwater Systems, Inc.
8121 Georgia Avenue
Silver Spring, Maryland 20910
Attn: Dr. M. S. Weinstein 1

XONICS, Inc.
6837 Hayvenhurst Avenue
Van Nuys, California 91406

DEPARTMENT OF THE NAVY
OFFICE OF NAVAL RESEARCH
875 NORTH RANDOLPH STREET
SUITE 1425
ARLINGTON VA 22203-1995

IN REPLY REFER TO:

5510/1
Ser 321OA/011/06
31 Jan 06

MEMORANDUM FOR DISTRIBUTION LIST

Subj: DECLASSIFICATION OF LONG RANGE ACOUSTIC PROPAGATION PROJECT (LRAPP) DOCUMENTS

Ref: (a) SECNAVINST 5510.36

Encl: (1) List of DECLASSIFIED LRAPP Documents

1. In accordance with reference (a), a declassification review has been conducted on a number of classified LRAPP documents.

2. The LRAPP documents listed in enclosure (1) have been downgraded to UNCLASSIFIED and have been approved for public release. These documents should be remarked as follows:

   Classification changed to UNCLASSIFIED by authority of the Chief of Naval Operations (N772) letter N772A/6U875630, 20 January 2006.

   DISTRIBUTION STATEMENT A: Approved for Public Release; Distribution is unlimited.

3. Questions may be directed to the undersigned on (703) 696-4619, DSN 426-4619.

BRIAN LINK
By direction

Subj: DECLASSIFICATION OF LONG RANGE ACOUSTIC PROPAGATION PROJECT (LRAPP) DOCUMENTS

DISTRIBUTION LIST:

NAVOCEANO (Code N121LC – Jaime Ratliff)
NRL Washington (Code 5596.3 – Mary Templeman)
PEO LMW Det San Diego (PMS 181)
DTIC-OCQ (Larry Downing)
ARL, U of Texas
Blue Sea Corporation (Dr.Roy Gaul)
ONR 32B (CAPT Paul Stewart)
ONR 321OA (Dr. Ellen Livingston)
APL, U of Washington
APL, Johns Hopkins University
ARL, Penn State University
MPL of Scripps Institution of Oceanography
WHOI
NAVSEA
NAVAIR
NUWC
SAIC

Declassified LRAPP Documents

Report Number	Personal Author	Title	Publication Source (Originator)	Pub. Date	Current Availability	Class.
Unavailable	Bossard, David C.	ACOUSTIC ANALYSIS/ASEPS	Wagner Associates	780726	ADA076268	U
NRLMR3832	Heitmeyer, R., et al.	PRELIMINARY RESULTS OF AN ANALYSIS OF BEAM NOISE IN THE MEDITERRANEAN (U)	Naval Research Laboratory	780901	ND ADC016220	U
Unavailable	Watrous, B. A.	PARKA 1 OCEANOGRAPHIC DATA COMPENDIUM	Naval Ocean R&D Activity	781101	ADB115967	U
Unavailable	Dunbar, B., et al.	LAMBDA PROCESSING LABORATORY AND ENGINEERING SUPPORT, FINAL REPORT 1 JANUARY 1977 - 31 OCTOBER 1978	Texas Instruments, Inc.	781129	ND	U
Unavailable	Blumen, L. S., et al.	ASTRAL MODEL. VOLUME 2: SOFTWARE IMPLEMENTATION	Science Applications, Inc.	790101	ADA956122	U
Unavailable	Spofford, C. W.	ASTRAL MODEL. VOLUME 1: TECHNICAL DESCRIPTION	Science Applications, Inc.	790101	ADA956124	U
Unavailable	Townsend, R., et al.	SELF-TENSIONING ACOUSTICAL HORIZONTAL LINE ARRAY (SPRAY) DATA ANALYSIS. FINAL REPORT OF BEARING STAKE TESTS JANUARY THRU MARCH 1977. VOLUME IA. OVERALL PROGRAM PERFORMANCE RESULTS WITH TEST RESULTS SUMMARY	Sanders Associates, Inc.	790101	ADC017573	U
Unavailable	Unavailable	SELF-TENSIONING ACOUSTICAL HORIZONTAL LINE ARRAY (SPRAY) DATA ANALYSIS. FINAL REPORT OF BEARING STAKE TESTS JANUARY THRU MARCH 1977. VOLUME IB. DETAILED DESCRIPTION, TEST RESULTS	Sanders Associates, Inc.	790101	ADC017574	U
Unavailable	Unavailable	SELF-TENSIONING ACOUSTICAL HORIZONTAL LINE ARRAY (SPRAY) DATA ANALYSIS. FINAL REPORT OF BEARING STAKE TESTS JANUARY THRU MARCH 1977. VOLUME II. DATA ANALYSIS FACILITY AND DATA REDUCTION METHODOLOGY	Sanders Associates, Inc.	790109	ADC017575	U
Unavailable	Unavailable	SELF-TENSIONING ACOUSTICAL HORIZONTAL LINE ARRAY (SPRAY) DATA ANALYSIS. FINAL REPORT OF BEARING STAKE TESTS JANUARY THRU MARCH 1977. VOLUME IIIA. DATA POINTS 1, 2 AND 3 RAW DATA	Sanders Associates, Inc.	790109	ADC017576	U
Unavailable	Unavailable	SELF-TENSIONING ACOUSTICAL HORIZONTAL LINE ARRAY (SPRAY) DATA ANALYSIS. FINAL REPORT OF BEARING STAKE TESTS JANUARY THRU MARCH 1977. VOLUME IIIB. DATA POINTS 4, 5 AND 6 RAW DATA	Sanders Associates, Inc.	790109	ADC017577	U
Unavailable	Unavailable	SELF-TENSIONING ACOUSTICAL HORIZONTAL LINE ARRAY (SPRAY) DATA ANALYSIS. FINAL REPORT OF BEARING STAKE TESTS JANUARY THRU MARCH 1977. VOLUME IVA. DATA POINTS 7, 8 AND 9 RAW DATA	Sanders Associates, Inc.	790109	ADC017578	U